

Quantitative analysis with electron energy-loss spectroscopic imaging and its application in pathology

(Kwantitatieve analyse met behulp van elektron energieverlies spectroscopische afbeeldingen en de toepassing hiervan in de pathologie)

Proefschrift

Ter verkrijging van de graad van doctor aan de
Erasmus Universiteit Rotterdam op gezag van de
rector magnificus
Prof. dr. P.W.C. Akkermans M.A.

en volgens besluit van het college voor promoties
de openbare verdediging zal plaatsvinden op
woensdag 6 september 1995 om 13.45 uur
door
Augustinus Laurens Dominicus Beckers
geboren te 's-Gravenhage

Promotiecommissie

Promotor: Prof. dr. E.S. Gelsema
Co-promotor: Dr. W.C. de Bruijn
Overige leden: Prof. dr. H.G. van Eijk
Prof. dr. ir. P. Kruit
Prof. dr. ir. A.W.M. Smeulders

Contents

1. General introduction	7
Part I: Electron spectroscopic image analysis	
2. Physics and instrumentation	13
2.1 The interaction of fast electrons with matter	13
2.1.1 Elastic scattering	13
2.1.2 Inelastic scattering	14
2.2 Electron energy-loss spectroscopy and electron spectroscopic imaging	16
2.2.1 Electron energy-loss spectroscopy (EELS)	16
2.2.2 Electron spectroscopic imaging (ESI)	17
2.3 Description of the laboratory for electron microscopic imaging and processing	19
2.4 The resolution of analog and digital EFTEM images	22
2.4.1 Resolution limitations in the electron microscope	23
2.4.2 Other resolution limiting effects	25
3. Principles of quantification	27
3.1 Quantification in electron spectroscopic images	27
3.2 The role of internal standards for quantification	28
3.3 Specimen thickness	29
4. Image restoration	31
4.1 Shading and gamma-correction	31
4.1.1 Shading	31
4.1.2 Camera non-linearity	31
4.1.3 Corrections	32
4.1.4 Experimental results of correction	34
4.2 Specimen drift correction	34
5. Image modelling	35
5.1 Spectral models and spectroscopic images	35
5.2 Characterization of image statistics	37
5.2.1 The combination of scintillator screen and TV-camera in the acquisition system	37
5.2.2 The relation between electron beam intensity and camera output	37
5.2.3 Image statistics	38
5.2.4 Experimental results	39

APPENDIX A5	40
A5.1 Derivation of the relationship between electron beam intensity and greyvalue	40
A5.2 Light-production weights for the combination of a first order scintillator screen and an integrating sensor	43
A5.3 The relationship between mean and variance of image greyvalues	44
6. Background correction	46
6.1 Curve fitting or parameter estimation	46
6.2 An efficient algorithm for background fitting	47
6.2.1 Theory	47
6.2.2 Implementation and results	49
APPENDIX A6	52
Listing of the spectrum fitting routine	
7. Measurement issues	54
7.1 The precision of concentration measurements	54
7.1.1 Theory	54
7.1.2 An experimental investigation of the approximation of $\sigma_{I_b}^2$ by V_{I_b}	56
7.2 Strategies for concentration analysis	57
7.2.1 The calculation of signal to noise ratio images and their use for thresholding	57
7.2.2 Additional and alternative strategies for analysis	58
7.3 Opportunities for the validation of the image data	59
7.4 Measurement linearity	61
7.4.1 The investigation of linearity with double sections of Fe-Chelex	62
7.4.2 The relation between R_{Fe} and $\ln(I_t/I_0)$ in sections with Fe-Chelex	64
7.4.3 The investigation of linearity with R_{Fe} - $\ln(I_t/I_0)$ plots from sections with Fe-Chelex	66
7.4.4 The consistency of $\ln(I_t/I_0)$ measurements	66
7.4.5 Variations in the loading of Fe-Chelex spheres	67
7.5 The reproducibility of measurements	69
8. Image acquisition and analysis of Fe in biological specimens	70
8.1 Design considerations of an image acquisition protocol	70
8.2 Description of the image acquisition protocol for Fe	76
8.3 The analysis procedure for Fe	78
9. Discussion part I	82

Part II: Application of ESI-analysis in Pathology

10. Electron spectroscopic image analysis of cellular iron in an overload situation	89
10.1 Iron overload in the liver	89
10.2 Materials and methods	93
10.3 Results	97
10.4 Discussion	99
11. Electron spectroscopic imaging as a tool for the analysis of structure and composition of isolated ferritin particles	108
11.1 Carbon specific imaging	108
11.2 Materials and Methods	109
11.3 Results	112
11.4 Discussion	114
12. General conclusions and summary	119
References	123
Publications	134
Algemene conclusies en samenvatting	138
Dankwoord	142
Curriculum Vitae	143

Chapter 1. General introduction

After the invention of the transmission electron microscope (TEM) in 1931 by Ruska and Knoll, it took about 20 years to develop the instrument into a tool for ultrastructural research. In material science this led to the ability to visualize and investigate atomic arrangements through the imaging of columns of atoms in a lattice or by electron diffraction. In biology the instrument enabled the visualization of cell structures at an unsurpassed level of detail. New cell structures, cells and organisms were depicted and more knowledge was gained about the complex ultrastructural morphology of the cell. Novel preparation procedures for fixation, cytochemical staining and labelling, embedding and the use of ultramicrotomy and cryo-techniques increased the investigative capabilities of the TEM in the direction of cell functioning. In physics, right from the beginning, it was recognized that the interaction of electrons irradiating a specimen can be used not only for visualization but also gives the opportunity to investigate the chemical nature of the irradiated matter. This opened the way to the analytical use of the TEM and many instruments were subsequently equipped with highly specialized detectors for each of the analytical possibilities. In this way true micro-analytical laboratories were created.

Two main types of TEMs have been developed: the scanning transmission electron microscope (STEM) and the conventional transmission electron microscope (CTEM). In the STEM, a small relocatable spot irradiates the specimen and scanning techniques are used to move the spot across the specimen to form an image. In the CTEM, the specimen is illuminated with a static beam as a whole and an image is formed in parallel. Both microscope types are still subject to a constant evolution. One important step of progress towards the analytical use of the TEM was the invention of the electrostatic energy analyzer by Möllenstedt in 1949. Since the electrons, which are transmitted through the specimen, at the expense of some energy-loss, contain information about that specimen, much effort was put in creating new energy-selecting devices. For use in combination with STEM instruments mainly, the sector magnet spectrometer was developed to create energy-loss spectra and also energy-filtered images (with additional lenses). For the CTEM, in 1962 Castaing and Henry were able to design an imaging spectrometer, later followed by the Ω -filter of Rose in 1978, both permitting energy-selected images and diffraction patterns to be obtained. In contrast to the sector magnet system, which is an extension of the microscope below the column, both latter types of spectrometer are integrated in the microscope column.

These laboratory developments were implemented by electron microscope manufacturers. This led to the recent commercial availability of energy-filtering transmission electron microscopes (EFTEM): the Zeiss EM902, equipped with the Henry-Castaing filter appeared in 1985 and the Zeiss EM912, containing the Ω -filter followed in 1992. These instruments have great potentials for application in biology. Energy-filtering results in a considerable improvement of the image quality through the exclusion of inelastically scattered

Chapter 1

electrons from image formation [Reimer91]. On the other hand, the inelastically scattered electrons contain a wealth of chemical information about the irradiated specimen. The EFTEM has the capability to also capture these electrons, thus opening the way to chemical micro-analysis through electron spectroscopic imaging (ESI) and analysis (Chapter 2). Although the instrumental capabilities of the EFTEM are well-developed [Reimer88], the full exploitation of these capabilities by analysis techniques is still immature. Particularly the computerized processing and analysis of spectroscopic images is currently a topic of many investigations. One of the major objectives of these investigations is the development of quantitative techniques. In our laboratory, preliminary investigations in this field were performed by De Bruijn and Sorber [Sorber93]. In this thesis (part I), the development of analytical techniques, particularly for the quantitative imaging of chemical element concentrations, are investigated further. A major motivation for this development was the need to measure element quantities in situ in tissues with pathological deviations. Analytical biochemistry generally employs techniques with a spatial resolution determined by the size of the analyzed tissue part. Cytochemistry enables to study morphology and function at the cellular level. ESI makes the step towards the ultrastructure. At this level, distributions of chemical elements can be measured. The limits of this technique are currently explored.

Several disorders are known to be accompanied by the presence of a more than functional and frequently toxic amount of certain metals in the human body [Alt90], such as iron in the case of hemochromatosis or copper in e.g. Wilson's disease. A common aspect of these disorders is the intracellular storage of surplus quantities of such elements. Transmission electron microscopy is already established as a valuable tool for studying ultrastructural changes of the metal overloaded cell. The combined ultrastructural and analytical potentials of the EFTEM could provide an enhanced way of investigating these overload conditions. If the quantitative capabilities of the instrument were improved, more knowledge could be obtained e.g. about the effects of treatment within the context of the cell.

Because iron is an element with various unknown aspects regarding storage in overload conditions and iron is known to survive the preparation steps for electron microscopy (fixation, embedding, wet-sectioning [Stearns94]), this element was selected as the central theme regarding quantification.

If the concentration of iron in storage patterns is to be sensibly investigated by ESI, this has some implications for the requirements imposed on the measurement procedures that are to be developed. On morphological grounds, major iron storage patterns are believed to consist of conglomerates of the macromolecule ferritin due to which concentrations below 1 iron atom/nm³ are to be expected. Thus, the lower limit of detection should be better than this. To study concentration variations in relation to the morphology of storage patterns, it is reasonable to expect that the spatial resolution of the measurements approximates the resolution of the TEM under normal observation conditions (~1 nm) and is not more than about one order of magnitude worse. This means that the resolution in the final iron

concentration distribution images should be better than 10 nm. Both requirements make a careful consideration of various quantification aspects necessary. Because of that, this thesis is composed of two parts. The first part mainly treats methodological issues and the development of quantification procedures. The second part considers the application of these procedures.

More specifically, problems addressed in Part I are the development of a suitable image acquisition protocol, the definition of corrective image processing steps where necessary and the development of the actual quantification procedures. In addition to obtaining a measurement value, this latter issue also comprises an indication of the precision of this value and its use for the objective detection of element quantities.

For the application in biology in Part II, the purpose was to investigate whether an element such as iron could be measured in cells with sufficient sensitivity and resolution in order to be of use to the researching biologist. For this question to be answered, liver biopsy material of a patient with an established excessive iron accumulation disorder (hemochromatosis) was available, before and after treatment by phlebotomy. Concentrating on the disease of hemochromatosis, the problem was considered whether the effect of phlebotomy treatment would be measurable in the iron accumulating organelles. Since from bio-chemistry it is known that the iron accumulation in liver cells occurs in various forms, it was further questioned whether, on the basis of element concentration measurements, it would be possible to characterize these forms. Related to the elemental imaging capabilities of ESI, it was explored whether this modality can be used as a tool for the investigation of isolated (macro molecular) structures by the natural presence of specific elements such as carbon.



Part I.

Electron spectroscopic image analysis

Chapter 2. Physics and instrumentation

2.1 The interaction of fast electrons with matter

When matter is irradiated by a beam of fast electrons, various interactions may take place. When the specimen is sufficiently thin, the beam passes through and from either the properties of the out-coming beam or from the interaction products, structural and chemical information can be obtained about the matter under investigation. The thinner the specimen, the more electrons pass without any interaction. Differentiation between types of interactions can be based on the amount of energy transferred during such events [Egerton86]. Those interactions that transfer only a very limited amount of energy to the irradiated atoms are called elastic scattering. In inelastic scattering, in contrast, energy is transferred to the atoms, usually modifying the atomic state. Using the term scattering does justice to the fact that interactions in most cases are accompanied by a change of the angular distribution of the incident electrons.

2.1.1 Elastic scattering

Elastic scattering of an electron beam is caused by interaction with the combined electrical fields of an atomic nucleus and its surrounding electron shells. In this field, dominated by the positively charged nucleus, incoming electrons are deviated possibly over large angles, see Fig. 2.1. A central concept in describing elastic scattering is the differential cross-section $d\sigma_e/d\Omega$, expressing the probability of having such a scatter event for one atom per unit solid angle. The probability distribution of scattering by one atom as a function of

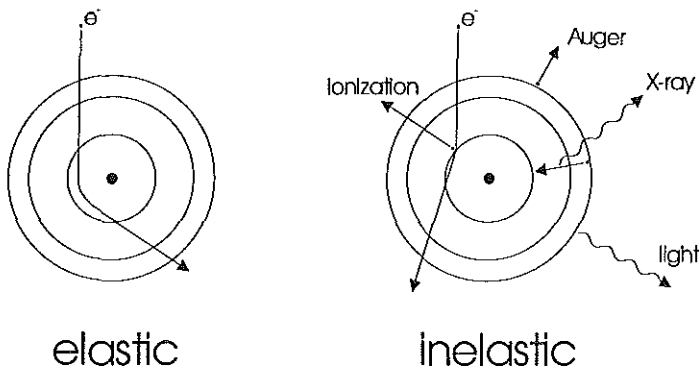


Figure 2.1 Two types of electron - matter interaction are generally discerned. With elastic interactions, virtually no energy is transferred to the atom. After inelastic interaction, the incident electron proceeds with a lower energy.

Chapter 2

the scattering angle is peaked around zero. This holds similarly for the scattering by a collection of atoms arranged in amorphous matter, but in crystals also other usually very pronounced angular preferences occur, depending on the Bragg conditions [Alonso80]. Observation of scattered electrons, as e.g. in the electron microscope, is usually restricted to a limited aperture angle β . Consequently, the differential cross-section is integrated up to β and yields the cross-section $\sigma_{el}(\beta)$. For a given primary beam energy (e.g. 80 keV) the elastic cross-section roughly depends on the atomic number $\sigma_{el} \sim Z^{4/3}$. Therefore, in the transmission electron microscope elastic scattering contributes to the formation of image contrast if there are regions in a specimen consisting of different elements. In biological material, contrast is enhanced by staining or post-fixation with heavy elements [Reimer84]. A related quantity, reciprocal to the cross-section, is the mean free path $\lambda_{el} = [n_v \sigma_{el}(\beta)]^{-1}$, in which n_v is the total number of atoms per unit volume. The mean free path may be interpreted as the average distance between subsequent elastic scatterings.

Elastic scattering is also important when considering inelastic events, in the sense that the angular distribution of those events is modified by elastic interactions in the same specimen transition.

When the energy of the incoming electron beam is sufficiently high, head-on elastic collisions are able to disposition the atoms from their inter-atomic arrangement and are a source of damage to the specimen.

2.1.2 Inelastic scattering

Incident primary electrons in a beam lose energy when they interact with atomic shell electrons. The binding energy of the shell electrons is changed by this excitation or even made zero in the case of ionization. The excitation energies (for ionization and inter-band excitations) are specific for different atomic elements. In the case of ionization, in addition to the ionization energy, an amount of kinetic energy may be transferred to the excited electrons. Inner-shell or core electrons are relatively more strongly bound than the outer-shell electrons and, consequently, more energy is needed for their excitation. When an atom returns to a less excited state, energy is released in the form of X-rays, Auger electrons or light, see Fig. 2.1. Together with the modified energy content of the primary beam, these products contain specific information about the nature of the elemental structure of the irradiated matter. Detection and analysis techniques have been developed to investigate these sources: electron energy-loss spectroscopy (EELS), X-ray emission spectroscopy (XES), Auger-electron spectroscopy (AES) and cathodoluminescence (CL).

For inelastic scattering, the concept of the inelastic differential cross-section $d\sigma_{in}/d\Omega$ describes the scattering-angle dependent probability distribution, similar to elastic scattering. Inelastic scattering is even more forward-directed than elastic scattering. Thus the objective lens aperture β in the transmission electron microscope can be used to control the relative contributions of elastic and inelastic electrons to image formation. Scattering outside this aperture excludes electrons from the image. Comparing the total cross-sections for both types

of scattering (irrespective of the direction), the following simple dependency has been derived [Reimer91]: $\sigma_{in}/\sigma_{el} \approx 20/Z$. This relation, together with the different angular characteristics forms the basis of Z-contrast imaging. The relatively large inelastic cross-section for light elements, in addition to its more forward-peaked distribution are favourable conditions for the analysis of energy-loss of the inelastically scattered electrons by EELS. Especially in biology, the majority of the (interesting) elements have a low Z-number.

Another way to characterize inelastic interactions, which is relevant for EELS, is to consider the energy E that is lost by an electron in the primary beam. The single differential cross-section, however, does not explicitly express the dependency on the energy-loss. Therefore, the probability of interaction with an atomic shell electron, dependent on the energy-loss and in relation to the solid angle Ω can be described more adequately by the double differential cross-section $d^2\sigma_{in}/d\Omega dE$. In the transmission electron microscope, the observation of the (forward) scattering processes is normally confined to the limited objective lens aperture β , which excludes scatterings over larger angles. For inelastic scattering, this limitation can be expressed as the apparent interaction probability:

$$\frac{d\sigma_{in}(\beta)}{dE} = \int_0^\beta \frac{d^2\sigma_{in}}{dEd\Omega} d\beta \quad (2.1)$$

This equation, which is an expression for the energy-differential cross-section, holds for one atom of a particular element and for one shell-type of interaction with this atom. For inner-shell interactions with element x, the atomic shell is explicitly referred to (k=K,L,M..). Under specimen conditions with n_x atoms per unit area, the actual probability is proportional to $n_x d\sigma_k(\beta)/dE$, because the inner shell scattering by different atoms are independent events. If an area of the specimen is irradiated by a beam of total intensity I_T , due to elastic scattering only an amount $I_T(\beta)$ is available for inelastic scattering. The contribution of one type of inelastic interaction with a certain element to the observed energy dependent transmitted electron beam can now be expressed as:

$$J_x(E, \beta) = I_T(\beta) \cdot n_x \cdot \frac{d\sigma_k(\beta)}{dE} \quad (2.2)$$

under the condition that the thickness of the specimen allows only one single event of such an interaction per transmitted electron. For this to hold, the section thickness should not exceed the average distance between two consecutive inelastic scatterings as expressed by the inelastic mean free path λ_{in} . Outershell excitations, which occur more or less collectively over several atoms (plasmons) are by far the most probable inelastic events to occur [Egerton86]. Therefore, it suffices to regard the plasmon mean free path: $\lambda_p = [n_v \cdot \sigma_p(\beta)]^{-1}$, in which n_v is the total number of atoms per unit volume and $\sigma_p(\beta)$ the plasmon cross-section.

True biological specimens consist of a mixture of different elements in various quantities. Because the interactions with the inner-shell electrons of these atoms are

Chapter 2

independent events, the total energy-differential cross-section is the weighted sum of the energy-differential cross-sections: $\sum_{x,k} n_x \cdot d\sigma_k(\beta)/dE$. This quantity reflects the energy-dependent joint probability distribution of inner shell scatterings.

Since inelastic scattering may be accompanied by ionization and the generation of Auger electrons, chemical bonds may be broken and the dissipation of heat affects the vibrational states of the molecules in an organic specimen. These changes form another source of specimen damage. The ionized state makes an atom also more susceptible for displacement by head-on elastic collisions. It has been reported that, e.g., in the case of oxygen, only strong cyclic bounds are preserved under the heavy electron bombardment of an electron beam [Leapman88], resulting in a major loss of this element.

2.2 Electron energy-loss spectroscopy and electron spectroscopic imaging

2.2.1 Electron energy-loss spectroscopy (EELS)

If a specimen is irradiated by a mono-energetic electron beam and the intensity of the transmitted scattered electrons is measured as a function of their energy-loss, an electron energy-loss spectrum may be composed. Fig. 2.2 shows an example of such a spectrum. From left to right several peaks may be observed. In principle, at zero energy-loss the unscattered electrons are collected. In practice, the incident electron beam is not entirely monochromatic but has a certain energy-width and the elastic scattering of electrons by small angles costs only a very limited amount of energy. Therefore, the elastic and unscattered contributions are difficult to differentiate and both are combined in what is observed as a zero-loss peak. Next to the zero-loss peak is the plasmon peak, originating from (collective) excitations of outer-shell electrons. Still further to the right is the core-loss region in which so called core edges

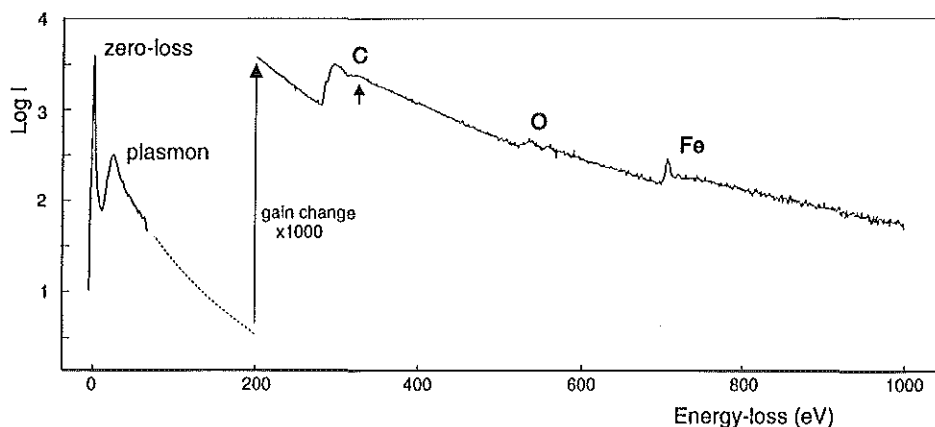


Figure 2.2 Example of an electron energy-loss spectrum of a biological specimen. The arrow behind the C-edge indicates dual scattering.

are visible. These edges originate from interactions with inner-shell electrons and in particular from their ionization. The ionization energies are specific for the various chemical elements and thus the edges occur at specific locations in the spectrum. This forms the basis for the analytical use of spectra. The very precise location and shape of the leading part of an edge, also referred to as near edge fine structure, contains information about small differences in the electronic binding state and thus about the chemical bonds. The edges are further characterized by long tails. This phenomenon is explained as coming from kinetic energy that has been transferred to the shell electron in addition to the ionization energy. From the considerations in section 2.1 it can be understood that the core-loss region in the spectrum reflects the joint probability distribution of inelastic events. Each of the interactions additively contributes to the spectrum, depending on the number of atoms present and the energy differential cross-section as described by eq. (2.2). As such, this relation forms the basis for quantitative energy-loss spectroscopy, which will be elaborated upon further in section 3.1.

When the thickness of the specimen is increased, multiple inelastic scatterings may occur in the transition of a primary electron. Plural scattering most frequently involves outer-shell excitations, because these interactions correspond to the largest cross-sections. In the low-loss region, multiple scattering is seen as a repetition of the plasmon-peak towards higher energy-losses. In the core-loss region, mixed type of plural scatterings are visible as plasmon peaks after each edge. Mathematically, the n^{th} order plurally scattered spectrum can be described as a convolution of the $(n-1)^{\text{th}}$ with a spectrum having only single inelastic scattering. For both qualitative and quantitative EELS, plural scattering must be avoided, since the relation between a spectral event and its originating process is lost. Therefore, the thickness of a specimen is usually kept as small as possible. As a rule of thumb, the section thickness should be less than the mean free path for plasmon interactions. If dual scattering occurs, spectrum de-convolution is an option for the reconstruction of the single scatter spectrum [Egerton89].

2.2.2 Electron spectroscopic imaging (ESI)

While in electron energy-loss spectroscopy the transmitted integral intensity through the specimen is expanded with respect to the energy-loss, in electron spectroscopic imaging this expansion takes place for a true two-dimensional area (two dimensions higher). Thus, for each specific location (x,y) within this area, the energy-loss dependence of the scattering is in principle known. This results in a three-dimensional description of the inelastic scattering within the specimen with two coordinates for the location and one for the energy-loss (E) . A discrete representation of a part of this three-dimensional space is shown in Fig. 2.3 and may be viewed as either a two-dimensional set of spectra or as a set of images with varying energy-losses [Jeanguillaume91]. Actually, both views are closely related to the two manners to acquire such an energy-loss expansion of a two-dimensional raster in the electron microscope. The first possibility is using a scanning transmission electron microscope (STEM) with a spectrometer. With such an instrument a two-dimensional part of the specimen is

Chapter 2

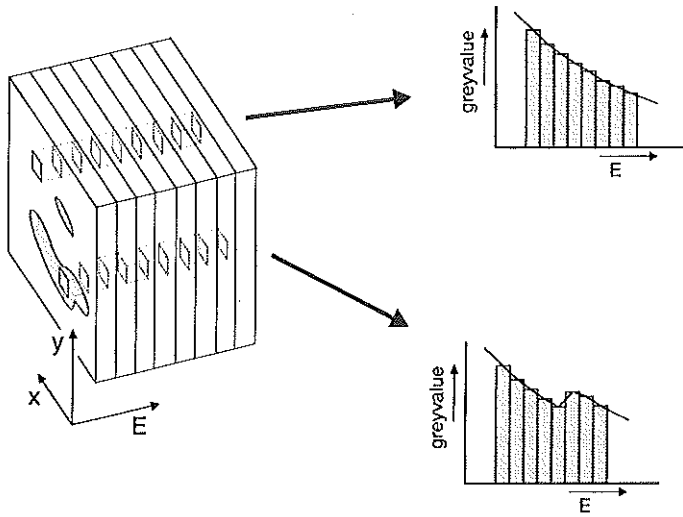


Figure 2.3 A discrete representation of a part of (x,y,E) -space. From such a representation, spectra as well as energy-filtered images may be reconstructed.

scanned with the electron beam, while the spectrometer records the spectrum [Hunt91, Leapman94, Botton94]. The second way uses an energy-filtering transmission electron microscope (EFTEM), in which images are formed from only those electrons that suffered a similar amount of energy-loss, specified as an energy-loss band [Castaing62, Ottensmeyer84]. This band can be tuned to different energy-losses and by scanning the energy-loss scale, a spectral representation is formed from the two-dimensional region. Both methods of acquisition result in a comparable representation of (x,y,E) -space. Since the results of both methods of acquiring the (x,y,E) -space are similar, spectral image sequences can be reconstructed from the STEM recording and spectra may be retrieved from the EFTEM images. It should be realized, however, that both types of instruments still have their own characteristics and specialities. High resolution spectra of small spots are more conveniently obtained with parallel detectors in the STEM [Shuman85, Krivanek91a, Tang94], while the energy-filtered images with a high resolution are far more easily acquired by two-dimensional image sensors in an EFTEM [Henkelman74]. The time to acquire (x,y,E) -space is generally shorter for the EFTEM, because the sensor is two-dimensional, while the STEM uses a one-dimensional sensor and has to use a scanning technique to build up a two dimensional raster. True three-dimensional sampling of (x,y,E) -space with high resolution would be ideal in terms of efficiency and convenience, because from this representation any reconstruction could be made. This is currently not yet possible, however. Some recent technical developments in energy-filtered imaging are the addition of new energy-filtering capabilities: below-column

in (S)TEM-instruments [Krivanek91a], and in-column with the Ω -filter [Lanio86, Mayer93], and the use of slow-scan CCD cameras as image sensors [Krivanek93].

Spectroscopic imaging of core-loss spectral regions is of special interest for qualitative and quantitative purposes. The presence of chemical elements can be localized and represented in relation to their quantity by concentration distribution images. In bio-medical sciences, where specimens with small structures of strongly varying composition are frequently encountered in practice, analysis of two-dimensional elemental distributions is more appropriate than point analysis by EELS. ESI potentially gives elemental distributions in clear reference to the surrounding biological structure. In this thesis, particular attention is given to a proper treatment of spectroscopic image sequences with the purpose to transform these sequences into quantitative element distribution images, thus relating the elemental quantities to their biological surroundings.

For the imaging of the morphology of biological structures, two spectral regions are of particular interest: the zero-loss region and the pre-carbon edge region. The energy-filtered image corresponding to the zero-loss peak can be seen as a normal transmission image from which the inelastically scattered electrons are excluded. In this way, the image degradation by such electrons is suppressed and as a consequence the image quality is improved [Reimer91]. Carbon is a major constituent of structures in biological specimens. Excluding electrons inelastically scattered by carbon, with energy-losses larger than 284 eV, enhances contributions to image contrast of other elements. This is done by so-called $E=250$ eV energy-filtered imaging. Unstained specimens are reported to show greatly improved contrast [Reimer91], allowing section-staining procedures to be circumvented [Stearns94]. Both $E=0$ eV and $E=250$ eV energy-filtered imaging modes are used for structural reference of the element distribution images.

2.3 Description of the laboratory for electron microscopic imaging and processing

Figure 2.4 shows an overview of the facilities available at the Erasmus University for analytical electron microscopy, electron spectroscopy and image processing. These facilities are distributed over the Department of Pathology and the Department of Medical Informatics. In the Pathology Department, a Zeiss EM 902 electron microscope and a Kontron IBAS 2000 image processing system are available, while the Department of Medical Informatics contributes to this equipment with a network of Hewlett-Packard Unix workstations, among which an HP 9000/735 and an HP 9000/725 workstation dedicated to image processing and pattern recognition research.

The Zeiss EM 902 is an energy-filtering electron microscope equipped with an in-column prism-mirror-prism energy-loss filter according to the Castaing-Henry principle [Castaing62]. The central part of this microscope is depicted in Fig 2.5. A virtually mono-energetic 80 keV electron beam irradiates the specimen. The scattered electrons are restricted in angular sense by the (selectable) objective-lens aperture, also functioning as the spectrometer entrance aperture [Bihr88]. The electrons passing this diaphragm, have different

Chapter 2

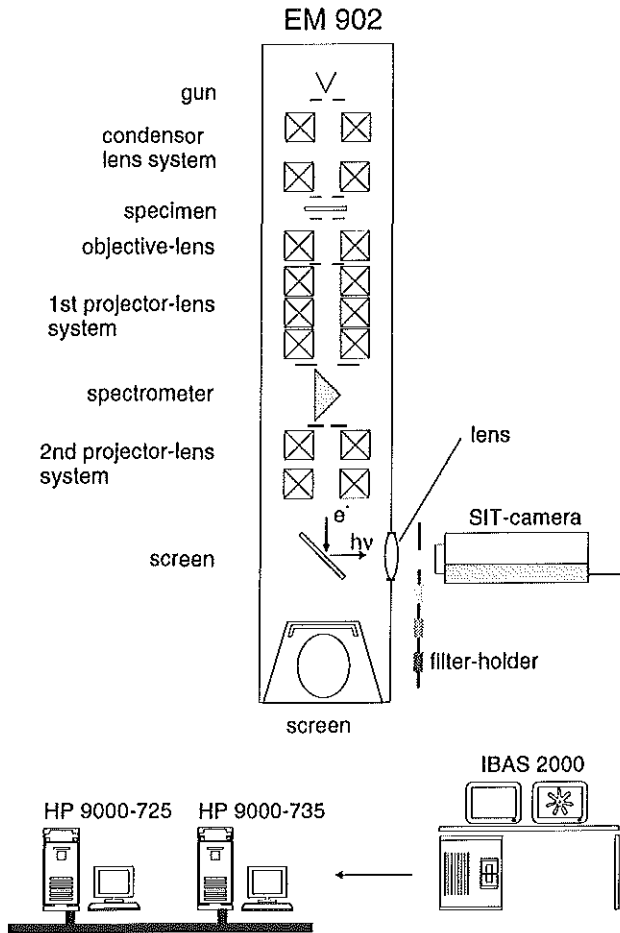


Figure 2.4 An overview of the laboratory equipment used for electron microscopic imaging and analysis.

energies, as a result of the inelastic scatterings within the specimen. The spectrometer modifies the angular characteristics of the electrons dependent on their energy. The result of this modification is two-fold, dependent on the plane that is considered. In the energy-dispersive plane below the spectrometer a spectrum is formed, while in the achromatic image plane an (achromatic) image of the specimen is present. The second projector lens below the filter has two focus conditions to magnify and project either of the two planes onto a fluorescent screen. By inserting a slit aperture in the energy-dispersive plane, electrons within

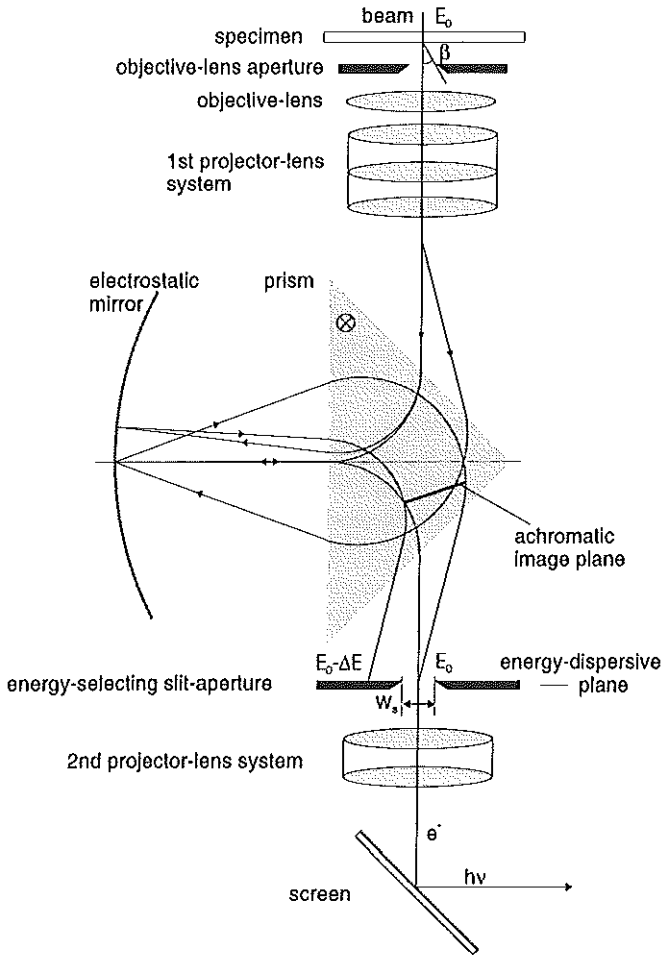


Figure 2.5 The spectrometer consists of two integrated sector magnets and an electrostatic mirror designed for the axial transfer of E_0 keV electrons. Tuning of energy-loss is done by adjusting the high voltage.

only a limited energy-band are allowed to pass. The width of the slit w_s (expressed in eV) is tunable and controls the energy-range that is selected. When projecting the achromatic image plane, the result is an energy-filtered image, in which only electrons from the selected energy-band contribute to the formation of the image. The pass-band is positioned along the energy-loss scale as follows. The electrostatic mirror is charged to 80 kV and the spectrometer is

Chapter 2

tuned to project 80 keV electrons in the energy-dispersive plane on the optical axis (zero-loss imaging). Electrons that have lost energy (ΔE) in the specimen are deviated (to the left in Fig. 2.5) and blocked by the slit aperture. Increasing the high voltage to augment the energy of the primary beam, e.g. with ΔE , the spectrometer still passes 80 keV electrons on-axis. These electrons, however, have lost an amount of energy equal to the energy increase ΔE of the primary beam above 80 keV. In this way the energy-loss scale can be scanned from 0-2000 eV.

The energy-filtered images or spectra are either projected onto a photographic plate, or a scintillator screen for visual observation, or onto a diagonally placed screen depicted in Figs. 2.4 and 2.5. The diagonal screen allows an image or a spectrum to be projected by an optical lens onto a camera attached to the C-mount outside the microscope column. This mount has been modified through the addition of an optical filter holder, by which the amount of light reaching the camera can be attenuated, independent of the illumination system of the microscope. The filter holder has four slots, three of which provide room for Kodak No. 96 gelatin neutral density filters. The fourth position in the holder is left open for direct viewing. The holder position is under manual control. A newer version of the filter holder foresees in computer control and has more filter slots. In the current set-up a silicon intensified target (SIT) TV-camera is attached to the C-mount. Two camera types were used: the Bosch TYC9A SIT-camera and the SIT-66 from Dage-MTI Inc. Both cameras are equipped with an RCA 4804 tube as the sensor. The camera output is fed into the IBAS frame-grabber, in which the images are digitized to 8 bits. The standard image size is 512x512 pixels, digitizing the image from a square part of the sensor. The IBAS has options for real-time integration and averaging of images for noise reduction. Images may be either locally stored or transferred to the HP 9000/735 system for further processing and analysis. The software used for image analysis is written in the C-programming language [Kernigan78]. For general purpose image processing tasks, the Scilimage package [Kate90a] is used.

2.4 The resolution of analog and digital EFTEM images

Under ideal conditions, an imaging system would be able to resolve details in the order of the wavelength λ . The De Broglie wavelength of 80 keV electrons is $\lambda=4.174$ pm [Reimer84]. This suggests the possibility that in a normal electron microscope, details on an atomic scale could be visualized. In practice this is not the case. Resolution limits, reached with instruments operated even at higher voltages, are currently around 0.1 nm, which enables the imaging of atom columns within crystal lattices [Phillipp94]. Several phenomena are responsible for this reduction in spatial resolution [Reimer84]. These will not be discussed here in full length. Only the most important ones and those of relevance to energy-filtered imaging and elemental imaging will be shortly addressed, split-up into effects fundamental to electron microscopy and other effects. The EM 902 is specified to reach a maximal point resolution of 0.5 nm [Zeiss].

2.4.1 Resolution limitations in the electron microscope

In energy-filtered transmission electron microscopy, several phenomena influence the resolution of the images. Some of the effects can be controlled by the user of the microscope by the selection of aperture dimensions. For the description of the resolution limitations, two operational conditions are discerned; one is the (more conventional) energy-filtered zero-loss imaging mode, the other is the situation in which elemental distributions are produced. For the first mode, diffraction, spherical aberration and chromatic aberration are the main effects to be considered. These are described in e.g. [Agar74, Reimer84]. For the creation of element distribution images, which case is considered in this thesis, in addition to the mentioned effects, the delocalization of inelastic scattering may be important. The effect of each resolution limiting contribution is generally expressed by the diameter of the associated disc of confusion.

The first process considered is diffraction. The electron wave below the specimen diffracts on the boundaries of the objective lens diaphragm and thereby limits the resolution. The effect depends on the semi-angle of this aperture [Agar74]. The diameter of the diffraction limiting disc is:

$$\delta_d = \frac{0.61\lambda}{\beta} \quad (2.3)$$

where λ is the wavelength of the primary electrons and β is the semi-angle in mrad. For some standard apertures in the EM 902, operated at 80 kV ($\lambda=4.2$ pm), numerical values for the diameter of the disc in eq. (2.3) are given in Table 2.1. It has been noted that under elemental imaging conditions, the effect of diffraction is relatively small.

Electrons that are scattered by the specimen follow helical trajectories in the magnetic lenses [Reimer84]. The strength of this effect depends on the scattering angle. As a consequence, the focus is not the same for all electrons. By selection of the plane of least confusion as the focus plane, some contributions to the image will be unsharp. This effect is called spherical aberration and the limitation of resolution is expressed by the size of the aberration disc [Shuman86]:

$$\delta_s = C_s \alpha^3 \quad (2.4)$$

in which C_s is the spherical aberration coefficient of the objective lens. In the EM 902, $C_s=2.2$ mm [Zeiss]. The angle α represents the effective value of the aperture. This angle is generally smaller than β and has to be properly chosen to take into account the anisotropy of inelastic scattering. For a sufficiently large value of β , $\alpha=[\theta_E\beta]^{1/2}$, with $\theta_E \approx E/2E_0$ and E_0 is the energy of the illuminating beam (80 keV in the EM 902). Table 2.1 contains numerical values for the diameter of the spherical aberration disc in the case of the imaging of iron ($E=708$ eV) and carbon ($E=284$ eV).

Chapter 2

Table 2.1 The limitation of resolution by diffraction, spherical aberration, chromatic aberration and delocalization of scattering is given for various standard objective apertures. The size of the chromatic aberration disc is expressed per eV and for a slit of 20 eV width. In the last column, the total aberration is calculated for $w_s=20$ eV.

E (eV)	β (mrad)	θ_E (mrad)	α (mrad)	δ_c (nm/eV)	$\delta_{c,20}$ (nm)	δ_s (nm)	δ_d (nm)	δ_R (nm)	δ (nm)
708	17	4.43	8.67	0.184	3.686	1.435	0.151	0.076	3.959
708	12	4.43	7.29	0.155	3.097	0.851	0.214	0.076	3.220
708	6	4.43	5.15	0.109	2.190	0.301	0.427	0.076	2.253
284	17	1.78	5.49	0.117	2.335	0.365	0.151	0.188	2.375
284	12	1.78	4.62	0.098	1.961	0.216	0.214	0.188	1.994
284	6	1.78	3.26	0.069	1.387	0.076	0.427	0.188	1.465

The thermal tungsten electron source of the EM 902 produces an energy distribution with a width of approximately 1.5 eV [Bih88]. Inelastic scattering in the specimen broadens this distribution considerably as is observed in the energy-loss spectrum. Chromatic aberrations resulting from this broadening may be restricted by energy-filtering, using a limited slit-width w_s (in eV) (Fig. 2.5). The remaining aberration is quantified by the size of the associated aberration disc [Shuman86]:

$$\delta_c = C_c \left(\frac{w_s}{E_0} \right) \alpha \quad (2.5)$$

where C_c is the chromatic aberration coefficient and E_0 is the primary beam energy (in the EM 902, $C_c=1.7$ mm and $E_0=80$ keV). The angle α is again the effective aperture angle as defined above. Table 2.1 also contains some values for δ_c expressed per eV because the slit-width is variable in size. When energy-filtered images are to be acquired, frequently used values for w_s vary from 5-25 eV, depending on the application.

The fourth resolution limiting influence is the delocalization of the scattering process. A rough estimate for the magnitude of this effect may be given by [Egerton86, Lavergne94]:

$$\delta_R = \frac{\lambda}{4\pi\theta_E} \quad (2.6)$$

in which, again, λ is the wavelength of the electron beam and $\theta_E \approx E/2E_0$. Table 2.1 contains

some values for δ_R , from which it can be concluded that this effect is negligible for the computed cases.

The individual contributions to the limitation of the resolution are combined by:

$$\delta = \sqrt{\delta_c^2 + \delta_s^2 + \delta_d^2 + \delta_R^2} \quad (2.7)$$

Values for the total aberration are given in Table 2.1 for $w_s=20$ eV. It will be clear from this section that the instrumental parameters, slit-width and objective-lens aperture, have a decisive influence on the spatial resolution of the final element distribution image.

2.4.2 Other resolution limiting effects

Other effects further affecting the image quality occur when the microscope image is acquired by a sensor. For image acquisition a TV-camera is used. Such cameras are equipped with a tube usually showing a spatially uneven sensitivity, resulting in shaded images under homogeneous illumination. Also, when the sensor is covered, a certain output level may be measured, known as the black level response. In addition, TV-tubes are known to possibly have a non-linear response to illumination [Batchelor85]. The TYC9A-SIT and SIT-66 cameras used in this investigation showed all three effects. Linearity between illumination intensity and camera response is a pre-requisite for the type of quantification wanted in this study, where image addition and subtraction are necessary operations (see chapters 3 and 6). Therefore, the raw images as are produced directly by the camera are unsuitable. In chapter 4, restoration of the images is discussed.

Since the probability of inelastic scattering is low and the energy distribution is wide, the number of electrons contributing to image formation in energy-filtered imaging in other regions than the zero- and low-loss region is severely limited. As a consequence, such images are corrupted by noise, expressing the uncertainty of the observed intensity over the limited observation time. Because the camera is an electronic system, this device acts as a second source of noise.

In addition to these phenomena, affecting the brightness transfer to the final image, the detection system further reduces the spatial resolution. Before the image is projected on the camera sensor, it is converted by a scintillator screen from an electron image to a visible-light image. The composition and grain size of the powder on the screen and the thickness of the layer determine the efficiency of electron-photon conversion and resolution [Chapman89]. In the EM 902, the scintillator consists of ZnS, which, according to Zeiss [Roß-Meßmer93], was optimized for resolution, being about 60 lp/mm [Zeiss]. The screen image is projected 1:1 through a lens with a resolving power of 100 lp/mm onto the TV-sensor having dimensions of 12.8x9.6 mm. Theoretically, about 30 lp/mm can be resolved in the sensor plane with 768x512 digitization, not violating the Nyquist criterion [Oppenheim83]. In practice, camera resolutions are lower. For the Bosch camera, a 5 MHz resolution at 20% modulation depth is specified in response to a bar pattern (illumination level not specified),

Chapter 2

while the theoretical limit lies at 7 MHz in the case of 768x512 digitization. This suggests a resolution of 20 lp/mm along video lines. Dage-MTI Inc. expresses the resolution, also in response to a square wave pattern, in terms of resolved TV-lines. This, apparently, is dependent on the absolute light level. In [Tsay90], the resolution of the SIT-66 camera was measured at an illumination level of 10^{-3} lux, resulting a value of 212 TV-lines at 50% contrast transfer. For the same light-level, a resolution of 340 TV-lines was specified. The difference between the two values may be explained by the adoption of different contrast transfer levels for determining the resolution cut-off point. In general, under low light-level conditions, such as present during the acquisition of spectroscopic image sequences, about 1/3 to 1/2 of the optimal performance of 700 lines can be reached, which is equivalent to 12-18 lp/mm in the sensor plane. From these considerations it is concluded that the screen and lens do not limit the resolution. The electronic image produced by the camera is degraded in such a way that under the current conditions, 768x512 image digitization fulfils the Nyquist criterion of sampling in the (horizontal) scanline direction, irrespective of the contents of the projected image. For the vertical direction, this depends on the frequency contents of the projected image, which ultimately is determined by the microscope aberrations.

Another resolution limiting factor is drift at the specimen level. As a result of heating and radiation damage, the unsupported ultra-thin sections used are likely to tear or deform during image acquisition. Depending on the acquisition time, not only may blur be observed, but also, when spectroscopic sequences are acquired, the pixel locations in the consecutive images may have lost correspondence. Specimen drift is considered unacceptable for quantitative ESI. Possibilities for the correction of specimen drift are further discussed in section 4.2. Drift along the E-axis is specified by the manufacturer to be ≤ 0.2 eV/minute. This has been verified and is considered to be of minor importance since the acquisition time of a series is usually less than about 5 minutes.

Chapter 3. Principles of quantification

3.1 Quantification in electron spectroscopic images

Chapter 2 describes the perspective of using spectral information for quantification (eq. (2.2)). The energy-differential cross-section, however, is not precisely known and varies with the local chemical composition. Rather than addressing one sample in the spectral edge-region in relation with the energy differential cross-section as in eq. (2.1), the whole edge is considered in correspondence to the integrated or total inelastic cross-section. Rewriting eq. (2.2), taking the section thickness t into account, gives an expression for the atomic concentration, i.e. the number of atoms of a certain element x per unit volume:

$$N_x = \frac{I_k(\beta)}{I_T(\beta) \cdot \sigma_k(\beta) \cdot t} \quad (3.1)$$

The total edge intensity $I_k(\beta)$ and the total spectrum intensity $I_T(\beta)$ are quantities to be obtained from integration over the appropriate regions in the spectrum. As described in section 2.2, I_k and I_T refer either to intensities measured in a true spectrum or to equivalent quantities obtained from the greyvalues of corresponding pixels in a sequence of spectroscopic images. Spectra and spectroscopic images are rarely acquired over the entire spectral range. The extraction of $I_k(\beta)$ is problematic and inaccurate (e.g. due to the presence of other edges). For these reasons, an approximation of eq. (3.1) is used in practice. Following [Egerton86], we consider the intensity $I_k(\beta, \Delta)$ in the spectral edge region, integrated only over a width Δ from the onset of the edge, in relation to the intensity $I_T(\beta, \Delta)$ in the zero and low-loss region, integrated up to an energy-loss Δ :

$$N_x = \frac{I_k(\beta, \Delta)}{I_T(\beta, \Delta) \cdot \sigma_k(\beta, \Delta) \cdot t} \quad (3.2)$$

where $\sigma_k(\beta, \Delta)$ is the partial cross-section, which is the energy differential cross-section integrated over Δ . This is the central quantification expression used in this thesis, which may be used in situations where the specimen thickness is less than the plasmon mean free path: $t < \lambda_p$ and Δ is sufficiently large to include a representative sample of the edge-intensity. Let:

$$R(k, \beta, \Delta) = \frac{I_k(\beta, \Delta)}{I_T(\beta, \Delta)} \quad (3.3)$$

be the ratio to be obtained from the spectrum. With $R_x(k, \beta, \Delta)$ determined for shell k of element x , eq. (3.2) rewrites to:

Chapter 3

$$N_x = \frac{R_x(k, \beta, \Delta)}{\sigma_k(\beta, \Delta) \cdot t} \quad (3.4)$$

This is merely a different notation of the quantification expression eq. (3.2), in which the quantities obtained from the spectrum are combined in R_x and separated from the other quantities.

In practice, eq. (3.4) is evaluated along the following lines. Because $R_x(k, \beta, \Delta)$ is composed of only spectral quantities, eq. (3.3) is applied pixelwise. An ESI-sequence is thus treated as a set of spectra. $I_T(\beta, \Delta)$ is obtained directly from images acquired in the zero- and low-loss region. From the independence of scattering events, $I_k(\beta, \Delta)$ may be considered as a quantity that is superimposed on a background in the spectrum. Therefore, the determination of $I_k(\beta, \Delta)$ requires a process to subtract the aspecific background. This implies that in addition to a number of edge images, also background related images have to be acquired. The superimposition of the ionization edges on a background is nicely observed in spectra such as in Fig. 2.2, while the separation of the two quantities is visualized in Fig. 6.1. The partial cross-section is a constant under the given conditions and can be determined from electron scattering models [Leapman80, Ahn85, Egerton86]. However, the results from these models are still subject to discussion [Auerhammer89, Hofer91]. Therefore, internal standards are frequently used for reference. Because the embedding and sectioning of such standards with biological tissue is feasible [Bruijn85b], the determination of t can also be avoided. Section 3.2 treats this approach to quantification in more detail.

For background subtraction, two fundamentally different approaches are reported in the literature. The model-based approach uses knowledge about spectral characteristics of the background. Although, unfortunately, no universal model exists, in major parts of the spectrum a background behaviour proportional to E^{-r} (with r as a parameter) is predicted and observed. The model-based approach is further discussed in section 5.2. Recently, the application of the formalism of correspondence analysis for background subtraction has been described [Hannequin88, Trebbia90a&b, Bonnet92a&b, Gelsema92&94]. This technique does not assume any physical model, which makes it attractive as a more general tool. Trebbia applied the formalism to calculate distribution images directly from a spectroscopic image sequence, implicitly correcting for the background. The result, however, only has a qualitative meaning. Bonnet and Gelsema, interested to obtain quantitative results, adapted the formalism to obtain an explicit estimation of the background, which is subsequently subtracted. Although promising steps have been taken towards the use of correspondence analysis for element quantification, a definitive proof is still awaiting.

3.2 The role of internal standards for quantification

When the objective of measurement is the goal-directed assessment of the quantities of particular elements, internal standards containing these elements can be embedded with the specimen and sectioned. De Bruijn [Bruijn85b] advertised the use of Chelex Bio-standards,

which are ion exchange beads, consisting of an organic-like matrix. These resins, about 30-75 μm in size, are available in two versions, one for loading with anions, the other for loading with cations. Using such standards, quantification now comprises the measurement of the element in both the unknown and in the standard (s), which is reflected by an adaptation of eq. (3.4) to:

$$N_x = \frac{R_x(k, \beta, \Delta)}{R_{x,s}(k, \beta, \Delta)} \cdot N_{x,s} \quad (3.5)$$

where the measurement of the standard eliminates both $\sigma(\beta, \Delta)$ and t , provided it is performed in the same section, with the same thickness. $N_{x,s}$ refers to the atomic concentration of the element loaded into the standard. Since $R_{x,s}(k, \beta, \Delta)$ stands for the partial cross-section, the conditions for which it is determined should be the same as those used for $R_x(k, \beta, \Delta)$, i.e. with equal values for β and Δ . As long as the conditions are the same and the section thickness may be assumed constant, the calculation of $R_{x,s}(k, \beta, \Delta)$ needs to be done only once per section.

The atomic concentration in the standard is determined by neutron activation [Sorber91b]. This analysis gives a concentration value C_x for the loaded standard-element in weight percentages and has to be converted to the atomic volume concentration. From [Sorber91b], the following equation is obtained:

$$N_{x,s} = \frac{\rho C_x N_A}{m_x} \quad (3.6)$$

where ρ is the mass density of the standard, m_x the atomic mass of the element and N_A Avogadro's constant. To give an impression of the magnitude of $N_{x,s}$, the frequently used iron-loaded Chelex Bio-standards, with 12.9 % (w/w) iron and $\rho=1.18 \text{ g/cm}^3$ contain $N_{\text{Fe},s}=1.64$ atoms Fe/nm^3 .

In addition to the already mentioned advantages of using standards, it may be expected that radiation damage effects are (partly) cancelled, because of the comparable measurement conditions. Since eq. (3.2) is an approximation of the actual quantification expression eq. (3.1) it was established that in the case of multiple scattering, eq. (3.2) gives erroneous results. Particularly, eq. (3.3) tends to yield too low values if t approaches the mean free path for inelastic scattering (see chapter 7). Reduction of this bias may also be expected, using an internal standard.

3.3 Specimen thickness

In order to assess the validity of the application of the quantification equations, the specimen thickness should be monitored in relation to the mean free path of the plasmons, in the remainder of this thesis referred to by λ . Rather than obtaining the section thickness and mean free path separately, the scattering parameter t/λ can be determined more directly. An

Chapter 3

estimation for this quantity is obtained in the low-loss region of the spectrum from [Egerton87]:

$$t/\lambda = \ln \frac{I_t(\beta, \Delta_2)}{I_0(\beta)} \quad (3.7)$$

where $I_t(\beta, \Delta_2)$ is the total area under the spectrum, truncated at Δ_2 energy-loss and $I_0(\beta)$ is the zero-loss intensity. As a rule of thumb, Δ_2 is taken about 100 eV wide, above which the spectral intensity becomes negligible. Since I_T in eq. (3.3) and I_t in eq. (3.7) are to be evaluated at the same locations and the Δ - and Δ_2 -regions overlap, these measurements in the zero- and low-loss region can be combined.

Chapter 4. Image restoration

4.1 Shading and gamma-correction

In this section, two types of imaging distortions are discussed: shading and camera non-linearity. Within the context of quantification it is analyzed to what extent corrections have to be performed.

4.1.1 Shading

Shading is prominently visible in the acquired TV-images. In general, it originates from the uneven sensitivity of the camera tube and non-homogeneous illumination, e.g. caused by the optics. In addition to these multiplicative effects, a significant additive component in the form of a dark-level response can be present. Together, these phenomena may be described by a linear model [Kate90b], with two parameters. The values for these parameters may be estimated from two independent recordings of an empty microscope field with known intensity relations and the inverse is easily calculated. The amount of shading has been found to depend on the camera gain. Since the parameters are to be used for image correction, they must be calculated for each set of acquisitions under fixed conditions.

4.1.2 Camera non-linearity

Another, although less visible effect, is the non-linear response of the camera system. TV-tubes are known to have a photometric response of the following form [Batchelor85]:

$$I_{out} \sim I_{in}^{\gamma} \quad (4.1)$$

I_{in} represents the intensity of the incoming light and I_{out} the output signal. The parameter γ describes the non-linearity. In the case of quantitative ESI, non-linearities in the intensity recordings are unwanted, because after spectral background correction, the relation between the net signal intensity and concentration will be unknown. Therefore, the influence of γ should be removed prior to any further processing. Measurements performed with the cameras used in this investigation (from Bosch and Dage-MTI) revealed that for the Bosch camera the average γ -value varies from 0.8-1.0, while a slight dependency exists on the location in the camera field. For the Dage-MTI camera, γ was around 1.1 and rather constant over the field. The γ -value of the Bosch camera depends on the gain level, while also in this respect the camera from Dage-MTI gave an almost constant result. A dependence on the camera gain implies that, in principle, for each recorded data set (for which the camera has been newly adjusted), the γ -value has to be determined.

Chapter 4

4.1.3 Corrections

Based on the previous findings, the combination of photometric sensitivity and shading can be described by the following model:

$$I_{out}(x,y) = K'.c'(x,y).I_{in}^{\gamma}(x,y)+b(x,y) \quad (4.2)$$

where K' is the global gain of the system, $b(x,y)$ the local black-level; the multiplicative shading component $c'(x,y)$ is expressed as a local attenuation factor ($0 \leq c'(x,y) \leq 1$). The local light intensity can be reconstructed by the inverse model, expressed by:

$$I_{rec}(x,y) = \frac{1}{K.c(x,y)}.[I_{out}(x,y)-b(x,y)]^{\frac{1}{\gamma}} \quad (4.3)$$

Note that K and c are the γ -corrected versions of K' and c' , respectively. The local values for b are obtained when the sensor is covered. The value for γ is determined using optical filters with density D_1 and D_2 to acquire the images I_1 and I_2 corresponding to known relative illuminations. In each pixel one calculates:

$$\gamma = \frac{\log \frac{I_1 - b}{I_2 - b}}{D_2 - D_1} \quad (4.4)$$

Subsequently, γ is averaged over the image plane. The local values for c are obtained from the difference of a homogeneously illuminated image and a dark one, correcting it for γ and normalizing it on the maximum value. The reference images used for correction should be noise-free to prevent image quality reduction. Note that calculation of the image $c(x,y)$ and of parameter γ , in relation with the acquisition of the corresponding reference images, is necessary each time the camera gain setting has been changed. The policy behind the image acquisition protocol (section 8.2), using optical filters to regulate the image brightness, is that the camera gain is optimized at the beginning of the acquisition of an image sequence and held constant thereafter, for that sequence. Thus, $c(x,y)$ and γ are calculated once per sequence.

Considering eq. (3.3), it can be understood that if the same multiplicative distortions are present in both I_k and I_r , corrections for these effects can be omitted. Using the optical filters for attenuation we have such a case, since the conditions for all images are the same. Thus, only black-level and γ -corrections are necessary and should be carried out on all the data before background correction, irrespective of the actual technique used. For other purposes, full correction may be necessary, or shading correction only as is the case when calculating the specimen drift.

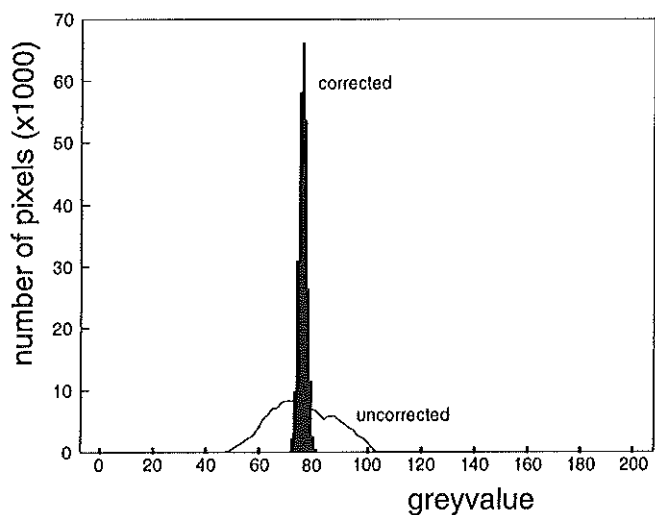


Figure 4.1 An illustration of the effectiveness of linear shading correction. A homogeneously illuminated image was obtained from the SIT-66 camera and the histograms were determined before and after correction.

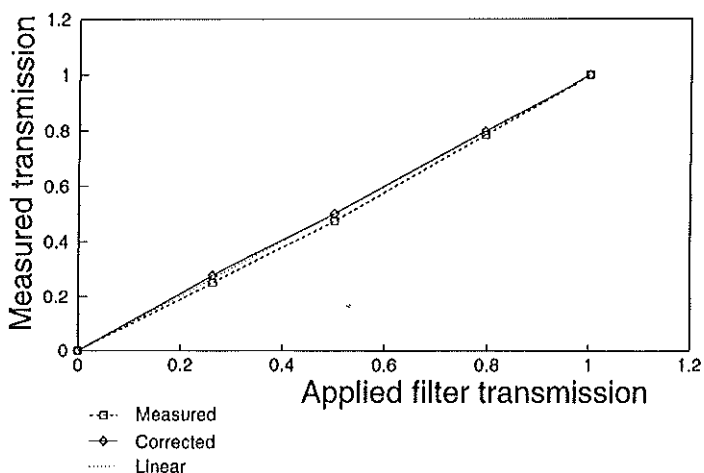


Figure 4.2 Gamma-correction applied to a series of images with known relative illumination levels. The SIT-66 camera was used for image acquisition.

Chapter 4

4.1.4 Experimental results of correction

Fig. 4.1 shows the effectiveness of the correction for shading based on the linear model. The greyvalue histograms are obtained from a homogeneously illuminated image acquired with the SIT-66 camera and the situations before and after correction are compared. The standard deviation of the image's greyvalue distribution is reduced from 11.8 to 1.6. Of the remaining variation, about 50% can be explained as rest-shading and 50% by the presence of some noise. Images acquired with the TYC9A SIT camera show a more severe rest-shading, especially in the corners. Fig. 4.2 illustrates the effect of γ -correction in an experiment with the SIT-66 camera to measure the transmission values of a series of attenuation filters, based on the acquired greyvalues. The first set of points (marked \square) is for the uncorrected data, the second set (\diamond) is corrected for offset and γ according to eq. (4.3) and closely approximates the expected linearity.

4.2 Specimen drift correction

Specimen drift is a common problem in electron microscopy [Cattermole91]. Drift impairs deformation onto the three-dimensional ESI sequence, which consequently needs to be corrected. The drift is observed to be translational. Cross-correlation between images potentially yields drift vectors in combination with peak-finding [Ballard82]. As the images in an ESI-sequence are obtained at different energy-losses, the image content changes through the sequence. As a consequence, correlation between the images is never 100%. In images obtained in the low-loss region, the contrast is inverse as compared to the contrast in images taken at higher energy-losses and thus, the correlation function also inverts. Shading correction is considered essential, prior to image correlation. A standard procedure for image cross-correlation was implemented, based on the use of image patches (e.g. 64x64 pixels). A simple peak finding algorithm is then applied from which the translation vectors are determined. The results are good when sufficient contrast is present and structures with various orientations compose the sub-images. Occasionally this is not the case, leaving manual correction as an alternative option. As the spectroscopic images are usually acquired as a time sequence, a certain time relation exists. If deformation is assumed to originate mainly from thermal heating, the displacements may be described by a smooth function. The sequence of drift vectors is always inspected for outliers. When such deviations are found, the vectors judged unreliable are discarded and replaced by an interpolated value. The errors related to this interpolation step are small since interpolation was necessary only when the automatic procedure failed due to the absence of contrast. An increase in integration times for image acquisition in the presence of drift yields images that are blurred to a certain extent. This effect is currently not corrected, but such a correction may be feasible using inverse filtering [Gonzalez87]. Abrupt changes in the specimen such as tearing generally yield unusable data sets which have to be discarded.

Chapter 5. Image modelling

5.1 Spectral models and spectroscopic images

For ESI, models are applicable in two types of situations. Descriptive models are of importance for quantification and understanding spectral fine structure, while generating models are of use for producing artificial sets of spectroscopic images. Artificially generated image sequences are particularly relevant for testing new algorithms for spectral background correction and quantification [Pun85, Sorber91a, Gelsema92].

A spectroscopic image sequence (section 2.2) may be interpreted as a two-dimensional set of spectra. Therefore, models for spectra also apply to spectroscopic images. With a generating spectral model, artificial objects, e.g. structures of a distinct chemical composition, can be synthesized by expanding certain spectral characteristics over two dimensions.

Because a spectrum is a reflectance of the additively combined energy-differential cross-sections corresponding to the various inelastic scattering events, from a modelling point of view these aspects may be addressed separately. Interactions with inner-shells are described by various models with different degrees of accuracy [Auerhammer89, Hofer91]. The partial cross-sections obtained by these models are frequently used for quantification, while the energy-differential behaviour assists in understanding spectra. For generating spectroscopic images such models are rarely used and ionization events are more simply modelled by a Gaussian function [Sorber91a] or a step function [Pun85, Gelsema92]. The ionization edges are superimposed on a background, of which the intensity decreases with increasing energy-loss. For energy-losses larger than approximately 100 eV and over limited energy-loss ranges, not too close to the near-edge decay of previous edges, the background may be described by the power-law [Egerton86]:

$$f(x,y,E) = A(x,y).E^{-r(x,y)} \quad (5.1)$$

where the energy-loss is expressed by E , and A and r are parameters depending on the location (x,y) . A and r vary with the local composition and section thickness of the specimen. The spectral background behaviour originates from the tails of low-loss interactions (e.g. plasmons) and is predicted by the Bethe theory of inelastic scattering [Egerton86]. The validity of eq. (5.1), within the limitations mentioned above, has been confirmed experimentally.

With the power-law as a model for the energy-differential behaviour of the background, and using an energy-dependent step-function to model an edge, the following function generates an artificial spectrum around an ionization edge at $E=E_{IE}$:

$$f(E) = A(1+\epsilon)E^{-r} \quad (5.2)$$

with $\epsilon=0$ if $E < E_{IE}$ and $\epsilon > 0$ for $E \geq E_{IE}$. An example of a generated spectrum is shown in

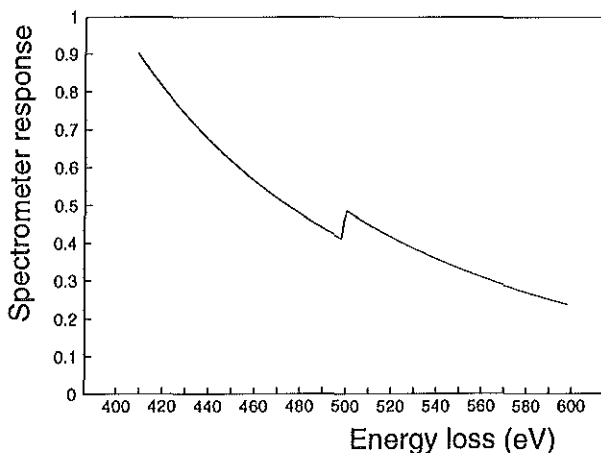


Figure 5.1 An example of an artificially generated spectrum.

Fig. 5.1 with $E_{IE}=500$ eV, $r=4.0$ and $\epsilon=0.2$. Using the same model, a spectroscopic image sequence was created with a circular object, see Fig. 5.2. The object is circular, the outer ring of which is supposed to contain some element. Since the object in this example is presumed to have a higher mass than its surroundings, the A- and r-values are dependent on the location. In the circular object area $r=3.6$, in the background area $r=4.0$ and in the element area $r=3.6$ and $\epsilon=0.2$. The A-value in the object and element regions is 20% higher than in the background region. The result is that object contrast is visible in all images, while element contrast is only observed in the edge images. Because the probabilities of inelastic interaction are low in practice, real images are formed with only a limited number of electrons. Consequently, the images are noisy. In order to faithfully generate image sequences comparable to real images, noise has to be added. The statistical characterisation of images is addressed in section 5.2. Artificial noisy sequences have been used in [Gelsema92, Gelsema94] for evaluating techniques based on correspondence analysis for background correction.

The power-law model can also be used effectively for background correction for quantification. Following this approach, in each pixel location in an image we have two unknown parameters A and r which requires minimally two images in the pre-edge region to be acquired for their estimation. When the model is parametrically adapted to the local conditions, the function is extrapolated to the edge region to enable subtraction of the background contribution from the total edge intensity. To account for and reduce the effect of noise, usually more than two pre-edge images are used for correction. This makes background correction a statistical problem, which will be further elaborated in chapter 6.

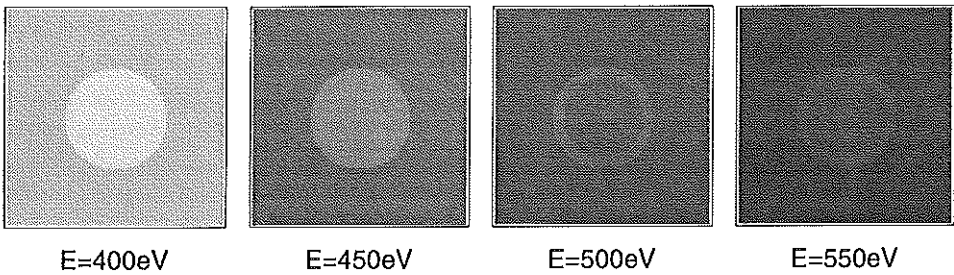


Figure 5.2 A sequence of generated spectroscopic images with an element containing ring structure in a circular object. Element contributions are only seen in the edge images. Note the decay of the spectral background intensity.

5.2 Characterization of image statistics

After energy filtering, the electrons are detected in two stages, using a scintillator screen and a TV camera. The influence of this combination on the recorded greyscale values in relation to the incoming electrons is investigated here in a statistical sense.

5.2.1 The combination of scintillator screen and TV-camera in the acquisition system

The scintillator on the screen and the TV-camera are in a way separate integrating components in the acquisition system. The scintillator is excited by an incoming electron and produces an amount of light in a period of time thereafter with a decay profile that depends on the composition of the screen. Newly incoming electrons excite the scintillator more and add to the decaying amount of light already produced. Therefore, the screen can be seen as an integrator that forgets according to the decay profile. The TV-camera is typically equipped with a true integrating sensor, accumulating the incoming photons produced by the screen over a period of time that is related to the video frame rate. As a consequence, the combination of the two components cannot be seen as a true counting device. This poses the question of the relationship between the camera signal and the incoming intensity of the beam of electrons. A second important question is, how to describe the image statistics. Due to the described nature, the Poisson statistic seems inappropriate.

5.2.2 The relation between electron beam intensity and camera output

The decay profile of the scintillator screen in our electron microscope may be described by a first order system, with an impulse response proportional to $e^{-t/\tau}$, with time t and τ a time constant. The incoming stream of electrons is a stochastic signal which is convolved with the impulse response of the screen to obtain the light response. The light-intensity is then integrated by the camera over an interval of length T and subsequently digitized. The resulting greyscale value may be regarded as a weighted addition of preceding electron contributions, and

Chapter 5

the average value can be calculated up to an unknown scaling constant. Re-scaling the greyvalues such that the new values have an average of μ_y equal to the variance, as is done in appendix A5.1, it can be shown that the following relation holds: $\mu_y = f_{\tau,T} \cdot \mu_T$, where μ_T is the average number of counts that would be recorded if the incoming electrons were directly detected during the interval T and $f_{\tau,T} = [1 - \tau/T(1 - e^{-T/\tau})]^{-1}$. The factor $f_{\tau,T}$ is a constant for the given situation and may be regarded as a prolongation of the camera integration time to effectively: $T_{eff} = f_{\tau,T} \cdot T$. Numerical values of the integration constants for our system are: $\tau = 17$ ms and $T = 40$ ms, giving $f_{\tau,T} = 1.6$ if one image is acquired. Real-time digital addition of multiple (n) camera frames is simply expressed by taking nT for the camera integration time. For larger n , the role of the screen as an integrating component diminishes. It can be concluded that the greyvalue produced by the camera is proportional to the intensity of the electron beam hitting the screen and that due to this screen the integration time is effectively somewhat longer than would be expected from the TV-frame rate.

5.2.3 Image statistics

Noise is inherent to electron spectroscopic images and originates mainly from the fact that only a limited number of electrons is available to compose the image. The local image noise distribution plays an important role in the process of background correction using the methodology of statistical parameter estimation [Bos82]. This will be explained further in chapter 6. Although Poisson-distributed data initially would be expected, based on the described situation with two integrators, this is unlikely to be the case for the data produced by the camera. For spectra, in [Puymbroeck92] it was first recognized that EELS data obtained with the EM902 has a non-Poissonian distribution. In [Xhoffer93] this was also established for energy-filtered images. The problem of the determination of the actual distribution was put forward. Unfortunately, we were also unable to derive an explicit expression for the true probability distribution of the image greyvalues. It is shown in section A5.3, however, that if the greyvalue of one pixel is denoted by y , the variance of the distribution of y is simply related to the average value μ_y by a factor α : $\sigma_y^2 = \alpha \cdot \mu_y$, where α depends on τ , T and the system gain only. In practice, the gain is modulated by the shading $c(x,y)$, thus the variance in the observed data (corrected for offset and γ) is more precisely given by:

$$\sigma_y^2(x,y) = c(x,y) \cdot \alpha \cdot \mu_y(x,y) \quad (5.3)$$

Conversely, the unknown factor α can be estimated with this equation when the shading is measured separately as described in section 4.1 and the average and variance are estimated from e.g. two or more statistically independent instantiations of the same image:

$$\alpha = \frac{\sum_{(x,y)} \sigma_y^2(x,y)}{\sum_{(x,y)} c(x,y) \cdot \mu_y(x,y)} \quad (5.4)$$

For this moment we postulate that the distribution in each pixel can best be approximated by a normal distribution. A second reason for this choice is that in addition to the signal noise, in practice also system related noise is present in the data, giving a convolution of the two distributions. The system noise component is smaller in magnitude and depends on the camera system gain.

5.2.4 Experimental results

From a theoretical point of view it was stated earlier in this section that the variance in each pixel is linearly proportional to the average greyvalue. This relationship has been investigated in practice. A set of homogeneously illuminated images was acquired at a fixed camera gain-level with magnification factors of 3,000, 4,400, 7,000 and 12,000 times. In this way an image sequence is obtained at four different intensity and noise levels. The measured greyvalues are corrected for shading and camera γ following the procedure described in section 4.1.3. After correction, the greyvalues are proportional to the incoming electron intensity. Image mean and variance were calculated. The variance of the system noise was subsequently subtracted from the obtained variance values. The results are shown in Fig. 5.3. Comparison with the regression line shows that the correlation is high ($R=0.995$). The vertical intercept is calculated to be -0.01 . The results from this experiment support the linear relationship as derived theoretically in eq. (5.3).

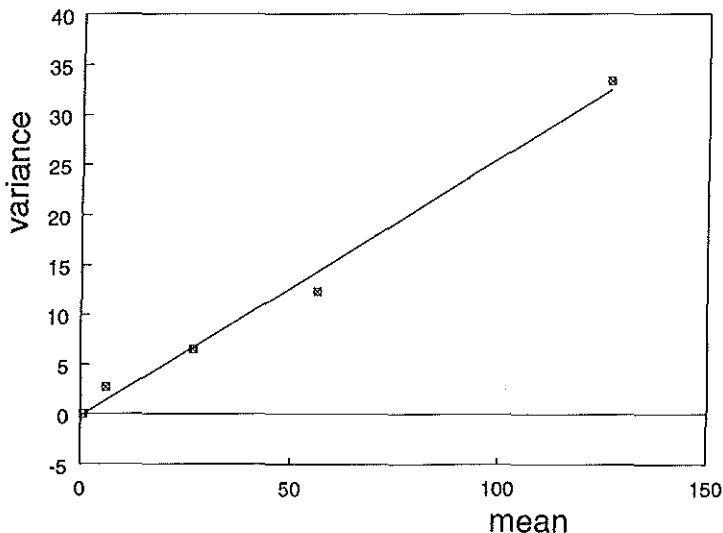


Figure 5.3 The relation between greyvalue mean and variance, measured from a series of homogeneously illuminated images at different intensity levels.

APPENDIX A5

A5.1 Derivation of the relationship between electron beam intensity and greyvalue

The detection of electrons takes place in two stages. First, the incoming electrons interact with the scintillator on the screen which produces an amount of light and subsequently this light is collected by the sensor. After interaction of one electron with the screen, the total number of photons produced depends on the energy of the electron, the conversion efficiency and the thickness of the scintillator [Chapman89]. The conversion process is not instantaneous, but follows a time dependent decay profile $D(t)$, characteristic for the composition of the screen. The sensor is assumed to be of the integrating type, collecting photons over a fixed interval of time T . The purpose of this section is to derive a relationship between the sensor read-out (in terms of camera greyvalues) and the intensity of the incoming electron beam.

Consider the situation of electrons in a beam along the time-axis. This axis is subdivided into micro-intervals such that an interval of length T consists of N micro-intervals, each with length t_i . This latter size can be chosen such that at most one electron is present in each micro-interval with probability p . Consequently, p will be small. The average number of electrons in time-interval T is μ_T , thus with a time average of $\lambda = \mu_T/T$. The statistical distribution, describing the probability of finding k electrons in a micro-interval is binomial: $p(\underline{x}=k) = p^k(1-p)^{1-k}$, with effectively $k=0,1$, and $\mu_x = p$ and $\sigma_x^2 = p$. Looking at a chronological series of micro-intervals, the electron pulse stream can be regarded as a stochastic signal $\underline{x}[i]$ with $\mu_x = \sigma_x^2 = p$ ($p \ll 1$). The average number of electrons hitting the screen during time T can also be expressed as $\mu_T = p.N$, which is equal to $\lambda.T$ (with $p = \lambda.t_i$), as was defined before and the variance is $\sigma_T^2 = p.(1-p).N \approx p.N$, equal to the expected value. The actual number of screen hits over the interval T is known to follow a Poisson distribution. It is noted that if \underline{x} is considered as a discrete time signal, its average is p . Regarded as a continuous time signal, the average is λ , using the conversion $p/t_i = \lambda$.

An electron produces an amount of light on the screen according to the decay profile and this light is integrated by the sensor. The exact amount of light actually sensed depends on the moment in time i that the electron hits the screen (arrival time), relative to the integration period (see Fig. 5.4). Electrons that hit the screen during the period of integration T , but also electrons that have hit the screen before this period, contribute independently to the sensor read-out by an amount a_i . The total signal intensity is expressed as a weighted addition of all these events:

$$y = \sum_i a_i \cdot \underline{x}[i] \tag{A.1}$$

The stochast \underline{y} is assumed to produce the signal $y[k]$ from independent samples, i.e. from samples with sufficient distance on the time-axis. The expected value of $\underline{y}[k]$ is therefore expressed by:

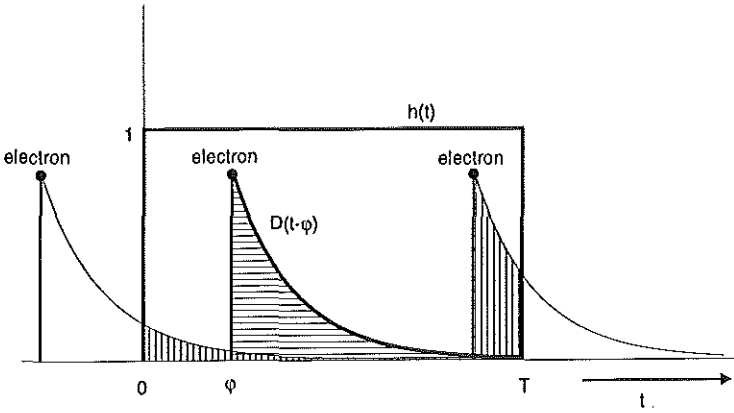


Figure 5.4 Light intensity decay of the scintillator screen after excitation by electrons. $h(t)$ represents the time interval of length T during which the camera is active in integrating the light contributions.

$$\mu_y = E\gamma = \sum_i a_i E_x[i] = \mu_x \sum_i a_i \quad (\text{A.2})$$

and its variance is given by:

$$\text{var}\gamma = \sum_i a_i^2 \text{var}x[i] + \sum_{j \neq i} \sum_i a_i a_j \text{cov}(x[i], x[j]) \quad (\text{A.3})$$

The independency of the events in each micro-interval implies that for $i \neq j$: $\text{cov}(x[i], x[j])=0$, thus:

$$\text{var}\gamma = \sum_i a_i^2 \text{var}x[i] \quad (\text{A.4})$$

The intuitively expected behaviour of the photon yield being proportional to the incoming electron beam intensity is confirmed by eq. (A.2), independent of the shape of the decay function. An increase of the intensity can be expressed either as an increase of p ($E_x[i]=p$), with the same number of micro-intervals and still under the condition that p is sufficiently small, or as a proportional increase of the number of electron containing micro-intervals, given a constant value for p . The mapping of the electron beam intensity onto the greyvalue scale involves a global system gain factor (screen efficiency, camera gain, A/D-conversion, etc.) which may be assumed to be implicitly absorbed in the factors a_i . This gain factor is generally not known and also not constant since it varies with the camera gain. This means that, unless

Chapter 5

the gain is somehow determined, the greyvalues cannot be calibrated directly.

A possibility for internal calibration is to scale the greyvalues in such a way that the mean and variance will be equal. In other words, choose κ such that with

$$z[k] = \kappa \cdot y[k] \quad (\text{A.5})$$

$\mu_z = \text{var}_z$. It can easily be derived that $\kappa = \mu_y / \text{var}_y$. Thus, combining eqs. (A.2) and (A.4) with eq. (A.5) yields:

$$z[k] = \frac{\sum_i a_i}{\sum_i a_i^2} \cdot y[k] \quad (\text{A.6})$$

with an expected value:

$$Ez[k] = \frac{(\sum_i a_i)^2}{\sum_i a_i^2} \cdot p \quad (\text{A.7})$$

In practice, the continuous time equivalent is more easily computable, giving:

$$Ez(t) = \frac{(\int a(t)dt)^2}{\int a(t)^2 dt} \cdot \lambda \quad (\text{A.8})$$

For a first order screen, the weight factors $a(t)$ and their integrals are derived in appendix A5.2. Substitution in eq. (A.8) results in:

$$\mu_z = \frac{T}{1 - \frac{\tau}{T}(1 - e^{-\frac{T}{\tau}})} \cdot \lambda \quad (\text{A.9})$$

Eq. (A.9) shows that the sensed result is systematically larger than the count result over period T ($\mu_y = \lambda \cdot T$) by a factor of $[1 - \tau/T(1 - e^{-T/\tau})]^{-1}$. This can be regarded as a prolongation of the integration time T due to the combination of two integrating components in the acquisition chain. If in practice both the mean and the variance of the distribution of greyvalues in each pixel can be determined, then normalizing the greyvalues in the way described above creates a simple link between camera greyvalue and the number of light producing electrons, which is a measure for the beam intensity. An interesting question that remains is, what the distribution of z is.

A5.2 Light-production weights for the combination of a first order scintillator screen and an integrating sensor

For the case of a scintillator screen with an exponential light decay after excitation, the weighing constants are calculated, describing the light contributions of electron screen hits to the (integrated) sensor output value. Consider Fig. 5.4; two situations are distinguished: electron hits during integration ($\varphi \geq 0$) and electron hits before starting the integration period ($\varphi < 0$). The decay profile of the screen in response to an electron hit is given by:

$$D(t) = \frac{1}{\tau} e^{-\frac{t}{\tau}} \quad (t \geq 0) \quad (\text{A.10})$$

The sensor integrates from $t=0$ to $t=T$, which is formally described by the function:

$$h(t) = 1 \quad (0 \leq t \leq T) \quad (\text{A.11})$$

The amount of light contributing to the sensor output value can now be formulated as:

$$a(\varphi) = \int_{-\infty}^{+\infty} h(t) \cdot D(t-\varphi) \cdot dt \quad (\text{A.12})$$

Substituting the functions and evaluating the integrals yields:

$$\begin{aligned} a(\varphi) &= \int_0^T \frac{1}{\tau} e^{-\frac{t}{\tau}} \cdot dt = \left[e^{-\frac{\varphi}{\tau}} - e^{-\frac{T-\varphi}{\tau}} \right] \quad (\varphi < 0) \\ a(\varphi) &= \int_{\varphi}^T \frac{1}{\tau} e^{-\frac{t}{\tau}} \cdot dt = \left[1 - e^{-\frac{T-\varphi}{\tau}} \right] \quad (0 \leq \varphi \leq T) \end{aligned} \quad (\text{A.13})$$

This function is shown in Fig. 5.5. The first part ($\varphi < 0$) describes light contributions from electron events before the start of the sensor integration period, the second part ($0 \leq \varphi \leq T$) describes the amount of light generated by electron hits during integration. For comparison the figure shows the rectangular function describing a counting detector.

For the calculation of the average values of the sensor response as in eq. (A.8), the integrals of $a(\varphi)$ and $a(\varphi)^2$ are needed. Using eq. (A.13), the first integral results in:

$$\int_{-\infty}^T a(\varphi) \cdot d\varphi = T \quad (\text{A.14})$$

and the second gives:

Chapter 5

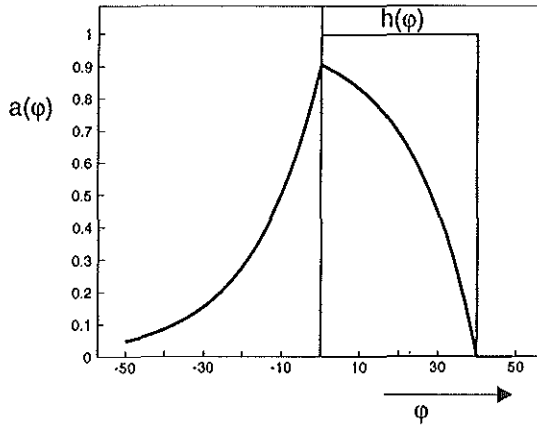


Figure 5.5 Contribution $a(\varphi)$ of an electron hit on the screen to the light intensity sensed by the camera, depending on its time of hit φ ($T=40\text{ms}$, $\tau=17\text{ms}$). Similarly, $h(\varphi)$ denotes the case of a counting detector.

$$\int_{-\infty}^T a(\varphi)^2 d\varphi = T - \tau + \tau e^{-\frac{T}{\tau}} \quad (\text{A.15})$$

Note that $a(\varphi)$ and the derived results have only a relative meaning, since the overall system gain is neglected in the expressions.

A5.3 The relationship between mean and variance of image greyvalues

For the weighted least-squares estimation of the spectral background it is required to know the variance of each measurement value. Repeating the measurements is one solution to estimate the variance. It is, however, very cumbersome to collect a sufficient amount of data and the stability of the relevant acquisition conditions is questionable. Therefore, it is investigated here whether the variance can be derived from the mean for which an estimate is given more easily (i.e. by the measurement value itself).

Eqs. (A.2) and (A.4) reveal that with $\mu_x = \sigma_x^2 = p$, the relation between mean and variance of the uncalibrated greyvalues is:

$$\text{var } y = \frac{\sum_i a_i^2}{\sum_i a_i} \mu_y \quad (\text{A.16})$$

This means that the variance is linearly proportional to the expected value. As explained

above, the absolute values of the constants $a(\varphi)$ depend on the system gain which is generally not known. If in practice both the mean and the variance can be estimated for a certain system gain, which is then kept constant, the obtained proportionality constant includes the gain and can be used generally for calibration under this condition.

Only two image instantiations are needed to obtain a good estimate for the mean and the variance (if the noise may be assumed to be ergodic, i.e., the space-ensemble is equivalent to the time-ensemble). In each pixel (i,j) , the relation: $\text{var}\underline{y}(i,j)=\alpha.\mu_y(i,j)$ holds. In this situation, the individual estimates for μ_y and $\text{var}\underline{y}$ can only be based on two samples, which is not very reliable. A more accurate estimate is obtained by considering the ensemble of all pixels and calculating α as follows:

$$\alpha = \frac{\sum_{i,j} \text{var}\underline{y}(i,j)}{\sum_{i,j} \mu_y(i,j)} \quad (\text{A.17})$$

If the image is corrupted by multiplicative shading $c(i,j)$, the situation is slightly different; $\underline{y}'(i,j)=c(i,j).\underline{y}(i,j)$, thus $\mu_{y'}(i,j)=c(i,j).\mu_y(i,j)$ and $\text{var}\underline{y}'(i,j)=c^2(i,j).\text{var}\underline{y}(i,j)$. Rewriting these expressions gives:

$$\alpha = \frac{\sum_{i,j} \text{var}\underline{y}'(i,j)}{\sum_{i,j} c(i,j).\mu_{y'}(i,j)} \quad (\text{A.18})$$

Peculiarly, the shading corrupted images have to be corrupted once more to obtain the proportionality constant. Intuitively, this can be understood from the quadratic influence of the shading on the variance, while the mean is only affected linearly. If the two image instantiations are available and denoted by $I_1(i,j)$ and $I_2(i,j)$, for practical purposes, the last expression converts into:

$$\alpha = \frac{\sum_{i,j} [I_1(i,j)-I_2(i,j)]^2}{\sum_{i,j} c(i,j)[I_1(i,j)+I_2(i,j)]} \quad (\text{A.19})$$

Eq. (A.19) is valid, if the image variance originates from signal noise only and the mean is corrected for possible offset.

Chapter 6. Background correction

6.1 Curve fitting or parameter estimation

Fig. 6.1 illustrates the principle of model-based background correction. Two regions are discerned: the pre-edge Γ -region with a width w_Γ and a Δ -region with a width w_Δ . Both regions are sampled through a spectrometer slit with an energy-width w_s . The purpose of the background correction is to obtain the quantity I_k by subtracting the background I_b from the measured total intensity I in the Δ -region. The background is quantified by fitting a function to the samples obtained in the Γ -region, which is then extrapolated to the Δ -region. In spectroscopic images, the situation in Fig. 6.1 applies for each pixel location.

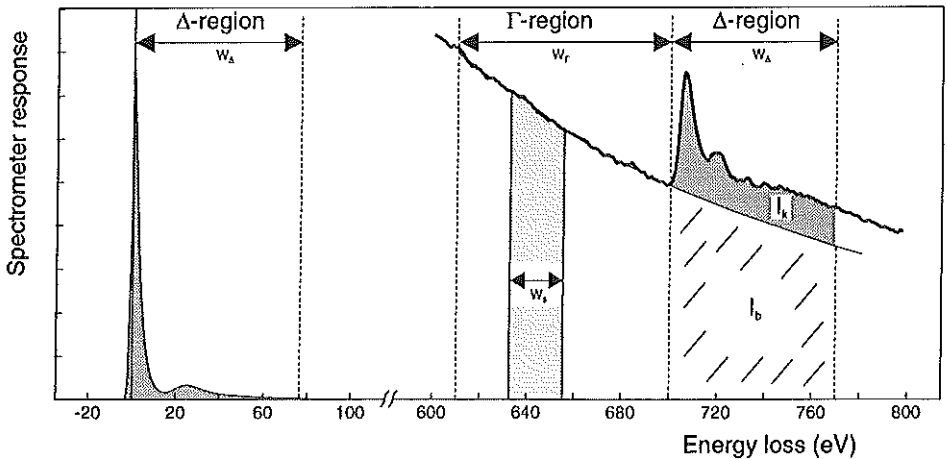


Figure 6.1 The problem of model-based background subtraction. The background I_b is to be removed to obtain the net-intensity I_k in the Δ -region. The Γ -region is used for fitting the model.

Since the advent of EELS, many techniques have been developed for the correction of the background contribution. As powerful computer resources were rare when researchers were first confronted with the problem of background correction, computational simplicity was the most important feature for the algorithms. Methods like the fitting of linear functions or weighted subtraction of a pre-edge image from an edge image have been applied [Sorber90b, Kortje92], leading to questionable results, as the physical nature of the images was neglected. In addition to these obviously too simple methods, more sophisticated techniques such as the three window method [Egerton80, Reimer91], Simplex fitting [Bruijn91] and log-log fitting [Pun84] were developed. Some authors were concerned about the limited validity of the

power-law and tried other functions in the low-loss region [Tenailleau92] or tried to account for the slight variation of the r -parameter with the energy-loss [Bonnet88a]. Although the power-law model (or one of its variants) was the basis for most methods mentioned above, the statistical nature of the problem was neglected or inadequately modelled. While great efforts have been made to develop the various curve-fitting techniques, only very few authors recognized this shortcoming. Colliex [Colliex81] realized that the EELS data as acquired with his microscope could best be described by Poisson distributions, but he was unable to translate the problem appropriately and resorted to weighted least-squares fitting based on the assumption of normal distributions. The Marquardt-algorithm [Bevington69] he used needs many iterations to find the optimal parameters in the banana-shaped error space. Also care has to be taken with the initial values, as convergence is not guaranteed in some cases. For Poisson distributed data obtained from counting detectors used in STEM instruments, Unser et al. [Unser87] were the first to derive the correct maximum likelihood estimators. In addition, they designed an efficient, rapidly converging iterative algorithm for finding the optimal estimates. The paper was apparently difficult to read as it lasted till 1994 [Botton94] before an implementation of the algorithm was reported. In section 5.2.3, we argued that the data obtained with the EM902 in the current set-up is unlikely to follow a Poisson distribution. Unfortunately, the results in [Unser87] are therefore not applicable. Nevertheless, following their ideas, in the next section it is shown that an equally efficient method can be derived for normally-distributed data, with non-constant variance.

6.2 An efficient algorithm for background fitting

6.2.1 Theory

Suppose we have n observations in the pre-edge part of the spectrum, denoted by the column vector \underline{w} ($w_1 \dots w_n$), obtained at energy-losses x ($x_1 \dots x_n$). Then the observation model in the pre-edge region is given by $\underline{w}_i = Ax_i^{-r} + \underline{v}_i$, with the noise term \underline{v}_i and is described by the transposed parameter vector: θ (A, r). From the assumed normal joint probability density $\underline{L} = f(\underline{w}; \theta)$, the following log-likelihood function can be derived:

$$\ln \underline{L} = -\frac{N}{2} \ln 2\pi - \ln[\det V]^{1/2} - \frac{1}{2} (\underline{w} - A\mathbf{x}^{-r})' \mathbf{V}^{-1} (\underline{w} - A\mathbf{x}^{-r}) \quad (6.1)$$

where \mathbf{V} is the covariance matrix of the noise. This diagonal matrix is composed of the variances σ_i^2 in each observation channel. To find the optimal parameter values, the function $\ln \underline{L}$ is maximized by equating the partial derivatives with respect to A and r to zero:

$$\begin{aligned} \sum_{i=1}^n \frac{w_i x_i^{-r}}{\sigma_i^2} - A \sum_{i=1}^n \frac{x_i^{-2r}}{\sigma_i^2} &= 0 \\ \sum_{i=1}^n \frac{w_i x_i^{-r} \ln x_i}{\sigma_i^2} - A \sum_{i=1}^n \frac{x_i^{-2r} \ln x_i}{\sigma_i^2} &= 0 \end{aligned} \quad (6.2)$$

Chapter 6

Parameter A as a function of r can be obtained explicitly:

$$A = \frac{\sum_{i=1}^n \frac{w_i x_i^{-r}}{\sigma_i^2}}{\sum_{i=1}^n \frac{x_i^{-2r}}{\sigma_i^2}} \quad (6.3)$$

while the following non-linear equation remains for r:

$$f(r) = \frac{\sum_{i=1}^n \frac{w_i x_i^{-r} \ln x_i}{\sigma_i^2}}{\sum_{i=1}^n \frac{w_i x_i^{-r}}{\sigma_i^2}} - \frac{\sum_{i=1}^n \frac{x_i^{-2r} \ln x_i}{\sigma_i^2}}{\sum_{i=1}^n \frac{x_i^{-2r}}{\sigma_i^2}} = 0 \quad (6.4)$$

The problem of maximum likelihood fitting is now transformed into the problem of finding the zero-crossing of the function $f(r)$. In other words, the dimensionality of the problem is reduced, while also the complexity has decreased because of the smooth behaviour of $f(r)$. The zero crossing of $f(r)$ may, e.g., be found by using the numeric method of Newton-Raphson, which utilizes iteration steps: $r_{k+1} = r_k - f(r)/f'(r)$, where $f'(r)$ is the first order derivative of $f(r)$. $f'(r)$ is given by:

$$f'(r) = \frac{-\sum_{i=1}^n \frac{y_i x_i^{-r} \ln^2 x_i}{\sigma_i^2} \cdot \sum_{i=1}^n \frac{y_i x_i^{-r}}{\sigma_i^2} + \left(\sum_{i=1}^n \frac{y_i x_i^{-r} \ln x_i}{\sigma_i^2}\right)^2}{\left(\sum_{i=1}^n \frac{y_i x_i^{-r}}{\sigma_i^2}\right)^2} + 2 \cdot \frac{\sum_{i=1}^n \frac{x_i^{-2r} \ln^2 x_i}{\sigma_i^2} \cdot \sum_{i=1}^n \frac{x_i^{-2r}}{\sigma_i^2} - \left(\sum_{i=1}^n \frac{x_i^{-2r} \ln x_i}{\sigma_i^2}\right)^2}{\left(\sum_{i=1}^n \frac{x_i^{-2r}}{\sigma_i^2}\right)^2} \quad (6.5)$$

A lower limit on the iteration step size $f(r)/f'(r)$ may be used as a stopping criterion. Iterating several times gives the requested r-value. The corresponding value for A is obtained by evaluating eq. (6.3). The variances in eqs. (6.4) and (6.5) are not exactly known and have to be estimated. This can be done either by repeatedly acquiring the same scene, which is very cumbersome, or by using the dependency of the variance on the expected value (eq. (5.3)). The latter approach has been followed here and μ_y is estimated each iteration from the best fit till then, as calculated in the previous iteration.

From the best estimate for the background parameters, the actual background at energies beyond the edge is calculated by extrapolation of the power-law function and calculating its contribution I_b to the measured edge intensity I for each pixel location. Correction for the background is simply expressed by:

$$I_k = I - I_b \quad (6.6)$$

As the observations are noisy, the estimated parameters A and r have a limited precision. In chapter 7, the influence of this noise corruption on I_b , I_k , the final concentration values and on element detection is considered in detail.

6.2.2 Implementation and results

Based upon the given expressions, the method was implemented in the C programming language on a state of the art Hewlett Packard 9000-735 workstation. The code of a routine for fitting an energy-loss spectrum is given in appendix A6. We evaluated the implementation on the basis of results obtained from simulated and real spectra and from a sequence of energy filtered images.

Four data sets of 100 noisy spectra each were generated artificially, simulating the observation of a power-law model spectrum (AE^r) with an electron detector (1 eV channel width). The distribution of the noise is normal with a variance equal to the mean of each observation. Sets #1 and #2 originate from energy-losses in the range 400-500 eV with $r=3$ and $r=5$, respectively, and in sets #3 and #4 energy-losses in the range 900-1000 eV are considered, also with $r=3$ and $r=5$. Each spectrum consists of 100 channels. The SNR in the first channel was 45 for sets #1 and #2 and 14 for sets #3 and #4. Thus, sets #3 and #4 are relatively more noisy. The performance of the above described new method is compared to that of a standard least squares ravine-search method (Marquardt algorithm [Bevington69]). Ravine-search stops when the relative decrease of the mean square error (MSE) drops below a certain threshold. The stop criterion for the new method is a lower limit on the iteration step size. For both methods, the level of the threshold is defined to be 10^{-8} . Note that, although the threshold values are equal, the stop criteria themselves are not equivalent and difficult to compare. As a consequence, somewhat different results may be expected. Ravine-search is initialized with a reasonable estimate for A and r , obtained from the two-area method [Egerton80]. The new method starts with an r -value obtained in a similar way.

Table 6.1 shows the results of the application of both algorithms on fitting-regions with width: $w_T=100$ eV and $w_T=50$ eV, just before an ionization edge at $E_{IE}=500$ eV for sets #1 and #2 and an edge at $E_{IE}=1000$ eV for sets #3 and #4. The results in Table 6.1 are average performance figures, computed over 100 runs per set: mean (μ) and standard deviation (σ) of the estimated r -values, the mean (μ_{MSE}) and standard deviation (σ_{MSE}) of the residual MSE, the average number of iterations per spectrum (N_{it}) and the average computation time per spectrum (t). It can be demonstrated that for both methods, the average estimation results for

Chapter 6

Table 6.1 Average performance of the new method compared to a ravine-search method.

Data		Ravine search						New method					
Set	w_Γ	μ_r	σ_r	μ_{MSE}	σ_{MSE}	N_{it}	t(ms)	μ_r	σ_r	μ_{MSE}	σ_{MSE}	N_{it}	t(ms)
1	100	3.0065	0.0464	1.0111	0.1401	9.6	18	2.9993	0.0433	1.0092	0.1396	4.0	11
1	50	3.0287	0.1488	1.0180	0.2131	59.0	26	2.9993	0.1423	1.0144	0.2117	4.3	11
2	100	5.0104	0.0486	0.9903	0.1581	6.4	15	4.9944	0.0422	0.9865	0.1574	4.1	12
2	50	5.0440	0.1652	1.0081	0.2183	46.1	23	5.0049	0.1560	1.0035	0.2157	4.4	11
3	100	3.0500	0.2806	1.3367	0.5788	96.2	63	3.0092	0.2690	1.3349	0.5792	4.9	11
3	50	3.1847	0.8388	1.3086	0.7559	605.6	176	3.0383	0.8808	1.3047	0.7535	5.2	10
4	100	5.0827	0.3036	1.2476	0.4747	86.5	61	5.0411	0.3009	1.2458	0.4745	4.9	11
4	50	5.1395	0.8980	1.2167	0.5702	469.7	143	5.0025	0.9083	1.2100	0.5703	5.3	10

r and MSE are consistent with 99% confidence. The estimates for the parameter r are also unbiased using 99% confidence limits, except for set #4 for $w_\Gamma=100$ eV, processed with ravine-search. Note that the number of iterations and consequently the computation times are considerably less for the newly proposed method. In addition to that, this method seems very insensitive to noise as can be concluded from the (virtual) constancy of t and N_{it} . Ravine-search needs more iterations to calculate a fit for $w_\Gamma=50$ eV as compared to $w_\Gamma=100$ eV for the same set. Since the first case only uses the second part of the 100 eV wide Γ -region, this case is relatively more noisy. The consequence of more noise is more iterations, which is also observed when the results for ravine-search of sets #1 and #2 are compared to those of sets #3 and #4. Variation of the value of the stop criterion for ravine-search in decades from 10^{-8} to 10^{-3} indicated that the number of iterations decreases gradually; between 10^{-4} and 10^{-3} this number is comparable to that of the new method (still with criterion 10^{-8}). This is naturally at the expense of a decreasing MSE performance.

In the new method, the zero crossing of $f(r)$ in eq. (6.4) is very well determined as can be seen from Fig. 6.2b, where $f(r)$ and its first derivative are shown for the real spectrum in Fig. 6.2a. From the smoothness of $f(r)$ it can be expected that the initial estimate for r has little influence on the outcome of the new method. The process of background fitting was repeated, applied to the same sets of simulated spectra, but now initializing our method with $r=6$ and once more with $r=0$. All individual fitting results show no significant differences when compared to each other.

Finally, to test the usefulness of the new method for elemental mapping, a real sequence of six energy filtered (pre-edge) images (512x512 pixels) was used for background fitting ($E=608, 623, 638, 653, 668, 683$ eV; slit width $w_s=15$ eV). For each image coordinate the background was estimated with the new method and with ravine-search. An average of 5.3

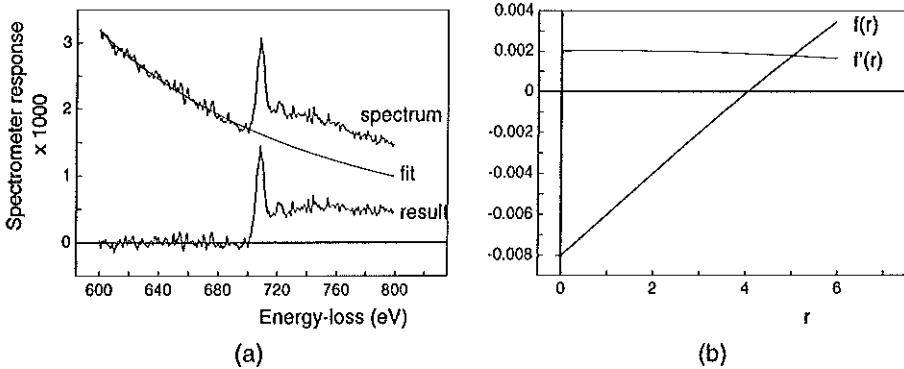


Figure 6.2 (a) Spectrum of an iron-containing section with background fit and subtraction result. (b) Function of the r -parameter and its derivative (eqs. (6.4) and (6.5)) for the pre-edge part of the spectrum in (a).

iterations per point was needed by the new method to calculate an r - and an A -image in 44.9 s. Using ravine-search on the same sequence, an average number of 88.0 iterations was needed. The computation time was 18 m 51 s. The fitting results were compared by calculating the sum of the MSE over all image points. The new method gave a residual MSE of 40759 and ravine-search yielded 40874. Here also, the new method is in favour for its higher speed and slightly lower MSE.

Chapter 6

APPENDIX A6 Listing of the spectrum fitting routine

```
#include <stdio.h>
#include <math.h>
#define EPS      0.00000001
#define MAXITER  25

FitSpectrum(E,F,N,r,A)
double  E[],F[];
int     N;
double  *r,*A;
{
    double  *logx,*log2x;
    double  u1, u2, u3, u4, u5, u6;
    double  yixir, xir, xi2r, lxi, l2xi, vari;
    double  FF, Fa, rr, dr;
    short   i, M;

    /* Allocate space for logarithm tables */
    logx = (double *)malloc(N * sizeof(double));
    if(logx == NULL) {
        printf("Cannot allocate logx table\n");
        return(-1);
    }
    log2x = (double *)malloc(N * sizeof(double));
    if(log2x == NULL) {
        printf("Cannot allocate log2x table\n");
        return(-1);
    }

    /* Initialize the log-tables */
    for(i=0; i<N; i++) {
        logx[i] = log(E[i]);
        log2x[i] = logx[i]*logx[i];
    }

    M = 0;
    dr = 1.0;
    rr = 0;
    while( (fabs(dr) > EPS) && (M<MAXITER) ) {
        u1 = u2 = u3 = u4 = u5 = u6 = 0.0;
        for(i=0; i<N; i++) {
            lxi = logx[i];
            l2xi = log2x[i];
            xir = pow(E[i],-rr);
            xi2r = xir*xir;
            yixir = F[i]*xir;
            vari = xir;

            u1 += yixir * lxi / vari;
            u2 += xi2r / vari;
            u3 += yixir / vari;
            u4 += xi2r * lxi / vari;
            u5 += yixir * l2xi / vari;
            u6 += xi2r * l2xi / vari;
        }
        FF = u1/u3 - u4/u2;
        Fa = (-u5*u3+u1*u1)/(u3*u3)-2.0*(-u6*u2+u4*u4)/(u2*u2);
        dr = FF / Fa;
        rr = rr - dr;
        M += 1;
    }
}
```

Background correction

```
/* On the basis of the estimated r-value, now calculate A */
u1 = u2 = 0.0;
for(i=0; i<N; i++) {
    xir = pow(E[i],-rr);
    vari = xir;
    u1 += F[i]*xir / vari;
    u2 += xir*xir / vari;
}
*r = rr;
*A = u1/u2;

free(logx);
free(log2x);

if(M==MAXITER)
    return(-1);
else
    return(0);
}
```

Chapter 7. Measurement issues

7.1 The precision of concentration measurements

7.1.1 Theory

An indication of the precision of the concentration measurements can be obtained from an estimation of the standard deviation σ_{N_x} . In the determination of the concentration with eqs. (3.3) and (3.5), the only quantity which may be expected to have an appreciable uncertainty is I_k , measured in the unknown. Therefore, the concentration variance amounts to:

$$\sigma_{N_x} = \frac{N_{x,s}}{R_{x,s}(k, \beta, \Delta) \cdot I_T(\beta, \Delta)} \cdot \sigma_{I_k} \quad (7.1)$$

where σ_{I_k} is the variance in the net edge-intensity. In a relative sense, the imprecision is expressed by:

$$\frac{\sigma_{N_x}}{N_x} = \frac{\sigma_{R_x}}{R_x} = \frac{\sigma_{I_k}}{I_k} \quad (7.2)$$

According to eq. (6.6), $\sigma_{I_k}^2$ is composed of the variances in the intensity of the observed edge and the background estimate:

$$\sigma_{I_k}^2 = \sigma_I^2 + \sigma_{I_b}^2 \quad (7.3)$$

Thus, to give an indication of the precision of the concentration measurements, estimates for the variances on the right hand side of eq. (7.3) have to be found. The first component in eq. (7.3) is obtained from the edge intensity itself with eq. (5.3), provided α and the shading influence $c(x,y)$ have been measured separately:

$$\sigma_I^2(x,y) = c(x,y) \cdot \alpha \cdot I(x,y) \quad (7.4)$$

The second component of eq. (7.3), $\sigma_{I_b}^2$, is generally larger in magnitude and also more difficult to obtain. Repeated acquisition of the pre-edge image sequence followed by background fitting may be possible but this is very cumbersome and requires much memory and computing power, since the procedures described in section 6.2 are to be performed several times. Therefore, this problem was approached differently. This is explained in the remainder of this section.

The theory of statistical parameter estimation offers the possibility of calculating the lowest obtainable values of the covariance of estimated parameters [Bos82]. Subsequent use of the uncertain parameters in a function of the parameters results in a variance of the function value. The consequence for the variance of using the uncertain parameters with

minimal covariance in such a function can be expressed by the so-called minimum variance bound (MVB). This MVB only depends on the estimation set-up and the probability density of the observations. For background correction, the estimation set-up comprises the independent variables, i.e. the energy-loss values at which the observations are made, the power-law model comprising the parameters A and r and also the use of this function for extrapolation. The MVB for background estimation is calculated hereafter.

Under the assumptions stated in section 6.2, the log-likelihood function $\ln \underline{L}$ was derived, see eq. (6.1). Following Van den Bos [Bos82], the information matrix M is defined by:

$$M = -E[\partial^2 \ln \underline{L} / \partial \theta^2] = \begin{bmatrix} \sum_i \frac{1}{\sigma_i^2} x_i^{-2r} & -\sum_i \frac{1}{\sigma_i^2} A x_i^{-2r} \ln x_i \\ -\sum_i \frac{1}{\sigma_i^2} A x_i^{-2r} \ln x_i & \sum_i \frac{1}{\sigma_i^2} A^2 x_i^{-2r} \ln^2 x_i \end{bmatrix} \quad (7.5)$$

The extrapolation of the background under the edge and the integration of these contributions is described as a function of the parameter vector $\rho(\theta) = \sum A x_k^{-r}$, where x_k represents the energy-loss of the edge-region channel k . For an unbiased estimator $r(\underline{w})$ of function $\rho(\theta)$, the Cramer and Rao inequality [Bos82] states for this case that:

$$\text{var} r(\underline{w}) \geq [\partial \rho(\theta) / \partial \theta] M^{-1} [\partial \rho(\theta) / \partial \theta]^T \quad (7.6)$$

where the right hand side expresses the lower bound on the variance that can be obtained when estimating the background under the edge with any unbiased estimator. $\text{Var} r(\underline{w})$ is in fact $\sigma_{I_b}^2$. With $\delta \rho(\theta) / \delta \theta = (\sum x_k^{-r}, -\sum A x_k^{-r} \ln x_k)$ and with eq. (7.5) substituted in eq. (7.6), the inequality rewrites to:

$$\sigma_{I_b}^2 \geq \frac{(\sum_k x_k^{-r})^2 \sum_i \frac{1}{\sigma_i^2} x_i^{-2r} \ln^2 x_i - 2 \sum_k x_k^{-r} \sum_k x_k^{-r} \ln x_k \sum_i \frac{1}{\sigma_i^2} x_i^{-2r} \ln x_i + (\sum_k x_k^{-r} \ln x_k)^2 \sum_i \frac{1}{\sigma_i^2} x_i^{-2r}}{\sum_i \frac{1}{\sigma_i^2} x_i^{-2r} \sum_i \frac{1}{\sigma_i^2} x_i^{-2r} \ln^2 x_i - (\sum_i \frac{1}{\sigma_i^2} x_i^{-2r} \ln x_i)^2}$$

(7.7)

Note that this equation is independent of the observations and only depends on the parameter values, the independent values for the energy-loss in the pre-edge region (with index i) and those in the edge region (with index k) and the distribution parameters σ_i^2 describing the pre-edge statistics. For an increasing number of observations (asymptotic behaviour) maximum likelihood estimators finally reach the MVB. The right-hand side of eq. (7.7) will further be

Chapter 7

abbreviated as V_{I_b} , thus $\sigma_{I_b}^2 \geq V_{I_b}$. In practice, there are two problems in evaluating V_{I_b} for each pixel location: the true local r -value as well as the local variance per channel are unknown. The first problem can be solved, by substitution of the estimated r -values instead of the true ones. The second problem is solved by the application of eq. (5.3) again to estimate the variance:

$$\sigma_{I_i}^2(x,y) = c(x,y) \cdot \alpha \cdot A(x,y) \cdot x_i^{-r(x,y)} \quad (7.8)$$

By taking the fitted background for the pre-edge intensity, we obtain a smoother estimate for $\sigma_{I_i}^2$ than when the actual observations were used. Now that we are able to evaluate $V_{I_b}(x,y)$ in practice, it may be used as an estimate for $\sigma_{I_b}^2(x,y)$. By substitution of $V_{I_b}(x,y)$ and eq. (7.4) in eq. (7.3), the total variance in the net edge intensity is:

$$\sigma_{I_i}^2(x,y) = c(x,y) \cdot \alpha \cdot I(x,y) + V_{I_b}(x,y) \quad (7.9)$$

This expression enables the evaluation of eqs. (7.1) and (7.2). The estimate V_{I_b} for $\sigma_{I_b}^2$ is biased, because it is only a lower bound on the variance. To get an impression of the error, this topic is investigated experimentally in the next section.

7.1.2 An experimental investigation of the approximation of $\sigma_{I_b}^2$ by V_{I_b}

The consequence of using V_{I_b} as an approximation of the true background variance was first examined with simulations (section 5.1). For two noise levels, spectra consisting of 8 energy-loss values in the range of 600-740 eV with a 20 eV step increase were generated with power-law parameter $r = 4.0$. Noise level I represents a signal to noise ratio (SNR) of 30 in the first channel at 600 eV and level II denotes an SNR of 10 in the same channel. For both noise levels, the spectra were generated repeatedly 100,000 times. The first 5 channels (600-680 eV) in each noisy spectrum were taken for estimation of the background, which was subsequently extrapolated to the remaining 3 channels (700-740 eV). In Table 7.1, the background variance 'Bg', directly obtained from the spectra, is given. For each spectrum, the background fit was calculated and extrapolated as indicated above. From the background values thus obtained, the variance was also computed. These values are indicated in Table 7.1

Table 7.1. Results of simulation experiments to test the validity of using the MVB for the true background variance. The column 'Bg' denotes the actual variance present in the spectrum, ' $\sigma_{I_b}^2$ ' refers to those values obtained after fitting and extrapolation, ' $V_{I_b}^{(1)}$ ' and ' $V_{I_b}^{(2)}$ ' indicate the values obtained from eq. (7.7), based on the actual and estimated MVB.

Noise level	Bg	$\sigma_{I_b}^2$	$V_{I_b}^{(1)}$	$V_{I_b}^{(2)}$
I	1745.7	8737.4	8711.7	8731.7
II	174.6	901.2	871.1	900.1

by σ_b^{2s} . Comparison of the columns 'Bg' and σ_b^{2s} reveals that, due to the extrapolation, in this configuration the variance was amplified approximately five times. Given the estimation set-up and noise levels, with eq. (7.7) and $r = 4.0$ the MVB-value $V_b^{(1)}$ is calculated, indicated in Table 7.1 as $V_b^{(1)}$. In practice the background r -value is not known, so if in eq. (7.7) the estimated r -values are used, the column $V_b^{(2)}$ is obtained. Comparison of the variance values shows that $V_b^{(2)}$ approximates σ_b^{2s} well. Estimation of the MVB from the fitting parameters seems to give somewhat higher values for the variance than when the true r -value is used. For the relatively lower noise level I this difference is less.

In a second experiment, measurements of the background variance were performed in a real spectroscopic image sequence obtained from a homogeneous section of epon. This series consists of eight images at energy-losses 608, 628, 648, 668, 688, 708, 728 and 748 eV. In this energy-loss range, no element specific edges are present for this specimen. After correction of the data for camera γ and shading, following the procedure in section 4.1.3, 16536 distributionally equivalent pixels were used in the analysis. The background was fitted using the five images with energy-losses below 708 eV and extrapolated to the remaining three. It was found that $\sigma_b^2 = 3.39$. With eq. (7.7) and the estimated r -parameters we found $V_b = 2.65$. The difference between the corresponding standard deviation values is 11.6%, somewhat higher than for the simulations. Similar experiments were repeated under various conditions and the differences in standard deviation typically varied between 10% and 20%. As the background variance is the most important component in the calculation of the precision in the elemental concentration, this latter precision would also be underestimated by 10-20% in these cases.

7.2 Strategies for concentration analysis

7.2.1 The calculation of signal to noise ratio images and their use for thresholding

The elemental concentrations represented in the distribution images are noisy quantities. To analyze these images, regions have to be defined in which the element contributions are significant. For the detection of elements in one-dimensional EEL spectra, it is a common procedure to first determine the signal to noise ratio of the net-intensity I_k , defined by:

$$S_{I_k} = \frac{I_k}{\sigma_{I_k}} \tag{7.10}$$

and to use this quantity in some way for thresholding (see, e.g., in [Puymbroeck92]). This step is frequently omitted in the case of electron spectroscopic images, where the I_k -image is directly used for thresholding [Sorber90b]. This is principally wrong, since the probability distribution in each pixel of the net-intensity image can be different. By normalizing the net-intensity image on the local standard deviation, as is done in calculating the SNR, and by thresholding this normalized image, the probability of making detection errors is equal for all pixels.

Chapter 7

The determination of the SNR-image $S_{I_k}(x,y)$ entails the difficulty of determining $\sigma_{I_k}(x,y)$. This problem, however, was solved in section 7.1.1, see eq. (7.9). From that section we also know that σ_{I_k} is underestimated and consequently with eq. (7.10), $S_{I_k}(x,y)$ is rated too high. Using $S_{I_k}(x,y)$ in a detection scheme yields more spurious detections than warranted. To reduce this effect, $S_{I_k}(x,y)$ can be corrected as follows. $S_{I_k}(x,y)$ is first calculated as described and a histogram is created from this image. In the absence of element contributions, the histogram shows a peak around zero and is expected to have a standard normal distribution [Pun84]. If an amount of element is present, the shape of the histogram is different because higher SNR-values are observed. The only part of which the shape is still similar is that below zero, representing half of the non-element distribution. The positive side of this distribution cannot be observed alone as it is deformed by the presence of low concentrations. When the standard deviation σ_{SNR} of the zero-centered peak is calculated from the negative portion, generally too high values, i.e. $\sigma_{SNR} > 1.0$, are obtained, as was expected from the overestimation of $S_{I_k}(x,y)$. By the scaling: $S'_{I_k}(x,y) = S_{I_k}(x,y) / \sigma_{SNR}$, the effect of overestimation is corrected and $S'_{I_k}(x,y)$ can further be used for element detection by thresholding.

Since I_k is corrupted by noise and only estimated parameters can be used for the evaluation of eq. (7.10), $S'_{I_k}(x,y)$ is somewhat noisy. This noise may be suppressed by spatially filtering S'_{I_k} . For the detection of objects consisting of several pixels, a certain amount of noise is not a real problem, as long as a sufficient number of object (element) pixels are positively detected.

7.2.2 Additional and alternative strategies for analysis

To reduce the influence of the noise during the concentration analysis in general, image filtering may be applied. Usually such a step is at the expense of the spatial resolution and it depends on the application whether this is acceptable or not. Image filtering may be applied in three ways. The first is to smooth the entire input image data before analysis (pre-processing). A second alternative is to filter the computed background image, because the background subtraction stage introduces most of the noise (intermediate processing). Finally, the concentration distribution images, or the SNR-images in the case of element detection, may be filtered (post-processing). The usefulness of spatial filtering techniques was studied to some extent in [Bonnet88a]. Post-processing can also be applied to the binary element map to re-group rejected object pixels and to remove spurious detections. Such operations, however, require more knowledge (size, shape, etc.) about the analyzed objects. This issue leads to a more general discussion about object-based detection [Pun84], in contrast to the pixel based detection scheme exploited in the previous section.

Spectroscopic image sequences usually contain more information, because images are also acquired in the zero- and low-loss region and at $E=250$ eV. Both the zero-loss and the $E=250$ eV energy filtered images show fine detail of biological structures making them in principle suited for the detection of various organelle structures such as mitochondria, parts of the endoplasmatic reticulum, golgi complex, lysosomes, etc. These images can be processed

alone, but also in combination to arrive at more robust schemes for biological object detection. When object models can be defined on a sufficiently abstract level, they can be quite useful for the analysis of images. Some care is demanded since the boundaries of element regions do not necessarily have to coincide with biological objects such as organelles. An example of the use of a simple model is described in section 11.2 for the detection of ferritin particles.

From images acquired in the zero- and low-loss region, the relative section thickness is calculated using eq (3.7). This result is primarily intended to check the validity of the application of the quantification expressions and can be used to discriminate regions that violate thickness requirements in order to exclude these from further analysis [Botton94]. More generally, a relative thickness image could also be used for segmentation.

An entirely different approach to concentration analysis is the user-driven definition of measurement regions. Such an approach circumvents the computationally expensive treatment of the entire image sequence by restricting the analysis only to user-defined regions. It is applicable when the user has a clear interpretation of what is depicted in the image and wants to quantify some aspect in the image in a goal-directed way. For this purpose a program was devised, allowing a user to move a scalable spot over a structure image (e.g. $E=250$ eV), controlled by a computer mouse. From the corresponding spectroscopic sequence, in the area thus defined, the spectrum is reconstructed and the concentration is determined in reference to the standard, which was processed in advance. If the regions are not too large, this procedure is fast enough to be executed on-line. As the spot size increases, more data are integrated in the spectrum and the SNR improves. Fig. 7.1 shows the program running on a workstation. Variants of such a program have also been developed elsewhere [Kortje94, Lavergne94].

7.3 Opportunities for the validation of the image data

The processing and analysis of spectroscopic image sequences is based on several assumptions, such as the absence of radiation damage and drift, the validity of the power-law model and appropriate specimen thickness. While methodological assumptions may be verified in general, acquisition dependent and specimen dependent aspects are to be evaluated each time. It is worthwhile to identify the checks which can be routinely performed, without imposing special requirements on an acquisition protocol. Four important aspects are considered: specimen drift, radiation damage, the consistency of the data in general with respect to both the assumed model and the instrumental stability of the entire acquisition system, and finally, the section thickness.

Specimen drift

Specimen drift is most prominent just after starting the irradiation of a section. If, during the execution of an image acquisition protocol, the same energy-filtered image is digitized again after some interval of time, in the absence of drift and disregarding noise, the pixel-wise difference of the two images should reveal a zero result. Structures seen in this image imply the presence of drift, which necessitates restoration steps as described in section 4.2.

Chapter 7

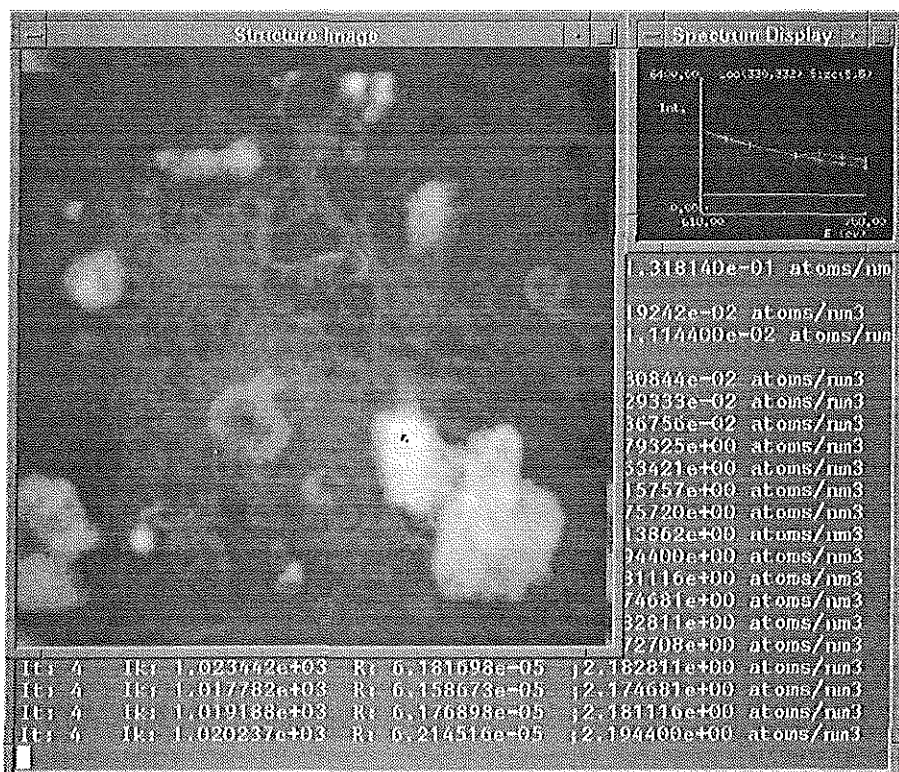


Figure 7.1 The interactive program for analysis of a sequence of spectroscopic images. One window shows a structure image, used for locating the analysis spot with the mouse. A second window graphically shows the spectrum reconstructed from the selected region and simultaneously the background fit. When a measurement value from an internal standard is available, the element concentration is given numerically in the text window.

Mass-loss

Mass-loss from radiation damage changes the spectrum because inelastic scattering is reduced in general. As a result, the intensity in the core-loss part of the spectrum decreases. The general pattern of radiation damage is a rapid loss during the first few seconds from the start of the irradiation, followed by a plateau phase with virtually no loss and lasting for several minutes. After that, further damage is inflicted [Lamvik87-91]. Using two time-spaced recordings as, e.g., used for the drift assessment, the average greyvalue of the two images should be equal in the absence of damage. If not, this could indicate specimen damage. Also, the inspection of the integrated spectrum over all pixel locations (with a sufficiently good

SNR) can reveal possible damage as discontinuities in the spectrum, provided sufficient spectral images are available.

Consistency of the data

Colliex [Colliex81] mentions the possibility of evaluating the chi-square measure after the fitting procedure to test the goodness-of-fit of the power-law function to the data. Tests based on this measure are considered particularly of use if edges are close together and the structure in the profile of one edge corrupts the background fitting region of another.

A particularly powerful way of checking the data is to apply the procedure for background correction and element detection on a data set known to contain no element contribution. If a sufficient number of pre-edge images is available, this could be done without any additional acquisition effort by considering the subset of pre-edge images only, pretending that the last pre-edge image is the "edge"-image and applying the background correction and detection procedures to that image [Bonnet88a]. The validity of using the MVB for the calculation of the SNR- I_k images for element detection is tested implicitly in this way, because the number of spurious detections can be determined and compared to the expected number.

If some knowledge about parts of the specimen is available, the absence of certain elements in particular areas can be predicted. In pixels where no element is present, the greylevel after background correction should be zero on average. This property can be used to check for any bias in the background correction procedure.

Specimen thickness

For increasing values of the relative section thickness, eq. (3.2) yields too low values for the concentration [Stephens80]. The relative section thickness is easily monitored by evaluation of eq. (3.7), which requires a spectroscopic sequence to be acquired in the low-loss region to cover the first 100 eV. If, e.g., the region from 0-50 eV is already needed for quantification, some additional images are to be acquired to cover the whole 0-100 eV region.

Chapter 8 further describes the consequences of the incorporation of validity checks as mentioned in this section for the acquisition of the entire image set and for the analysis procedure.

7.4 Measurement linearity

The purpose of this section is to investigate issues related to the linearity of the measurement of N_x . Eq. (3.4) states that R_x is proportional to N_x , suggesting that the investigation of linearity can be performed by addressing R_x only. The main difference between N_x and R_x , as can be seen in eq. (3.4), is a factor containing the specimen thickness. The partial cross-section is a constant. This means that R_x is proportional to the area concentration rather than to the volume concentration. This has no negative consequences for the evaluation of linearity. Linearity can be studied by creating known modulations in the

Chapter 7

measured quantity. Since R_x is proportional to the number of atoms per unit area, modulations can be created in two ways. In one approach, the volume concentration is varied. This issue is addressed in section 7.4.1. The other approach is to vary the area related concentration by modulation of the section thickness. This is described in section 7.4.3. The influence of variations in the relative section thickness on the linearity of R_x is treated in section 7.4.2. The consistency of the relative thickness as a measured quantity is investigated section 7.4.4.

7.4.1 The investigation of linearity with double sections of Fe-Chelex

Specimens with known modulations in volume concentration are not available. It was therefore tried to produce such a standard by creating unfiled grids with double sections in which iron-loaded Chelex spheres were present. In those locations where two spheres overlap the relative element concentrations are known, see Fig. 7.2. If from the spheres A and B (using eq. (3.3)) the average values ${}^A R_{Fe}$ and ${}^B R_{Fe}$ are obtained, respectively, the two should add-up to the quantity ${}^C R_{Fe}$ as measured in the overlap region C. Three data-sets, obtained from specimens with overlapping spheres in four locations were acquired with the protocol summarized in section 8.2, and subsequently analyzed. Fig. 7.3 shows I_k - and R_{Fe} -images of a complex situation in which three spheres overlap and thus in one image, two useful

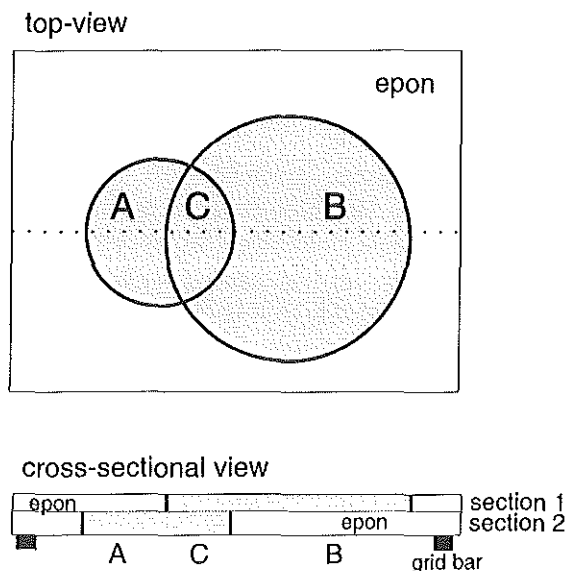


Figure 7.2 Sketch of the situation in a specimen with double sections. Region A is composed of a Chelex sphere in one section and epon in the other. This is similar the case for B. Region C is the region of overlap of A and B.

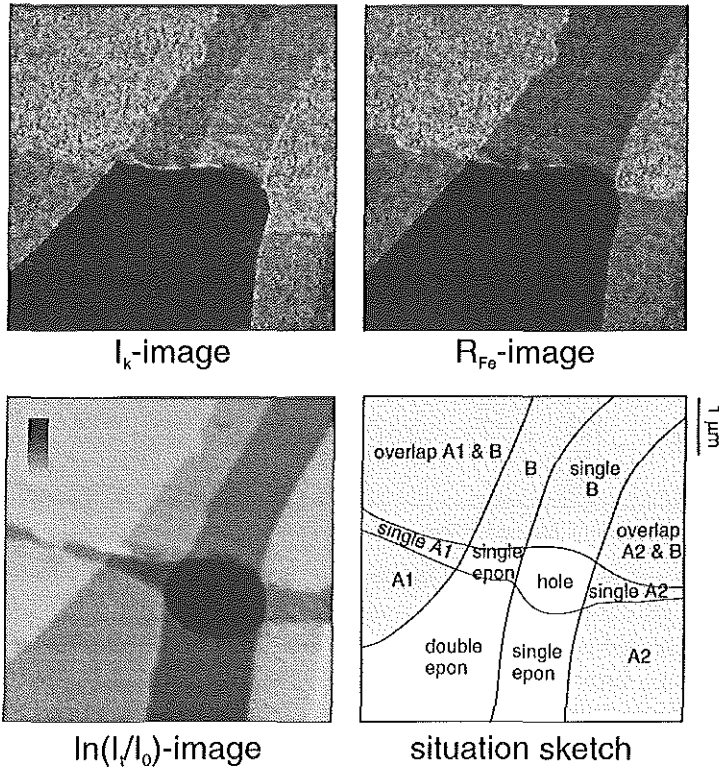


Figure 7.3 I_k -, R - and $\ln(I_t/I_0)$ -images of a double section containing three Fe-Chelex spheres. The sketch visualizes the situation. Both sections are torn, which permits the observation of the single spheres.

measurement situations are generated in the sense described. In the calculated R -images, for each of the regions A, B and C, multiple 63×63 pixel non-overlapping subregions were considered. The average R -value within each subregion was computed and if more than one subregion was available, the standard deviation was also calculated. Table 7.2 shows the results. From this table it is seen that the values for ${}^C R_{Fe}$ are systematically too low when compared to the expected values, and although the noise was reduced, considerable variations are still present. Several phenomena account for these results. First of all, the sectioning of the epon embedding medium in which the Chelex spheres are contained is difficult. Not only do many spheres drop out or get wrinkled, also chatter (periodic thickening and thinning) occurs during sectioning, generally resulting in thickness differences. Secondly, in this experiment, the inelastic mean free paths of epon and Fe-Chelex are different, creating regions

Chapter 7

Table 7.2. Measurement results obtained from double sections with Fe-Chelex. Spheres A and B are measured separately and together in the overlap region C. The latter results are to be compared to the values that are expected from the sum of the results in the single sphere regions. All measurements are obtained from fixed 63x63 image subregions to suppress the noise to a low level. If more than one such a subregion fitted within a Fe-Chelex region, the standard deviation was also calculated.

${}^A R_{Fe} (10^{-6})$		${}^B R_{Fe} (10^{-6})$		${}^C R_{Fe} (10^{-6})$		${}^A R_{Fe} + {}^B R_{Fe} (10^{-6})$
μ	σ	μ	σ	μ	σ	
37.9	2.1	35.6	-	56.5	6.1	73.5
35.7	1.3	31.1	1.1	55.9	5.0	66.8
37.1	-	32.2*	-	53.8	3.4	69.3
34.7	2.4	32.2*	-	56.6	2.6	66.9

*Both values were obtained from the same region.

A, B and C with different values for λ . Stephens [Stephens80] found that for increasing values of t/λ , increasingly too low values for R result from application of eq. (3.2). Our results are consistent with this behaviour. Thirdly, the distribution of the element loaded onto the Chelex is known to be not entirely uniform over a sphere, resulting in gradual variations in the R-values. When the measurements were repeated in subregions with locations which may be considered equivalent with respect to a suspected iron-loading gradient, the values for ${}^C R_{Fe}$ and ${}^A R_{Fe} + {}^B R_{Fe}$ were closer together: 65.6 vs. 71.1, 62.0 vs. 65.6, 59.4 vs. 69.4 and 56.5 vs. 69.1. In section 7.4.2 it is tried to put the effects of variations in thickness and mean free path into perspective. Fe-loading of Chelex is investigated in section 7.4.5.

In general, it must be concluded that with R depending on t/λ , the measurement scale is non-linear as the latter quantity always varies over a section. The severity of this non-linearity will be smaller if the section is thinner. The double sections used in this experiment have relative thickness values that lie outside the range usually met in practice. It should also be realized that in the measurement set-up described in this thesis, we use a standard for concentration reference having a comparable λ -value and the same section thickness as biological material. When unknown and standard are similarly biased, calibration with the standard will cancel (part of) this bias.

7.4.2 The relation between R_{Fe} and $\ln(I/I_0)$ in sections with Fe-Chelex

Observing the situation in the double sections with overlapping Fe-Chelex spheres, there are variations in iron-quantity, composition (λ) and, due to section artifacts such as tears, also differences in thickness (t). It was therefore tried to investigate all these effects simultaneously and to visualize them with $R_{Fe}-\ln(I/I_0)$ plots as a representation for R_{Fe} vs. t/λ , both obtained

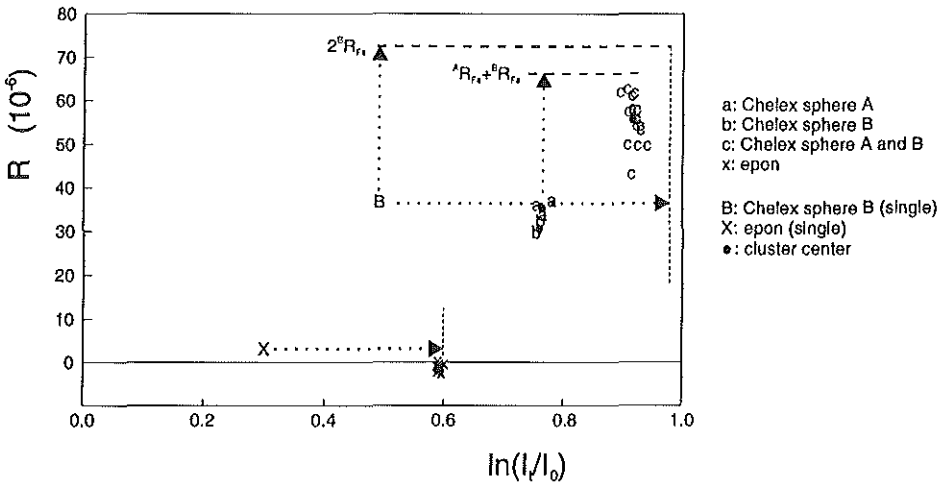


Figure 7.4 R - $\ln(I_v/I_0)$ plot of measurements in a section like in Fig. 7.2. Because one of the sections was torn, one of the individual sections could also be observed.

from the same locations. Fig. 7.3 shows an example of an R_{Fe} -image with the corresponding $\ln(I_v/I_0)$ -image. A typical R_{Fe} - $\ln(I_v/I_0)$ plot is shown in Fig. 7.4 for one of the data sets used in the previous section. For the double section part, 63×63 pixel subregions measured in spheres A and B, their overlap C and epon are indicated by 'a', 'b', 'c' and 'x', respectively. Measurements in locations where single parts of the sections were visible are marked by 'B' and 'X', as indications for sphere B and epon, respectively. The average value of each cluster is depicted with a '•'. Also, four levels are indicated. The two levels for R represent the expected value ${}^A R_{Fe} + {}^B R_{Fe}$ and the R -value if double B-spheres would be present. For the latter case we used the R -value of the single section under the assumption of linearity in R to estimate the corresponding R -value: $2^B R_{Fe}$. The consideration of this hypothetical case of double B-spheres is justified by the belief that both sections have equal thickness. Similarly, two levels for $\ln(I_v/I_0)$ are drawn, based on the measurement of a single section and the assumption of linearity in t . One level is for epon and the other for (assumed) double Fe-Chelex B-spheres. Apart from the negatively deviating value for R_{Fe} for larger t/λ -values, $\ln(I_v/I_0)$ is also estimated somewhat too low in epon and estimated definitely too low in Fe-Chelex. This follows from the discrepancy between the calculated levels and actual values obtained from the double regions. Fig. 7.4 also indicates that, especially in the double Fe-Chelex part, a considerable variation in R_{Fe} exists, while there is no positive correlation between R_{Fe} and t/λ . Similar plots obtained from comparable image sets of single and double Fe-Chelex sections revealed the same pattern, leading to the conclusion that the variations in R_{Fe} are to be explained mainly by inhomogeneous iron loading of the Fe-Chelex and not by thickness variations.

Chapter 7

7.4.3 The investigation of linearity with $R_{Fe}-\ln(I/I_0)$ plots from sections with Fe-Chelex

In section 7.4.1, linearity was investigated by comparing measurements within an R_{Fe} -image. Fig. 7.5 gives another view on the linearity of measurement. This figure is an $R_{Fe}-\ln(I/I_0)$ plot obtained from various image sets of Fe-Chelex containing sections, both single and double. Each individual point (*) was obtained from a 63x63 pixel region and the average value per Chelex sphere is also indicated (o). Similarly obtained values from epon regions are given as a baseline reference ('+'). In one section, there was a hole. Measurements in this region are marked by an 'x'. The average values per sphere were used to draw a curve, suggesting the functional dependence between R_{Fe} and t/λ . The flattening of the curve illustrates the non-linearity of the measurement scale. The degree of non-linearity, however, seems to be minor for values of $\ln(I/I_0) < 0.6$. The baseline, composed of the 'epon' and 'hole' measurements, is positively biased and slightly tilted. The reason for this is not known. The observations in the hole also suggest a positive bias in the relative thickness measurement which is expected to be zero for this location.

7.4.4 The consistency of $\ln(I/I_0)$ measurements

To check the consistency of $\ln(I/I_0)$ measurements in general, for each available Fe-Chelex data set, in the same $\ln(I/I_0)$ -image, the values obtained in Chelex were compared to those measured in epon. Fig. 7.6 shows the result. Linear regression reveals a good correlation ($R=0.99$) and coefficients 0.74 (angle) and -0.065 (intercept). The intercept value deviates

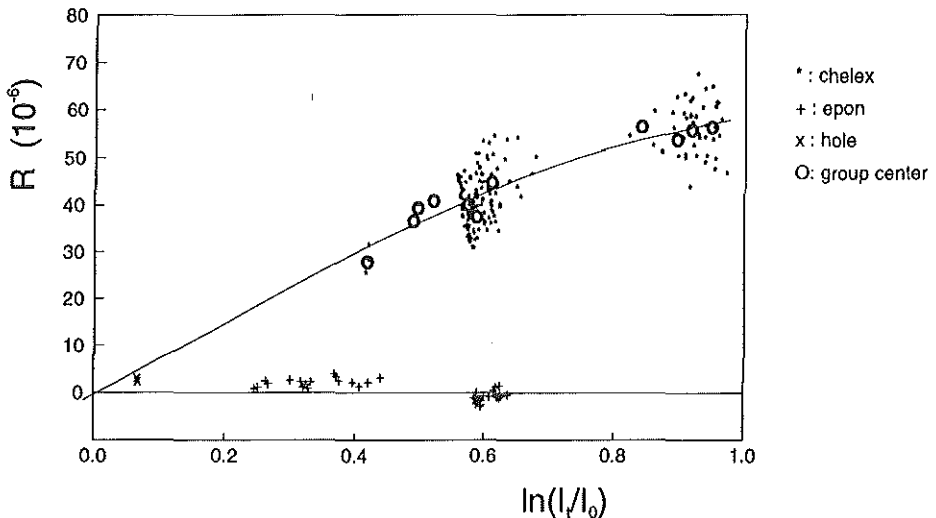


Figure 7.5 $R-\ln(I/I_0)$ plot of measurements in single and double sections. The average value per Chelex sphere is indicated and a curve is suggested for the relationship between R and $\ln(I/I_0)$.

somewhat from the expected value of zero. This is probably caused by the underestimation of t/λ for increasing values of the actual relative section thickness, as was already observed in Fig. 7.4. As the relative thickness in Fe-Chelex is generally larger than in epon, the underestimation problem is also larger for the Fe-Chelex and the regression line tends to be too steep. The effect may be partially suppressed by forcing the regression line through zero. This results in an angle coefficient of 0.65 while the correlation is still high ($R=0.98$). The angle of the regression line represents the relation between the inelastic λ -values of epon and Fe-Chelex: $\lambda_{\text{Chelex}}=0.65\lambda_{\text{epon}}$.

7.4.5 Variations in the loading of Fe-Chelex spheres

The loading of a chemical element into the Chelex shows variations. Not only may the loading within a sphere be inhomogeneous, also differences between spheres may be present. Measurements in sectioned Fe-Chelex spheres revealed a coefficient of variation (cv) of 10-20% for the variability of the concentration [Bruijn85a, Cleton86]. In Pt-Chelex even higher values were reported [Bruijn85b]. Another study [Zhengzhu93] established considerably lower values (cv: 2%-8%) for Pb-, Cd-, and Al-Chelex.

With the available data sets of Fe-Chelex, the variability within spheres was evaluated by computing the coefficient of variation of R_{Fe} and $\ln(I_t/I_0)$ in several regions. Each region was subdivided into a number (N) of 63×63 pixel subregions. Table 7.3 shows the result. In epon regions the variability of $\ln(I_t/I_0)$ -measurements was obtained similarly and shown in Table 7.4. The variability of the element loading measured here is somewhat smaller than in

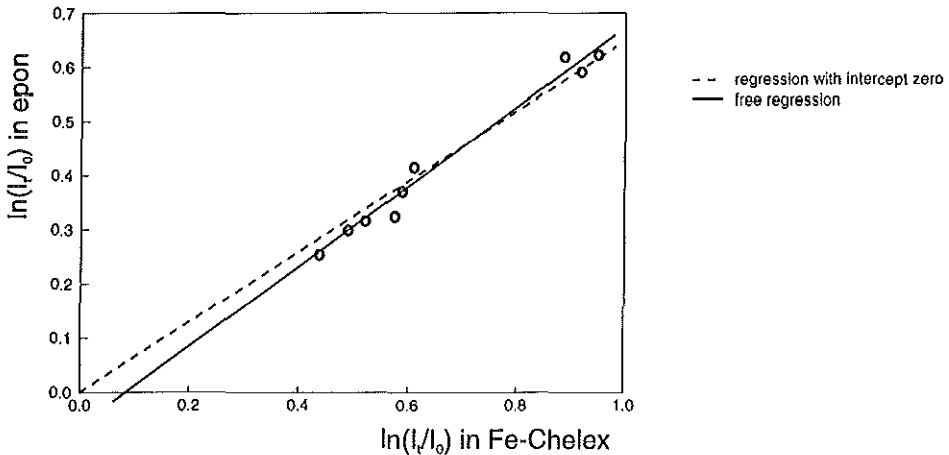


Figure 7.6 Comparison of the $\ln(I_t/I_0)$ -values in Fe-Chelex and epon regions in the same section.

Chapter 7

Table 7.3 The variability of R_{Fe} and $\ln(I/I_0)$ measured in single sections of Fe-Chelex. The size of the analyzed area in each specimen is expressed by the number of subregions N .

cv R %	cv $\ln(I/I_0)$ %	N
10.7	2.7	41
9.7	2.3	39
12.3	4.1	37
9.0	1.1	18
10.8	1.2	17
6.3	2.1	10
5.6	1.1	5
3.6	0.5	3
3.8	1.4	3
8.7	0.4	3
4.6	2.3	2
6.9	1.2	2

Table 7.4 The variability of $\ln(I/I_0)$ measurements within epon. The extent of the analyzed region is expressed by the number of subregions N .

cv $\ln(I/I_0)$ %	N
0.7	13
1.4	6
0.4	5
1.4	4
3.3	4
3.9	4
0.8	3
0.8	2

[Bruijn85, Cleton86], but of the same order of magnitude. This is probably due to the limited size of the considered areas. The largest spatial range over which the variability in the Chelex was analyzed was approximately 4.4 μm . The analyzed area was always on the border of a sphere. The average radius of a Chelex particle is 25 μm , thus only small parts have been analyzed. The variability of the $\ln(I_i/I_0)$ -measurements in Chelex and in epon is also smaller than the variability in R in this experiment.

7.5 The reproducibility of measurements

The reproducibility when repeating the entire measurement procedure was only briefly investigated. Experiments were performed twice under similar conditions. One of the double Fe-Chelex containing sections was acquired twice at the same location. The only difference was a slight rotation between the two views. In a second case, a single Fe-Chelex sphere was recorded twice. The locations within the sphere were different, but both acquisition areas were positioned along the border of the sphere. If there is an element loading gradient it is believed to be radially directed. Thus, measurements from the same radial position should be comparable. Measurements were done in Fe-Chelex and epon. The upper four rows of Table 7.5 contain the results for the double sections. The lower two rows are for the single section. Comparison of the measurements reveals that the relative errors for R are larger than those for $\ln(I_i/I_0)$. The relatively high value for the error in the last epon result is probably caused by contamination of the section and is considered to be an outlier. The average errors with respect to the reproducibility of concentration measurements and of $\ln(I_i/I_0)$ are 6.7% and 4.0% respectively.

Table 7.5 Overview of measurement results in the same double section with Fe-Chelex at the same location and in a single section within the same Chelex sphere in comparable but different locations. The results are compared on the basis of their relative error. The fourth and sixth row are obtained from epon.

Instance 1		Instance 2		Comparison		Location
R (10^{-6})	$\ln(I_i/I_0)$	R (10^{-6})	$\ln(I_i/I_0)$	$\epsilon(R)$ (%)	$\epsilon[\ln(I_i/I_0)]$ (%)	
37.9	0.796	36.2	0.773	4.6	2.9	double
32.2	0.794	29.4	0.763	9.1	4.0	double
65.6	0.945	62.0	0.911	5.6	3.7	double
-1.1	0.623	-0.7	0.589	-	5.6	epon
40.3	0.585	43.4	0.563	7.4	3.8	single
4.0	0.370	2.2	0.325	-	12.9	epon

Chapter 8. Image acquisition and analysis of Fe in biological specimens

8.1 Design considerations of an image acquisition protocol

An image acquisition protocol defines the sequence of actions to be performed to obtain a series of energy-filtered images. A variety of aspects is important when an image acquisition protocol is to be designed that provides all the information necessary for quantification. Not only the type of information is important, but also the quality of the information. Choices made in the acquisition stage influence the final quantitative results and determine the research questions which can be answered using these results. The most important aspects for the design of an acquisition protocol will be summarized hereafter. Similar considerations hold for the Bio-standard, which is used as a substitute for the cross-section combined with the section thickness. Practically, image acquisition for Fe quantification with the $L_{2,3}$ -edge is addressed.

Γ -region

The Γ -region (Fig. 6.1) is used for estimation of the spectral background. For the model-based approach, which involves extrapolation, this region should be located as close to the edge as possible. The energy-range w_{Γ} covered by the Γ -region has to be chosen such that no fine structure of edges with a smaller ionization energy is present. Also, the slight dependency of the r -parameter in the power-law function in eq. (5.1) on the energy-loss creates a limitation of the range. On the other hand, there should be a balance between the sizes of the Γ - and Δ -regions, because the background extrapolation to the latter region amplifies the noise. The Γ -range is generally chosen not smaller than the Δ -range.

Iron is usually present in specimens in an oxidized state and oxygen is also present in many bio-molecules. The oxygen K-edge lies at 532 eV just before the Fe $L_{2,3}$ -edge at 708 eV. Starting the Γ -region at around 600 eV circumvents distortions from the O K-edge and creates a sufficiently large fitting region with $w_{\Gamma} \approx 100$ eV. This choice limits the size of the Δ -region to about 100 eV.

Δ -region

The Δ -region (Fig. 6.1) is used for estimation of the element specific contributions. Measurement in this region should provide an accurate element related quantity with minimal noise. The start of the Δ -region is always located at the onset of the edge. The ionization edge profile varies from element to element and large fluctuations may be present. Such near-edge effects alone are not representative for the amount of the element. In order to restrict these influences, the width of the Δ -region, w_{Δ} , must be sufficiently large. It must, however, not be too large because the noise is amplified by the extrapolation process. On the other hand, the accuracy of eq. (3.2) for quantification decreases if w_{Δ} is smaller. The size of the Δ -region is usually determined in balance with the size of the Γ -region.

Image acquisition and analysis of Fe in biological specimens

Experiments with different Δ -regions have shown that near edge fluctuations in the iron edge profile are sufficiently damped if $w_{\Delta} > 50$ eV. If $w_{\Gamma} = 100$ eV, this limits the choice for the Δ -range to: $50 < w_{\Delta} < 100$ eV.

Δ_2 -region

The Δ_2 -region is used for the estimation of the relative section thickness. The width of this region must be as large as practically possible. For thin sections, however, the cut-off energy is frequently taken to be at 100 eV, above which the spectral intensity is usually considered negligible.

Objective-lens aperture

The objective-lens aperture (β) of the microscope restricts the solid angle of transmitted electrons. In an absolute sense it controls the number of scattered electrons to be used for image formation and thus the image intensity. In a relative sense it regulates the elastic and inelastic contributions to the image and also influences the contributions of various types of inelastic scattering. Outer-shell interactions generally result in somewhat larger scattering angles than core-loss interactions. Thus, a limitation of β enhances image contrast in zero-loss filtered images and spectral contrast in the core-loss region. The objective-lens aperture also influences the image quality in a spatial sense, because the two most prominent resolution limiting effects (chromatic- and spherical aberration) depend on β (section 2.4.1). Table 2.1 suggests that for an optimal resolution, β has to be relatively small.

For the investigation of biological materials, radiation damage was considered to be of prime importance. Therefore, the largest available aperture of $\beta = 17$ mrad was chosen for maximum signal yield, thus minimizing the exposure time.

Slit width

The slit allows electrons from an energy-band to be projected as an energy-filtered image. The wider the slit, the brighter the image, but also the larger the chromatic aberration. In the case of a more or less uniform energy-distribution, the projected brightness and aberration-disc size depend linearly on the slit width w_s . The electron dose can be lower if the slit is more opened, because the brightness of an image is higher and fewer samples are needed to cover selected Γ - and Δ -regions.

For iron structures of considerable size, the chromatic aberration is of secondary importance. Choosing $w_s = 20$ eV and $w_{\Gamma} = 100$ eV, the Γ -region can be covered with 5 samples starting at 608 eV and the Δ -region with minimally 3 samples ($w_{\Delta} = 60$ eV), starting at 708 eV.

Magnification, resolution and field of view

The choice of the magnification is determined by three aspects: projected image intensity, the limitation of the spectrometer entrance aperture by the spectrometer slit [Bihr88] and image resolution in relation to the vertical sample frequency (section 2.4.1). The projected intensity

Chapter 8

is higher for lower magnifications and depends quadratically on the magnification. Loss of intensity by an increase of magnification is usually compensated by an increase of the electron dose.

Given the size of the objective-lens aperture in combination with a certain slit width, Bihr [Bihr88] defines a lower limit on the magnification to have the objective aperture as the only limiting aperture for the entrance of the spectrometer. For $w_s=20$ eV and $\beta=17$ mrad the magnification limit is 5.000x.

The size of the total aberration disc (see eqs. (2.3-2.7)) is determined by the instrumental parameters β , w_s and the location of the edge of interest. For the case of measuring iron, Table 2.1 gives a total aberration of 4.0 nm for the chosen parameters. The Nyquist criterion requires a sample distance of 2.0 nm for the vertical image direction, for which a magnification of 20,000x (2.5 nm pixel distance) would be necessary. For several reasons, a slightly lower magnification was chosen: 12,000x, corresponding to a sample size of 5.5 nm. The first reason is that the resolution values in Table 2.1 are theoretical values; practical values are generally worse, e.g., because of non-optimal (manual) focusing or specimen drift. The Fourier transform of an iron containing test image, acquired with 12,000x magnification at $E=708$ eV did not reveal any signs of aliasing. The second reason for using this magnification is that it gives an approximately four times higher projected image brightness and a larger field of view: 2.8 μm along each side of a 512x512 image. For the embedded element standard, spatial details are not important. Therefore, the first available magnification above 5,000x may be taken. In the instrument used, this is a magnification of 7,000x.

Illumination brightness

Given a specimen, a spectral region to be investigated, instrumental parameters such as β , w_s and a fixed the magnification, the only remaining aspect that determines the intensity of a projected energy-filtered image is the brightness produced by the illumination system. Radiation damage is proportional to the electron flux through the specimen and must be kept as small as possible.

In practice, the camera is set at a high gain-level and the illumination brightness is adjusted to the lowest possible level still having (visually) a homogeneous spatial distribution.

Brightness dynamics

The acquisition of images in the core-loss as well as in the zero- and low-loss regions on a calibrated scale brings along the problem of bridging large brightness differences with the camera. The camera signal is digitized in 8 bits, while about 20 bits are needed to cover the entire dynamic range. With the calibrated attenuation filters in front of the camera (Fig 2.4) the amount of light reaching the sensor may be adequately reduced, avoiding the need to change the microscope illumination system, or to adapt the camera gain setting [Bruijn93].

For the acquisition of the energy-loss region around the iron edge from 608 eV until 768 eV with a slit of 20 eV, no filter is needed. Before switching to the zero-loss region, a

Image acquisition and analysis of Fe in biological specimens

filter with an optical density $D=4.0$ is inserted. Since in the zero- and low-loss region large intensity differences are still present, a second filter with $D=3.0$ was used to allow the acquisition of the low-loss region.

Camera properties

The camera properties are to be measured under the same conditions as those used for the specimen acquisition. Additional images with known relative intensity are needed for shading- and γ -correction. A black reference image can always be obtained by covering the sensor. Camera-related noise can be measured, provided a second black image is available. This is done similarly to the measurement of the signal noise as described at the end of section A5.3.

Under the iron acquisition conditions, for shading reference an empty microscope field at zero-loss is obtained with the filter with $D=4.0$. For the γ -value to be determined, the empty field is acquired once more with a filter of $D=4.3$.

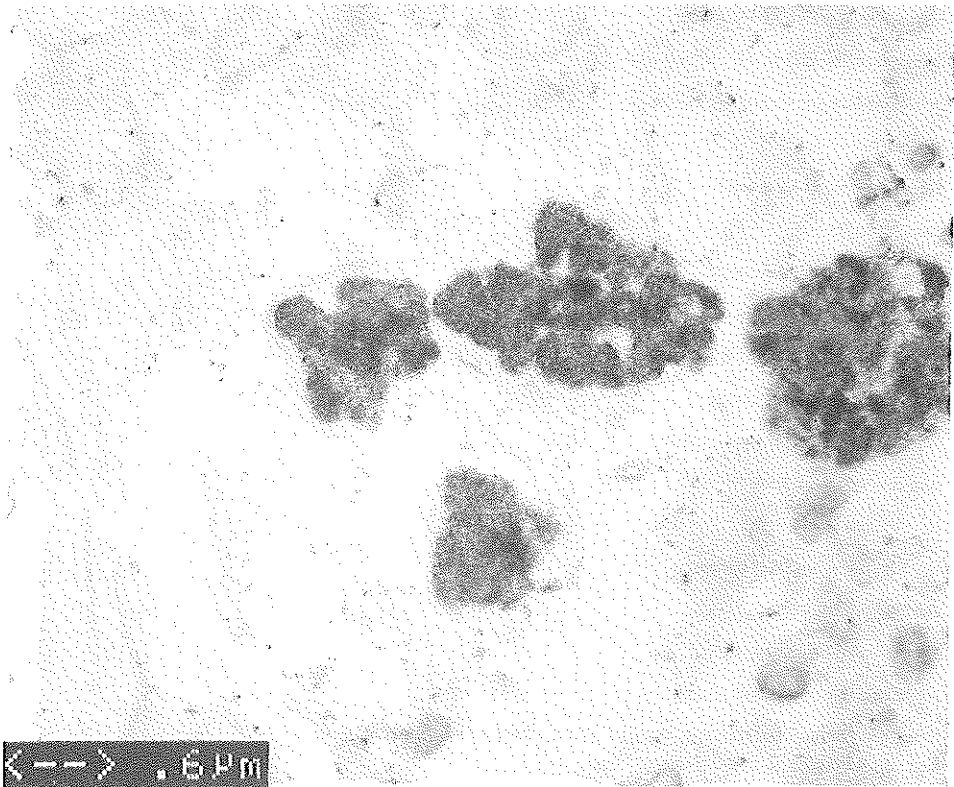


Figure 8.1 Conventional electron micrograph of the field of interest.

Chapter 8

Table 8.1. Acquisition protocol for iron.

Action	Result image
Select E=608 eV	
Fix illumination and freeze camera gain	
Acquire E=608 eV image	I ₁
Re-acquire E=608 eV image	I ₂
Select/Acquire E=628 eV image	I ₃
Select/Acquire E=648 eV image	I ₄
Select/Acquire E=668 eV image	I ₅
Select/Acquire E=688 eV image	I ₆
Select/Acquire E=708 eV image	I ₇
Select/Acquire E=728 eV image	I ₈
Select/Acquire E=748 eV image	I ₉
Select/Re-acquire E=608 eV image	I ₁₀
Insert filter D = 4.0	
Select/Acquire 0 eV image	I ₁₁
Insert filter D = 3.0	
Select/Acquire 20 eV image	I ₁₂
Select/Acquire 40 eV image	I ₁₃
Select/Acquire 60 eV image	I ₁₄
Select/Acquire 80 eV image	I ₁₅
Select empty region; cover sensor	
Acquire two dark images	I ₁₆ , I ₁₇
Insert filter D = 4.0	
Set E = 0 eV; uncover sensor	
Acquire white image	I ₁₈
Insert filter D = 4.3	
Acquire attenuated white image	I ₁₉
Re-adjust camera, illumination, remove filters, re-locate stage to specimen and select/acquire E=250 eV image	I ₂₀

Image acquisition and analysis of Fe in biological specimens

Table 8.2. Overview of the analysis procedures.

Processing action	Processing result	Equations
Calculate γ from I_{16} , I_{18} , I_{19}	γ	eq. (4.4)
Calculate shading from I_{16} , I_{18} with γ	$c(x,y)$	Norm $[(I_{18}-I_{16})^{1/\gamma}]$ (section 4.1.3)
Calculate α from I_1 , I_2 , I_{16} with γ and $c(x,y)$	α	eqs. (5.4) and (A.19)
Fit power-law from I_2 to I_6 using I_{16} , and with γ	$r(x,y)$, $A(x,y)$	section 6.2
Extrapolate background with $r(x,y)$ and $A(x,y)$	$I_b(x,y)$	section 6.2
Integrate edge intensity from I_7 to I_9 , using I_{16} , and with γ	$I(x,y)$	
Correct background with $I(x,y)$ and $I_b(x,y)$	$I_k(x,y)$ (Fig. 8.3)	$I_k = I - I_b$ (section 6.2)
Calculate background variance with α , $c(x,y)$, $r(x,y)$, $A(x,y)$	$\sigma_b^2(x,y)$	eqs. (7.7) and (7.8)
Calculate SNR of I_k with $I_k(x,y)$, $\sigma_b^2(x,y)$, α , $c(x,y)$, $I(x,y)$	$S_k(x,y)$	eq. (7.10)
Determine histogram of $S_k(x,y)$	His(S_k)	section 7.2.1
Calculate σ_{SNR} from zero-centered peak in His(S_k)	σ_{SNR}	section 7.2.1
Correct $S_k(x,y)$ for over-estimation	$S'_k(x,y)$ (Fig. 8.4)	$S'_k = S_k / \sigma_{SNR}$
Detect objects by thresholding the SNR at 3 with $S'_k(x,y)$	Map(x,y) (Fig. 8.4)	$S'_k > \text{threshold}$
Integrate zero/low-loss contribution from I_{11} to I_{13} , using I_{16} , with γ and filter densities 4.0 and 3.0	$I_T(x,y)$	
Calculate R-image with $I_k(x,y)$ and $I_T(x,y)$	$R_k(x,y)$ (Fig. 8.3)	eq. (3.3)
*Calculate concentration with $R_k(x,y)$, $R_{cs}(x,y)$, $N_{cs}(x,y)$	$N_k(x,y)$ (Fig. 8.5)	eq. (3.5)
*Calculate std. dev. of local concentration	$\sigma_{N_k}(x,y)$	eq. (7.1)
Integrate zero/low-loss contribution from I_{11} to I_{15} , using I_{16} , with γ and filter densities 4.0 and 3.0	$I_l(x,y)$	
Obtain zero-loss image from I_{11} , using I_{16} , with γ and filter density 4.0	$I_0(x,y)$	
Calculate relative section thickness with $I_k(x,y)$ and $I_0(x,y)$	$T(x,y)$ (Fig. 8.3)	$T = \ln(I/I_0)$

Chapter 8

Integration time per image

The integration time is regulated by the real-time digital addition of images. A longer integration time results in less noise, but also in larger possible drift effects. For practical purposes, the most convenient number of images used for integration was 256.

Validity checks

The validity checks for which an additional acquisition effort is needed are drift and radiation damage assessment and the monitoring of the relative section thickness. For drift and damage, the most convenient way to obtain an extra, delayed image is to re-record the first acquired core-loss region image in the protocol at the end. For the relative thickness, see the issue of the Δ_2 -region.

Noise measurement

For the determination of the proportionality factor α between greyvalue mean and variance with eq. (5.4), mean and variance measurements under stationary conditions are necessary. According to eq. (A5.19), two instantiations of an image are sufficient for this purpose. The brightest image in the pre-edge region is considered to be the most convenient image.

For iron, with a protocol based on $w_s=20$ eV and $w_r=100$ eV, the 608 eV image is the brightest pre-edge image. This image is therefore acquired twice.

Image acquisition strategy

The order in which images are acquired is dictated by two factors. No re-positioning of the specimen stage is allowed, because the reproducibility is insufficient and the thermal conditions need time to stabilize. Thus, all specimen related images must be acquired in one run and the empty field images are to be obtained separately. Furthermore, changing filters means dead time which is to be avoided. The camera must not be adjusted during the acquisition of an image series.

8.2 Description of the image acquisition protocol for Fe

Before acquisition of any iron related image sequence, the microscope is aligned and adjusted according to the instructions [Zeiss]. In the illumination system a condenser diaphragm with a hole of 400 μm is used. A 90 μm diaphragm is inserted below the objective lens to obtain an aperture of 17 mrad. The slit in the spectrometer is adjusted to 20 eV width and for offset calibration of the energy-loss scale, a negative bias of a few eV's is set as a guard region. The TV-camera needs a warming-up period of at least 45 minutes [Tsay90]. Interesting specimen locations and Chelex positions can be stored and recalled from memory in the stage-drive control unit. The magnification is set at 12,000x if the specimen is to be obtained and switched to 7,000x for the Chelex.

By taking into account the various considerations as discussed in the previous section, a protocol was designed as given in Table 8.1. The actions are briefly described and the

Image acquisition and analysis of Fe in biological specimens

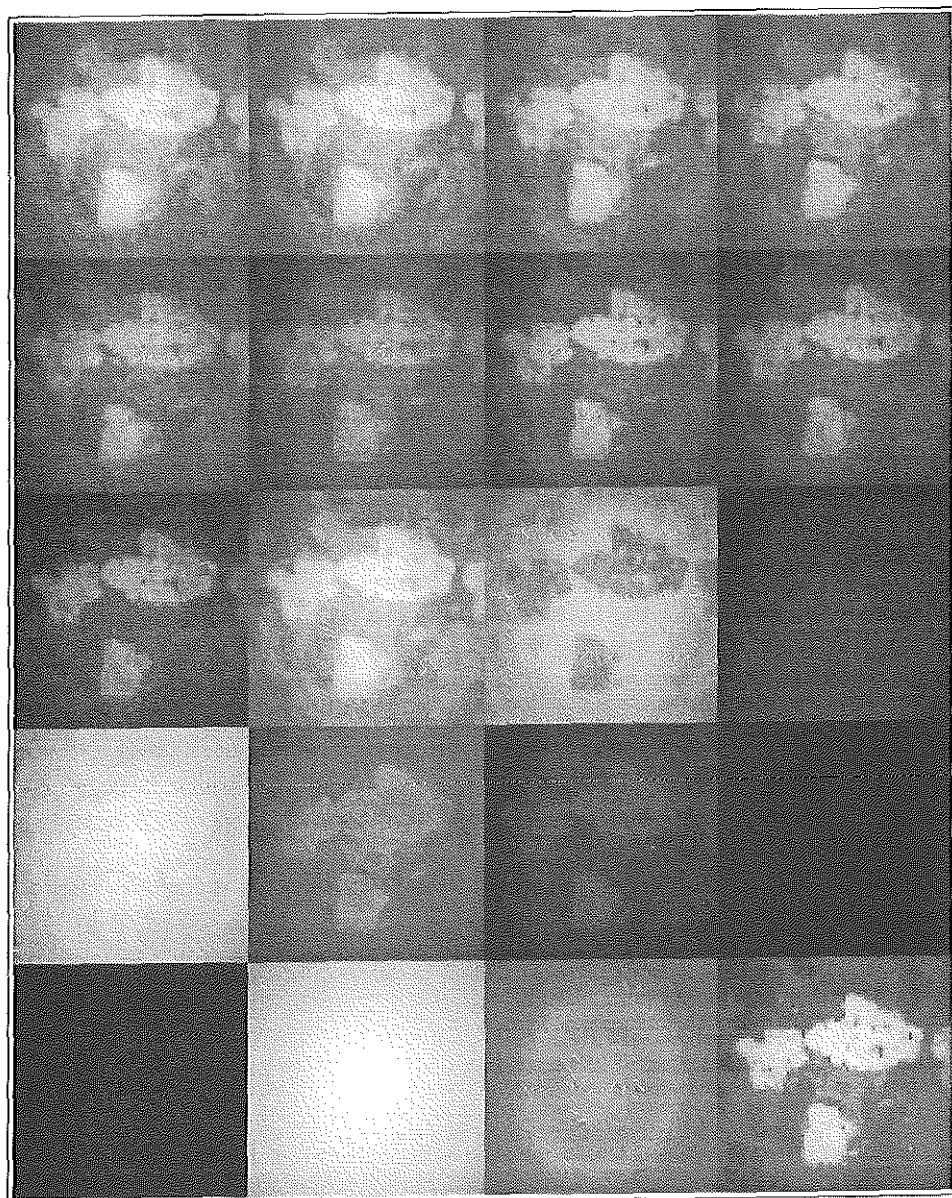


Figure 8.2 A composition of images, acquired with the protocol in Table 8.1.

Chapter 8

resulting images are identified. To acquire a 250 eV image for reference to the biological structure, the camera and illumination system has to be re-adjusted, because the number of available filters is limited. This is done afterwards, while in a more ideal situation this would be done, e.g., after acquiring the low-loss sequence. In this chapter we will illustrate the result of acquisition and various processing steps with an example. Fig. 8.1 shows an overview of the field of interest, Fig. 8.2 shows a composition of images acquired with the protocol defined above. The images I_1 - I_{20} are ordered scanwise. The liver section from which the images are obtained is described in chapter 12 (situation A).

8.3 The analysis procedure for Fe

Before the actual analysis procedure is executed, the integrated values of the images I_2 and I_{10} in Table 8.1 are computed to assess possible damage to the specimen. The difference image $I_2 - I_{10}$ is inspected for the presence of structures, which would indicate specimen drift. If it is shifted, the whole image sequence is processed to find the corresponding drift vectors, either by cross-correlation or by hand (see section 4.2). In the sequel, it is assumed that the correction for specimen drift is applied when appropriate. This step will not further be mentioned explicitly.

The various parts of the analysis procedure as introduced in this thesis are summarized in Table 8.2. This table describes the calculations that are performed, the images involved and the equations that are applied. The identification of the input images is the same as in Table 8.1. In contrast to the parameters (α, γ, \dots), the image results have an explicit reference to their (x, y) coordinates. The entire procedure is first applied to the Chelex Bio-standard present in the same ultrathin section of the specimen to obtain a value for $R_{x,s}$ (omitting the $'$ -steps) and then to any other sequence of the same specimen section, which is then calibrated with the $R_{x,s}$ -value obtained. The most powerful validity check described in section 7.3 is that for non-detection. For that purpose, the procedure in Table 8.2 is followed too, until the detection of the element contributions. In this case, the images I_2 to I_5 are taken as pre-edge images and I_6 as the pretended edge image.

Several steps in the analysis procedure are illustrated in Figs. 8.3 and 8.4. Fig. 8.5 shows the final quantitative iron distribution image with the corresponding indication of the local relative measurement error (scale indicator 0-50%). The check for non-detection yielded 204 randomly distributed pixels detected.

Image acquisition and analysis of Fe in biological specimens

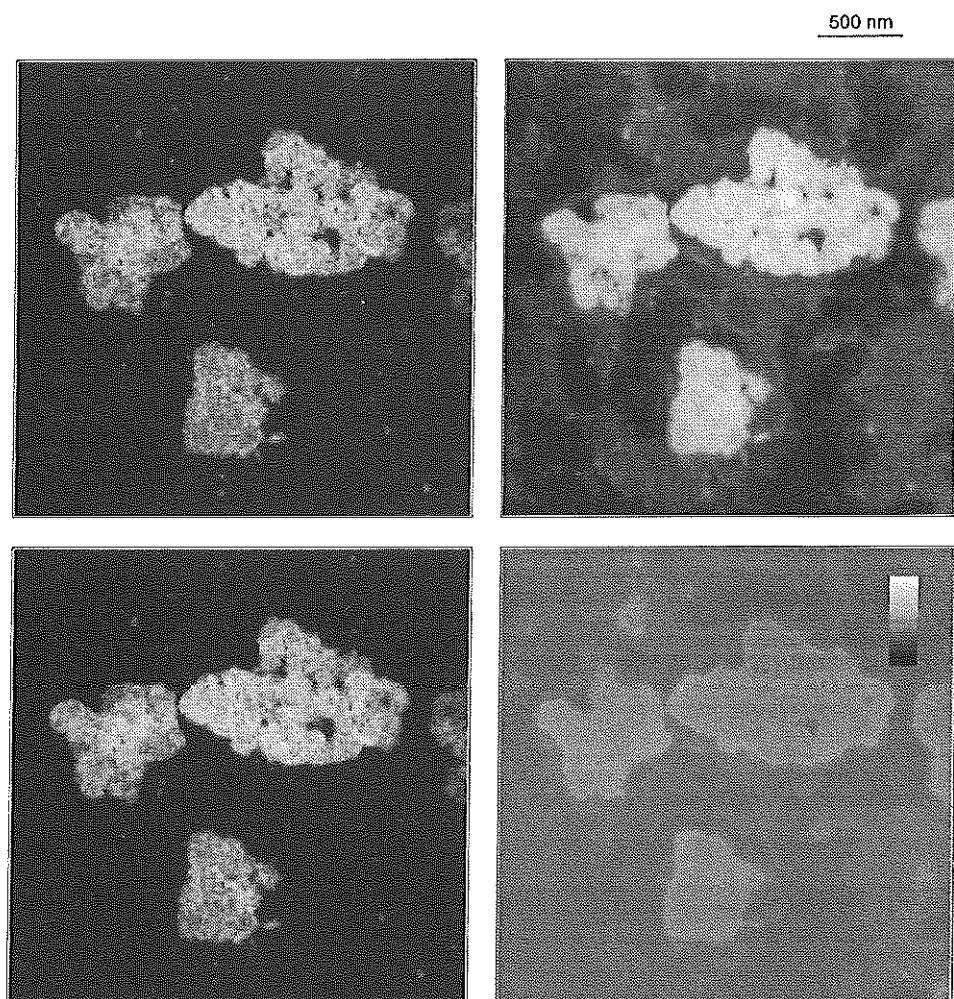


Figure 8.3 Results of the analysis procedure applied to the images in Fig. 8.2: I_c -image (top left), R-image (bottom left), T-image (bottom right) with grey bar from 0.0-1.0. The structure image ($E=250$ eV) is shown top right.

Chapter 8

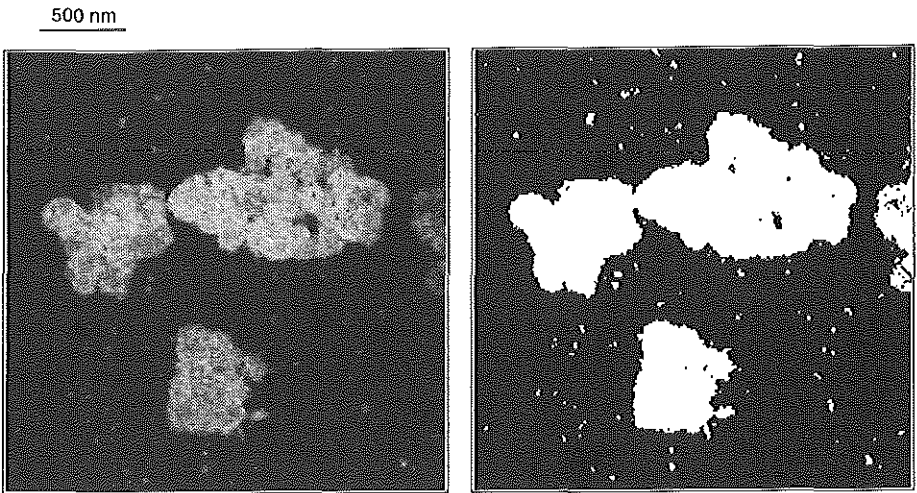
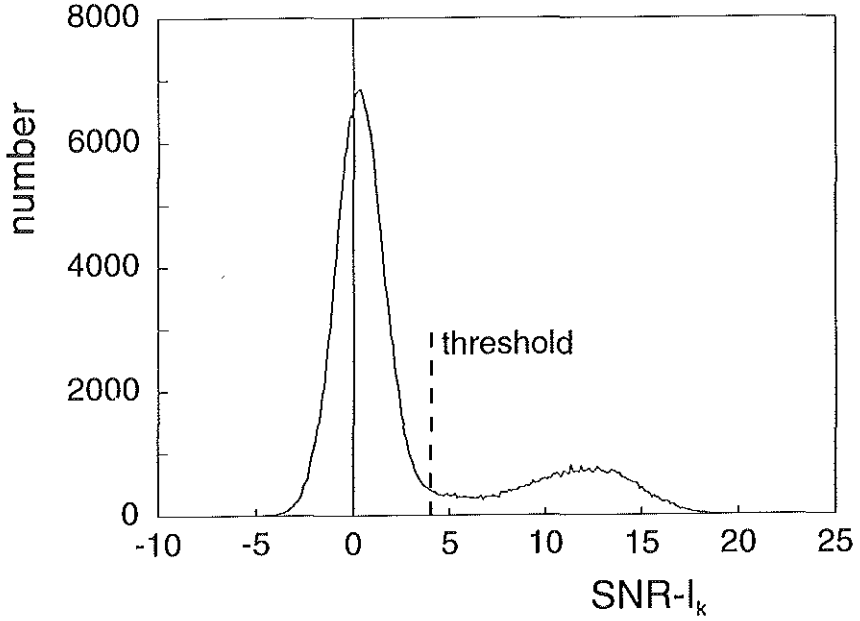


Figure 8.4 The process of element detection. The histogram (top) of the SNR-image (bottom left) is shown. The element map after thresholding at a calculated level of 3.7 is shown bottom right.

Image acquisition and analysis of Fe in biological specimens

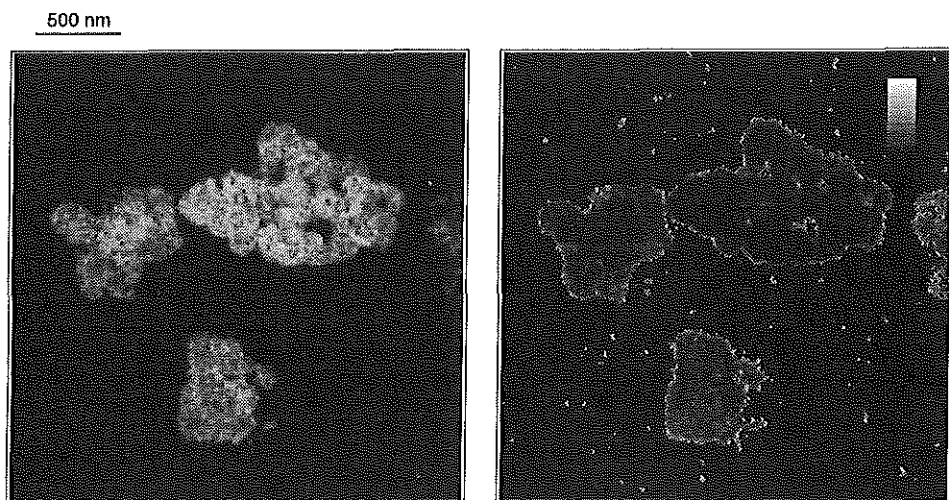


Figure 8.5 Final result of the procedure: the quantitative iron distribution image, masked with the detection map, together with an indication of the relative precision (scale bar 0-50%).

Chapter 9. Discussion part I

The first part of this thesis describes the development of methods to perform quantitative elemental concentration measurements in ultrathin sections of biological specimens. An acquisition protocol was devised which assures that all images necessary for quantification are obtained. In addition, procedures for processing the image sequences were developed. The main results of the analysis procedure are expressed in a number of images: the requested concentration distribution image, a corresponding binary image mask that identifies the location of significant element contributions (the elemental map), an image which contains an estimate of the local measurement precision and an image reflecting the local relative section thickness. Calibration of the concentration measurement values was performed by using a co-embedded Bio-standard. Chapters 2 - 7 give a detailed description of the motivation and assembly of the individual steps leading to well-documented quantification procedures. At this point it seems worthwhile to put some achievements into perspective in a critical review. A general conclusion is postponed until chapter 12.

The principle of quantification

The approach to quantification followed in this thesis is "classical" in the sense that the standard quantification expression eq. (3.2) is used and that background subtraction is performed based on the power-law model eq. (5.1). In all situations in which the power-law applies, and only in those situations, are the techniques generally valid. In other cases, e.g., for edges in the low-loss region (such as S, P...) or in the vicinity of other edges (such as Ca in the presence of C), the currently developed methods yield unreliable results. Furthermore, the step of background extrapolation amplifies the noise, which masks low elemental concentrations from detection. New techniques to cope with these problems are under development. These can possibly be used as alternatives for the currently used techniques, in situations where the power-law cannot reliably be applied.

Hannequin et al. [Hannequin88] initiated the use of the formalism of correspondence analysis as such an alternative for power-law based background subtraction. Because initially only qualitative element distributions could be obtained [Trebbia90a&b], improvements of the procedures were proposed for the quantitative use of the formalism [Bonnet92a&b, Gelsema92&94]. These methods are substitutions only for the conventional way of background subtraction. After that, quantification proceeds along the classical line using eq. (3.2). Since the initial results of the substitute techniques are promising, it is considered worthwhile to explore the qualitative and quantitative potentials of the formalism in more depth. With respect to the quantitative application, it is regarded as particularly important that further experimental evidence or even mathematical proof be provided demonstrating its truly quantitative potentials.

An alternative way of analysis has been proposed, based on spectral digital linear

filtering of EBL-spectra and ESI sequences. Initially [Shuman85, Zaluzec85], first and second order derivative filters were used to suppress gain difference artifacts originating from the use of CCD arrays for the parallel recording of spectra and for the enhancement of such spectra. Later [Shuman87], first order difference spectra were used to quantify near-trace amounts of calcium, using the "white lines" which characterize the element in the spectrum. The proposed quantification procedure consists of the application of multiple linear least-squares (MLS) fitting of various contributions to the filtered spectrum: carbon, single and double plasmon scattering and the contribution of calcium relative to a standard. Since the main purpose of the application of the digital filters is to suppress both background (low frequency) and noise (high frequency) contributions, while maximizing the signal, there is an opportunity for optimization. The properties of several filters and their optimization were discussed in [Bonnet92c] and applied in [Michel93]. From the above mentioned literature, it is concluded that edge detection is feasible with high sensitivity in high resolution spectra of K- and L_{2,3}-shell excitations. Making use of a high brightness field-emission electron source, measurement of almost single atomic quantities has been claimed using MLS fitting [Leapman91, Leapman92a]. However, questions remain about to what extent objective criteria were employed for the detection of the element quantities and whether mass-thickness corrections were applied. Nevertheless, it would be interesting to investigate whether the mentioned techniques can be generalized to be applicable in spectrally much coarser sampled energy-filtered image sequences.

Another, entirely different aspect of the quantification principle used in this thesis is the application of a Bio-standard and the advantage of using this with respect to radiation damage. Irradiation with electrons is destructive to biological specimens. Since the Bio-standards are measured under similar conditions as the unknown, the effect of radiation damage may be expected to be at least partially cancelled.

Calibration of the concentration measurement-scale and the use of element-loaded Chelex as a Bio-standard

Element-loaded Chelex was used as a Bio-standard for calibration of the measurements in other parts of the same section. With the use of such a standard, the determination of the partial cross-section of the element and the absolute section thickness can be avoided. It was noticed in section 7.4.5, however, that the variability of element loading into the Chelex spheres is considerable. This makes them less suitable as a standard. Measurement of a larger population of Chelex spheres seems necessary to improve the reliability of this type of calibration. However, to perform such an action for each section would be very cumbersome. Section 7.4.5 also showed that the variability of $\ln(I_t/I_0)$ -measurements is considerably smaller and is, according to the results in section 7.4.3, directly related to R_{Fe} measured in Fe-Chelex. This observation suggests to use a $\ln(I_t/I_0)$ -type measurement for calibration rather than measuring R_{Fe} in the standard. Since the measurement values of $\ln(I_t/I_0)$ obtained from the Bio-standard and those obtained from epon in the same section are linearly related (section

Chapter 9

7.4.4), R_{Fe} is also related to $\ln(I_i/I_0)$ in epon. As an alternative for the currently used calibration procedure it seems possible to measure a large population of element-loaded Chelex spheres, together with the corresponding $\ln(I_i/I_0)$ -values of epon in a separate section. A calibration constant can then be estimated. Subsequently, the measurement of $\ln(I_i/I_0)$ in epon is sufficient to quantify the element in any section. Such a procedure is expected to be more precise and circumvents the embedding of any type of Chelex sphere with each specimen. To successfully apply the described alternative for calibration, $\ln(I_i/I_0)$ must be measured accurately and in a reproducible way.

During the design of the image acquisition protocol, insufficient attention was paid to the width of the slit in relation to the accuracy of the relative thickness measurement. To measure I_0 with a slit width of 20 eV brings along the realistic danger of acquiring parts of the plasmon peak. The result is that $\ln(I_i/I_0)$ is rated too low with respect to the actual t/λ .

For larger values of t/λ (>0.6), R_x tends to deviate from the linear relation with the element quantity and hence will yield underestimated results. Stephens has shown that this error can be corrected for with a relatively simple procedure [Stephens80].

Modelling of the statistical noise

The statistical noise in each pixel was modelled to originate from a normal distribution. It is a matter for discussion whether or not this is correct. Alternatives are the Poisson distribution [Unser87] or transformed versions of it. The consequences of either of the choices are currently judged to be minor since the number of electrons that is recorded is rather large (in the order of 500-2000 electrons/pixel). This makes, e.g., the normal and Poisson distributions indiscernible. Our own measurements, performed at higher doses, revealed that the deviations from the normal distribution are very small.

An aspect that was simplified during the statistical modelling described in Appendix A5 is the production of photons by the ZnS scintillator on the screen after excitation. The maximum number of photons produced by an incident electron depends on the energy of the electron. In the energy-filtering mode of the EM 902, this energy is virtually the same for all electrons (depending on the energy-width selected by the slit). The actual number of photons produced depends on several other factors and shows statistical fluctuations. Further research is needed to elucidate the effect on the currently developed techniques.

Light-optical filters and their use for control of the intensity dynamic range

The optical neutral density filters are not only used to cover the large dynamic range of the intensity but they are also used for the measurement of the camera characteristics. A newer version of the filter device, with the capability of holding more filters with smaller density increments, has been developed. This device is designed for operation under computer control and enables a better tuning of the filter density to the brightness situation. Advantages of the filter-based dynamic range control are the possibility to use a constant illumination system and a fixed camera setting and the simplicity of implementation. Questions may be raised,

however, about the linearity of the scintillator on the screen in response to the large variations in projected image brightness. However, under normal quantification conditions, the "unknown" and the Bio-standard are acquired in the same experimental setting. Calibration is therefore expected to compensate for such non-linearities. Nevertheless, further investigations into this direction are needed.

An alternative for the filter-based regulation of projected brightness may be the calibrated control of the illumination system. An advantage of this method is the more constant projected electron intensity, implying that both screen and camera can be used under stable conditions. A drawback of this approach might be the deformation of the specimen under the varying illumination conditions.

Image restoration

Three corrections are applied to each raw spectroscopic image of a sequence before analysis is started: shading correction, γ -correction and correction for specimen drift. The corrections for camera-related effects (shading and γ) are satisfactory in the case of the SIT-66 camera. The TYC9A-SIT is originally a low light level camera with automated gain control. It was modified for measurement purposes. The resulting system is apparently less stable under varying illumination conditions, since after correction rest-shading can still be observed in the image corners.

Although it is attempted to avoid lateral specimen drift by a firm contact between the specimen grid and the grid holder, in most cases some drift is nevertheless present during the period for acquisition of an image sequence (approximately 5 minutes). Unfortunately, correction of this phenomenon cannot yet be performed completely automatically, because of the strongly varying contrast. In [Heel92] and [Bonnet88b] some alternatives for standard correlation are given.

An effect that is not corrected for is the image blur introduced by the SIT-camera, operated under low light-level conditions. The analysis of relatively small amounts of element present in tiny objects is hampered by this type of image blur.

Comparison of theoretical and experimental cross-sections

The element-loaded Bio-standard was used as a replacement for the quantity $\sigma(\beta, \Delta)$. If eq. (3.2) is rewritten as an explicit expression for $\sigma(\beta, \Delta)$, experimental values for the partial cross-section can be obtained. In one of the experiments, a value for $I_k/I_T=42.1 \times 10^{-6}$ was measured in Fe-Chelex with a concentration $N=1.64 \text{ at/nm}^3$, obtained with parameters $\beta=17 \text{ mrad}$ and $w_\Delta=60 \text{ eV}$. Depending on the section thickness, the $L_{2,3}$ partial cross-section of iron can be calculated to be between $5.1 \times 10^{-21} \text{ cm}^2/\text{atom}$ and $2.6 \times 10^{-21} \text{ cm}^2/\text{atom}$ for a thickness value in the range of 50-100 nm. This is somewhat higher than the theoretically determined hydrogenic cross-section $\sigma_{L_{2,3}}(\beta=17 \text{ mrad}, w_\Delta=60 \text{ eV})=2.5 \times 10^{-21} \text{ cm}^2/\text{atom}$ as computed with the SIGMAL2 program [Egerton86]. Several reasons may be given for this deviation. First of all, the section thickness may be larger than 100 nm. Although not monitored for this case,

Chapter 9

former measurements of routinely obtained sections, revealed values between 30 and 75 nm. Therefore, this must be ruled out as a likely explanation. Another point of doubt is the fidelity of the hydrogenic model. In the literature, differences between results from this model and experimental results of about 10% are reported for slightly more favourable conditions ($w_{\Delta}=100$ eV) [Hofer91]. Yet another possible origin for the indicated deviation may be that the value measured for I_{τ} is too low, because of the hypothesized non-linear response of the scintillator screen. If the latter hypothesis is correct, the intensity response of the screen is underestimated by not more than a factor of 2 over the dynamic range of 10^6 .

Visual interpretation of element distributions; should I_k - or R-images be used?

When visualization rather than quantification is the major objective of the analysis of elemental distributions, one may raise the question whether it is absolutely necessary to divide net-intensity I_k -images by the zero- and low-loss contributions. In other words, is it possible to visually judge elemental variations from an I_k -image rather than from an R-image? Consider the example in Fig. 7.3, where the I_k -image and the R-image of one of the previously used superimposed Fe-Chelex containing sections are shown. Also shown are the $\ln(I_k/I_0)$ -image and a sketch of the situation in this part of the section. Section thickness and mass thickness differences result in variations of the local I_k -values. Visual interpretation of the I_k -image in Fig 7.3 is therefore very problematic, whereas the R-image clearly provides the expected variations in elemental amount. In the given example, the absolute thickness as well as the thickness variations are extreme. Nevertheless, the conclusion is that utmost care must be taken when semi-quantitatively interpreting I_k -images. R-images are also preferred for this purpose.

Part II.

Application of ESI-analysis in pathology

Chapter 10, Electron spectroscopic image analysis of cellular iron in an overload situation

10.1 Iron overload in the liver

Iron is a biometal, indispensable to the human body. In a normal situation, 3-5 g is present in the body and this quantity is delicately balanced by nutrition intake (0.5-1.5 mg per day), compensating excretion and loss [Bothwell79, Eijk93]. Iron, as part of the hemoglobin molecule, plays an essential role in the transportation of oxygen, and also works as an electron transfer complex in enzymatic activity and many other processes. Human erythrocytes (red blood cells), containing hemoglobin, have an average life cycle of 120 days. Macrophages in the spleen and the liver remove the dead erythrocytes from the blood circulation and digest them. The released iron is bound to a bioprotein, called transferrin, for transportation. It is then recycled in the bone marrow to form new erythrocytes, or used in other tissues. Released or absorbed iron can also be stored in ferritin, which is another bioprotein. A very small portion of ferritin is present in the circulation, a major part is found in the liver and in the spleen. Although vital, iron can be very harmful if not bound adequately. Free radicals are, e.g., produced in the presence of catalytic amounts of iron and cause damage to membranes through lipid peroxidation [O'Connell86].

There is no mechanism in the body for the active excretion of surplus iron. If the recycling of iron or its uptake is disturbed, either a shortage or an excess of the element will result. A shortage induces iron deficiency anemia. An excess of iron leads to iron storage disease, i.e. hemochromatosis [Bothwell88]. The latter disorder is particularly relevant for this thesis and involves superfluous iron stored intracellularly in some form. When the absorption and storage of iron are excessive and a familial nature is observed, the disorder is called idiopathic hemochromatosis. This disease is believed to be related to a genetic disorder [Simon76], which indicates that the cause is primary. Other forms of hemochromatosis are secondary in nature, such as blood transfusion induced iron overload.

The treatment of hemochromatosis depends on the type of the disorder. If the cause is not related to a defective erythropoiesis, phlebotomy is an effective way of removing iron from the body. An alternative treatment exists in the form of iron chelation therapy with desferrioxamine (Desferal[®]). This subcutaneously or intravenously administered chelator mobilizes iron from its stores and removes it from the body through renal excretion. Because the way of administration is problematic, a considerable effort is put into the development of oral chelators [Kontoghiorghes85, Porter89, Hider90].

In some cases of overload, the storage of iron in the body is rather diffuse, in other cases a more specific storage location is observed, such as the liver in idiopathic hemochromatosis. The liver not only plays an important role in the digestion of dead erythrocytes but also in the detoxification and apparently in the storage of iron. Therefore, liver tissue is attractive for investigating conditions of iron overload.

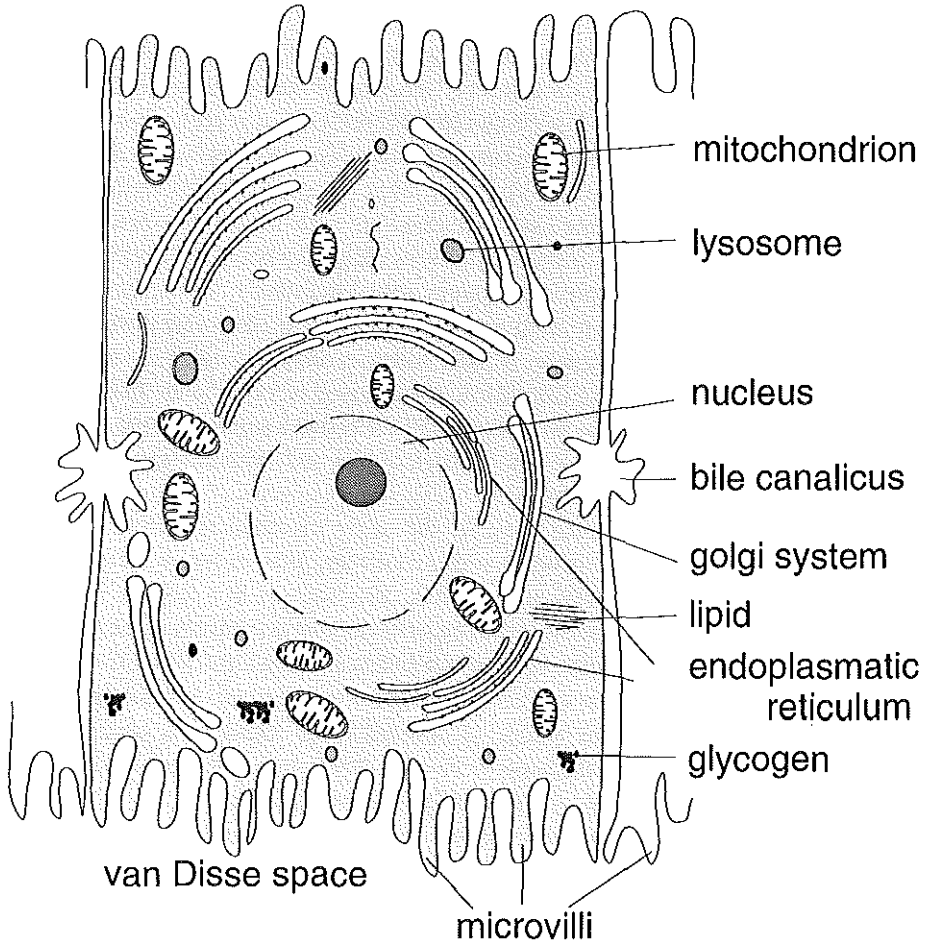


Figure 10.1 Liver parenchymal cell.

Electron spectroscopic image analysis of cellular iron in an overload situation

One of the most important iron storing cells in the liver is the parenchymal cell. Fig. 10.1 shows a cross-section of such a cell. Recently, better knowledge has been obtained about the process of iron accumulation, uptake and release in the liver parenchymal cell. There are indications that the whole process is mRNA regulated and mediated by specific proteins [Hentze87]. Several chemical structures play a role in the binding and storage of iron. Apotransferrin is a molecule synthesized by the parenchymal cell. It is able to bind one or two atoms of iron and is subsequently called ferric transferrin. Its task lies mainly in the transportation of iron through the body. A receptor mechanism followed by endocytosis enables the uptake of ferric transferrin from the blood by the parenchymal cell [Renswoude82]. Another molecule, mainly involved in the storage of iron, is ferritin. Ferritin is composed of 24 proteinaceous subunits. Two different types of subunits are found, one with a mass of 21 kDa, the other of 19 kDa [Drysdale77]. Probably, ferritin is a heteropolymer, with an apo-mass of 460-550 kDa [Harrison77]. Geometrically, the molecule consists of a shell of subunits with an outside diameter of approximately 12 nm and a central cavity [Granick46]. Iron is stored in the cavity in the form of ferrihydrite ($5\text{Fe}_2\text{O}_3 \cdot 9\text{H}_2\text{O}$) and is associated with a variable amount of phosphorus. Probably, *in vivo*, an average of about 2000 atoms Fe is stored in one molecule [Harrison77, Massover93]. Because of this large number, iron-loaded ferritin is a macromolecule which is visible in the electron microscope without additional staining or labelling. From 1966 onwards, great effort has been put by several groups into the research of the structure and function of ferritin; see reviews in [Jacobs74, Harrison91, Crichton92, Massover93]. Despite these attempts, many aspects remain unclear, such as the exact mechanism of iron uptake in ferritin as well as its release. The third and spatially largest form of iron storage is in hemosiderin. It is generally considered as a degradation product of aggregated ferritin and is found in lysosomes of patients with a long iron accumulating history. Hemosiderin, in contrast to ferritin, is water-insoluble and has an ill-defined constitution [Jacobs74, Richter78, Ringeling90&91, Ward92].

Light-microscopical observations of Perls' blue (iron specific) stained liver sections show that the iron containing parenchymal cells are arranged concentric around the descendants of the portal vein in each lobe. This indicates that the iron load on parenchymal cells which are more closely located to the central vein, is either less or is later imposed on these cells. The higher the load, the more widespread the iron distribution. Histological grading systems for overload have been defined, using this progression [Scheuer77, Sindram&Cleton86].

The morphology of structures in which iron is stored in the liver parenchymal cell depends on the severity and type of overload [Richter78, Iancu83]. Ultrastructurally, ferritin is found as individual particles in the cytosol or arranged in clusters or arrays located in relation to a substrate (e.g. lipid structures). Ferritin-like particles are also observed in lysosomes and in lysosomal structures, called siderosomes [Richter78]. Siderosomes were functionally defined by Cleton as iron-containing lysosomes that have lost their enzymatic activity [Cleton88]. Morphologically, clusters are ferritin aggregates without a membrane,

Chapter 10

while lysosomes are membrane-bound. Siderosomes contain, in addition to ferritin, hemosiderin. In the electron microscope, the membrane of such organelles is difficult to observe and sometimes not visible at all. The discrimination between clusters, lysosomes and siderosomes on morphological grounds is frequently difficult. The genesis of these structures is a matter of speculation, as electron microscopy only provides a static view [Richter84]. One of the most popular views about iron storage due to iron-overload is as follows: in response to the iron stimulus, the parenchymal cell first starts to synthesize apo-ferritin and each ferritin molecule is filled to a certain level with iron. With ongoing load, more molecules are created and subsequently clusters are being formed [Iancu83]. The trigger for clustering is unknown. With further load, clusters are surrounded by a membrane which may fuse with primary lysosomes, forming structures in which ferritin is believed to be degraded by protein-digesting enzymes. As a result, the iron-protein ratio increases [Richter84, Andrews87]. With ferritin digested to a certain level, these structures fuse again to form siderosomes, which are more or less static bodies also containing rest products, such as lipids and pigment (lipofuscin). Some observations indicate that after a while the siderosomal membrane breaks up or becomes 'leaky' [Iancu83, O'Connell86].

It can be seen from the above discussion, that many aspects of the iron storage metabolism are not yet (fully) understood. An important issue is what happens to the iron stores during treatment of patients. Idiopathic hemochromatosis is treated by phlebotomy. The effect of this treatment on patients has been discussed in [Sindram&Cleton86, Cleton88]. Under experimental conditions, iron overload can also be induced in animals and the effect of phlebotomy on such animals has been described in [Mostert89, Cleton89]. These biochemical and ultrastructural studies reveal that the total ferritin content in the liver decreases, while the average iron loading per molecule remains constant. This implies that ferritin molecules are catabolized specifically [Mostert89]. There are indications that ferritin in the liver is first removed from the sinusoidal lining cells and not from the parenchymal cells [Cleton89]. Lysosomal structures decrease in size [Cleton86], siderosomes decrease in number and it has been observed that the iron content per lysosome also decreases [Cleton88]. It was also shown that phlebotomy induces enzymatic activity in iron containing lysosomes and siderosomes [Cleton88].

Until recently, the iron content in liver tissue organelles was measured by X-ray microanalysis with 50-100 nm spots. Single samples or scanned images of 16x16 pixels were obtained of the organelles [Cleton86, Cleton88]. The geometric constraints of the relatively large spots are considerable. Each spot must be contained entirely in the object to yield a valid measurement, thus the shape of the object is difficult to follow and the limited spatial resolution allows only coarse details to be resolved inside objects. The first part of this thesis shows that with ESI, we are able to obtain quantitative iron-distribution images with a resolution which is approximately 5-10 times better than in the studies of Cleton. Preliminary results obtained with quantitative ESI-analysis revealed that the iron distribution in the lysosomes and siderosomes is highly inhomogeneous. In this chapter we investigate how the

Electron spectroscopic image analysis of cellular iron in an overload situation

resolution improvement contributes to answering questions related to iron storage in liver parenchymal cells and the effect of phlebotomy on the iron storage in these cells. Two problems are addressed specifically. One question is whether the unloading of the cell is organelle-specific. In other words, is the loading level of iron gradually diminished in all iron containing structures in all cells as suggested by the results in [Cleton88], or are the structures depleted one by one. The second question is related to the chemical nature and morphology of stored iron. Generally, the morphology of iron containing structures is studied in transmission electron micrographs, because of their relatively dense appearance. Iron storage, however, is frequently associated with other electron dense structures, such as lipids. Consequently, the iron specific contribution to the density is not known and frequently the discrimination based on density is difficult. ESI offers the possibility of observing the morphology and quantity of single element distributions. The iron distributions obtained by ESI will be compared to conventional electron micrographs and it is investigated to what extent the iron structures can be characterized biochemically. It was expected that the degradation of ferritin into hemosiderin could be observed as an increase of the local concentration, because of the biochemically determined increase of the iron-protein ratio [Richter84, Andrews87]. Consider the observation of ferritin molecules in low resolution, i.e., such that no individual particles can be resolved. For this case, no coincidental row-arrangements in the depth-direction have to be taken into account. If an average ferritin loading of 2000 atoms Fe/molecule is assumed, combined with a volume of approximately 1000 nm³ per molecule, a maximum concentration of 2 atoms/nm³ can be explained as originating from ferritin compounds. This concentration may be reached if the packing of the molecules is as compact as possible. With an unchanged core-loading, concentrations above this value must then be assumed to indicate degradation products of ferritin. In that case, subunits may have been removed from the protein shell or the subunits are modified into smaller components. Several authors report the presence of smaller units (e.g., 14.5 kDa) in biochemically separated iron-containing non-ferritin lysosomal compounds [Ringeling90, Crichton92]. The highest value that may be expected in hemosiderin is approximately 16 atoms/nm³ if all protein has been removed. The maximum concentration values for ferritin and hemosiderin mentioned above occur only if the packing of the molecules has a space-filling arrangement. In a slightly less tight packing, such as, e.g., in a cubic arrangement, the expected concentrations are almost a factor two lower.

10.2 Materials and methods

The material was obtained from an iron-overloaded male patient, 37 years of age. Clinically, the patient was diagnosed to have an idiopathic hemochromatosis. Liver biopsy specimens were obtained before and after phlebotomy. The treatment consisted of 20 venesections by which a total amount of 3 g iron was removed from the body. Perls' blue staining of histological sections revealed a grade 4 overload according to Scheuer [Scheuer77] before phlebotomy and grade 1-2 after treatment. Several tissue blocks of 1-2 mm³ were

Chapter 10

glutaraldehyde fixed, post-fixed with OsO_4 and embedded in Epon together with Fe-loaded Chelex. Ultrathin sections of approximately 60 nm were subsequently cut and put on 200 mesh copper grids without a carrier film. Material of the patient before and after phlebotomy is referred to by A and B, respectively.

To analyze the amount of iron in parenchymal cells, ESI-sequences were obtained at 12,000x magnification using the protocol described in section 8.2. The camera used was the MTI-Dage SIT-66. The sample distance in the images is 5.5 nm for the given magnification. The regions of interest were selected by the criterion that several dense structures of considerable size had to be present within the image frame. For these objects, a maximum diversity in denseness and morphology was pursued. In a number of sections, five regions were addressed to acquire data sets of the situation before phlebotomy and similarly seven regions for the situation after phlebotomy. In each section, an ESI sequence of the Fe-Chelex was also acquired for calibration. Zero-loss energy-filtered transmission electron micrographs were obtained at 12,000x magnification for visual inspection of all digitally acquired regions.

The processing of the data was carried out according to the procedures outlined in section 8.3. The validity of the input data was evaluated by the analysis for non-detection and checking for drift (which in principle was corrected for) and radiation damage. The iron concentration distribution images generally showed clustered amounts of iron, such as ferritin clusters, lysosomes and siderosomes. Such structures were considered as objects. The thresholding of the SNR-image of the net-intensity image formed the basis for object analysis. These images were thresholded at the level $S'_k = 3.0$. The result is a binary image, which represents all significant iron contributions in the imaged region. Because the quantity to be measured is the concentration, it is important that each object fills the section entirely (in the depth direction). Problems related to this cannot be entirely avoided, but small objects can at least be removed and the borders of the objects excluded from the analysis. Therefore, objects with a size smaller than 70 nm, measured by the diameter of an inscribed disc, were removed. Also, the objects were eroded one iteration with a 3x3 square structuring element to remove the borders. The binary mask that remained after these steps was used to identify the individual objects.

To compare the effect of phlebotomy on the iron-loading of the objects, the average concentration of each object was determined for situations A and B. The Wilcoxon-test was performed to determine the effect of phlebotomy on the average object concentration.

The chemical characterization needs a deeper investigation into the properties of the objects. Preliminary work indicated that the iron distribution of most objects is inhomogeneous. This means that each object may consist of different chemical components. To analyze the objects chemically, these components have to be isolated and characterized. This was done by creating a histogram of the element concentrations within each object. From such a distribution, the inhomogeneity of each object was quantified by the standard deviation and the range derived from the minimum and maximum values. The relation between these parameters was analyzed with scatter plots. Earlier investigations also learned that the object

Electron spectroscopic image analysis of cellular iron in an overload situation

Table 10.1 Overview of the measurement results in situation A (before phlebotomy).

Object	Standard	N_{avg}	N_{min}	N_{max}	std-N	$\ln(I/I_0)$	$\ln(I/I_0)$	Area	CR
#	#	at/nm ³	at/nm ³	at/nm ³	at/nm ³	(min)	(max)	pixels	
A1	Chlx1	1.79	.35	2.93	.44	.49	.72	17554	1.45
A2	Chlx1	1.57	.38	3.00	.46	.54	.73		
A3	Chlx1	.92	.33	1.76	.28	.49	.63	1928	1.61
A4	Chlx1	1.27	.39	2.56	.40	.55	.69	1820	1.13
A5	Chlx1	1.09	.35	1.94	.34	.50	.65	1705	1.43
A6	Chlx1	1.20	.42	2.08	.37	.53	.70		
A7	Chlx1	1.55	.48	2.55	.36	.50	.67	11570	2.03
A8	Chlx1	1.41	.48	2.42	.32	.48	.65	6308	1.75
A9	Chlx1	1.09	.48	1.87	.21	.49	.65		
A10	Chlx1	1.14	.49	2.05	.24	.46	.61	3625	1.85
A11	Chlx1	1.11	.50	1.83	.23	.46	.61	3392	1.95
A12	Chlx1	1.21	.55	2.05	.27	.51	.66	2908	2.30
A13	Chlx1	1.01	.49	1.97	.19	.48	.64	2552	2.19
A14	Chlx1	1.35	.60	2.14	.23	.52	.63	2117	1.28
A15	Chlx1	1.42	.54	2.35	.32	.53	.65		
A16	Chlx1	.90	.57	1.37	.11	.52	.58	230	1.44
A17	Chlx2	1.48	.39	2.80	.34	.38	.53	39132	1.91
A18	Chlx2	1.23	.42	2.12	.25	.39	.53	10325	1.61
A19	Chlx2	.86	.48	1.52	.14	.42	.53		
A20	Chlx2	.89	.38	1.78	.18	.40	.52	20713	2.57
A21	Chlx2	1.04	.37	1.84	.22	.41	.54		
A22	Chlx2	1.19	.39	2.11	.27	.42	.52	5059	1.26
A23	Chlx2	1.13	.38	1.98	.25	.39	.51		
A24	Chlx2	1.06	.40	1.83	.28	.40	.49	577	1.48
A25	Chlx2	.93	.41	1.65	.27	.40	.49	374	1.37
A26	Chlx2	1.16	.38	2.08	.24	.41	.53	15292	1.62
A27	Chlx2	1.08	.41	1.84	.23	.42	.57		
A28	Chlx2	1.03	.40	2.03	.29	.41	.53	3036	1.94
A29	Chlx2	1.10	.40	1.88	.26	.43	.55		
A30	Chlx2	.85	.41	1.48	.13	.43	.52	1319	1.52
A31	Chlx2	.99	.42	1.64	.25	.40	.53	859	1.39
A32	Chlx2	.92	.45	1.44	.15	.46	.54		

Chapter 10

Table 10.2 Overview of the measurement results in situation B (after phlebotomy).

Object	Standard	N_{vg}	N_{min}	N_{max}	std-N	$\ln(I/I_0)$	$\ln(I/I_0)$	Area	CR
#	#	at/nm ³	at/nm ³	at/nm ³	at/nm ³	(min)	(max)	pixels	
B1	Chlx3	1.48	.36	2.84	.51	.32	.48	10802	1.50
B2	Chlx3	1.15	.37	2.12	.36	.33	.46	7489	1.53
B3	Chlx3	1.27	.42	2.93	.43	.29	.51	9248	1.23
B4	Chlx3	1.51	.41	3.47	.57	.29	.50	4814	1.24
B5	Chlx3	1.45	.36	2.27	.35	.29	.43	4084	1.41
B6	Chlx3	1.17	.39	2.51	.46	.31	.49	3224	2.21
B7	Chlx3	1.34	.44	2.02	.32	.31	.44	2850	1.20
B8	Chlx3	.75	.37	1.33	.17	.28	.37	1995	2.54
B9	Chlx3	1.22	.35	2.61	.48	.32	.52	5534	1.98
B10	Chlx3	1.52	.41	2.70	.51	.36	.55	3730	1.54
B11	Chlx3	1.44	.40	3.28	.51	.28	.48	23644	2.50
B12	Chlx3	1.59	.44	2.59	.38	.28	.49	6562	1.24
B13	Chlx3	.99	.47	1.67	.22	.33	.42	311	1.14
B14	Chlx3	.81	.44	1.21	.13	.32	.39	295	1.55
B15	Chlx3	.71	.45	1.16	.12	.31	.38	171	1.39
B16	Chlx4	2.18	.52	3.94	.68	.31	.51	23136	1.36
B17	Chlx4	2.41	.47	4.71	.96	.26	.55	9729	1.88
B18	Chlx4	1.27	.39	2.70	.37	.34	.55	23563	3.21
B19	Chlx4	.71	.40	1.17	.07	.37	.45	708	2.22
B20	Chlx4	1.00	.40	2.33	.27	.32	.55	25332	2.89
B21	Chlx4	.96	.43	1.61	.15	.39	.50	2422	1.46
B22	Chlx4	.99	.41	1.53	.20	.37	.46	838	1.31

histograms may consist of several more or less overlapping peaks. When the location of these peaks is used to segment different contributions by concentration thresholding, errors are likely to occur. Because the regions from which the histogram peaks originate are believed to be compact, this property was used for their delineation. This was done with the dual-threshold operation $DTH(T_H, T_L)$. The operation works as follows. Two binary masks B_H and B_L are created by thresholding the input image with a high (T_H) and a low threshold (T_L), respectively. B_H is expanded by binary propagation within the mask defined by B_L . The result is that only those objects are reconstructed that are detected by both thresholds. If T_H is taken equal to the modal value of a peak in the histogram and T_L equal to the lowest (estimated)

Electron spectroscopic image analysis of cellular iron in an overload situation

value of this peak, the number of false detections is reduced. If the isolation of regions is started with the peaks corresponding to the highest concentrations, these regions can be excluded from the detection mask when proceeding to lower concentrations. In the detected object regions, the average concentration was measured and compared to the maximum ferritin-related concentration value that could be expected in this region on the basis of the maximum in vivo loading of ferritin molecules and their spatial arrangement.

Analysis of the morphology of the objects was restricted to the measurement of the object area (A) and the contour ratio (CR). These features were only evaluated for those objects not connected to the image border. The object area is defined as the sum of all object pixels and the contour ratio is defined by:

$$CR = \sqrt{\frac{\text{perimeter}^2}{4\pi A}}$$

Circular objects have a CR -value of 1, for non-circular objects, $CR > 1$. Both features were studied in relation to the average object concentration and the inhomogeneity (standard deviation). The morphology of the element distribution images was visually compared to the analog electron micrographs.

10.3 Results

The five data sets for situation A were processed and analyzed. In total, 32 objects were detected, integrally covering an area of $5.70 \mu\text{m}^2$. Table 10.1 gives an overview of the conditions and measured feature values per object. The objects are grouped per image and it is indicated which objects were calibrated with the same standard. Thus, e.g., the objects A20-A25 were measured in one image and calibrated with Chelex sphere Chlx2. For situation B, 22 objects were obtained with a total area of $5.16 \mu\text{m}^2$. The results are similarly presented in Table 10.2. With a mean value of the average object concentration of $1.16 \text{ atoms Fe/nm}^3$ for situation A and 1.27 atoms/nm^3 for situation B, the objects in the latter case seem to be slightly more heavily loaded. Since the distribution of the average object concentration was not normal for either of the situations A and B, the Wilcoxon-test was used ($\alpha=5\%$). This test revealed no significant difference in average object concentration before and after phlebotomy.

The concentrations in each object were analyzed further to investigate whether it was possible to chemically characterize the iron in situ. For situations A and B, the concentration ranges were $0.33 - 3.00 \text{ atoms/nm}^3$ and $0.35 - 4.71 \text{ atoms/nm}^3$, respectively. For both situations, concentrations exceed values that can be explained as derived from ferritin. Fig. 10.2 shows a scatter plot of the distribution averages and extremes per object versus the standard deviation per object. This figure and in particular the regression lines for N_{avg} and N_{max} show, that there is a clear relationship between the iron loading of the objects and the degree of inhomogeneity reflected by the standard deviation. Concentration histograms were constructed for each object (see, e.g., Figs. 10.4 and 10.6). From the shape of these histograms it was concluded that the majority of the structures was truly inhomogeneous. Multimodal

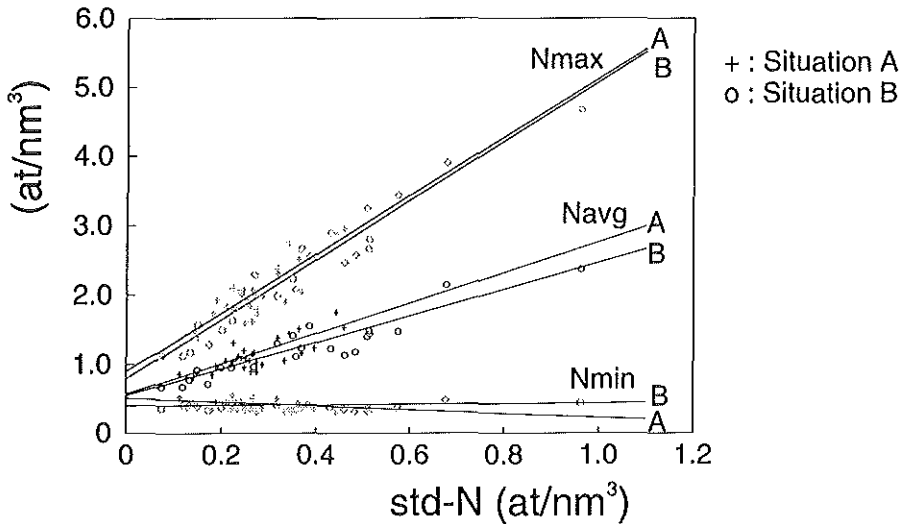


Figure 10.2 Scatter plot of the three concentration derived quantities N_{min} , N_{avg} and N_{max} versus $std-N$.

histograms and degenerate forms, like shoulder histograms and skewed histograms are observed. Such profiles indicate that in the corresponding objects, the iron is apparently in a number of similar states. In the histograms, the location of peaks may be different in different objects. This is not only true for objects in distant locations (different cells or distant positions within a cell) but also for objects that are close together, even within one image ($2.7 \mu\text{m}$). One peak location, with a modal value of approximately 0.7 atoms/nm^3 , is frequently observed. Two typical inhomogeneous cases were analyzed further, one for each of the situations A and B. For example A, Fig. 10.3 shows the iron concentration distribution image together with the object mask and the corresponding electron micrograph. In Fig. 10.4, the histogram profiles of all objects are presented (including the border-touching ones). The object labels correspond to those in Table 10.1. The average concentration for this example, calculated pixelwise, is 1.61 atoms/nm^3 . Similarly for situation B, Figs. 10.5 and 10.6 show the images and histogram profiles, respectively. The average pixel concentration in this case is 1.30 atoms/nm^3 . For both examples A and B it was tried to discern object subregions in the images that correspond to the observed major histogram peaks. Because these peaks have large overlaps and visually the subregions are of the compact type, the dual thresholding algorithm was used for segmentation. Three major peaks were visible in both situations. For example A, image segmentation was performed with $DTH(2.10,1.60)$ to extract the object

Electron spectroscopic image analysis of cellular iron in an overload situation

Table 10.3 The average concentration, determined for the regions obtained at each level, before (A) and after (B) phlebotomy.

Level	$^A N_{\text{avg}}$ atoms/nm ³	$^B N_{\text{avg}}$ atoms/nm ³
I	0.66	0.78
II	1.26	1.46
III	2.02	2.44

regions that compose the highest peak, followed by DTH(1.30,0.80) for the middle one and the original mask for the lower peak. Example B was processed similarly with DTH(2.50,2.00), DTH(1.50,1.00) and the original mask, respectively. Figs. 10.7a and b show the results, with the object regions corresponding to the highest values labelled in white (level III), the middle peak in light grey (level II), the lowest values in dark grey (level I) and the background in black. For each example, the average value of each region was computed. The results are shown in Table 10.3.

The quantitative results of the analysis of the morphology by area measurement and contour-ratio measurement are collected in Table 10.1 for situation A and in Table 10.2 for situation B. The missing values for each of the situations are caused by the fact that objects touching the image border were not measured. To investigate the relation between the average object loading and the morphology, scatter plots of the area A versus N_{avg} and of CR versus N_{avg} were made, as shown in Fig. 10.8a and b, respectively. The relationship between std-N and both morphological parameters was also plotted, but as can be understood from Fig. 10.2 in which an almost linear relationship between N_{avg} and std-N is suggested, these representations did not yield any new information and are therefore not shown. Finally, Fig. 10.8c shows the relationship between the morphological parameters.

For a qualitative treatment of morphology, the iron distribution images were compared with the more conventional (energy-filtered) analog electron micrographs. Fig. 10.3c and Fig. 10.5c show examples of such micrographs before and after phlebotomy treatment. Fig. 10.3c shows dense regions that are not detected as iron-containing structures (Fig 10.3a). Some large objects, like B3 as observed in Fig. 10.5c, contain more dense globular subregions. Such regions are also discernable in iron concentration, as Fig. 10.5a shows. Iron containing objects are frequently observed to be associated with other dense (osmiophilic) material such as lipids.

10.4 Discussion

Effect of phlebotomy

No difference could be measured in average object concentration between the situations before and after phlebotomy. The iron that was removed from the liver was most probably not removed from the structures such as analyzed in situation B. It may even be presumed that

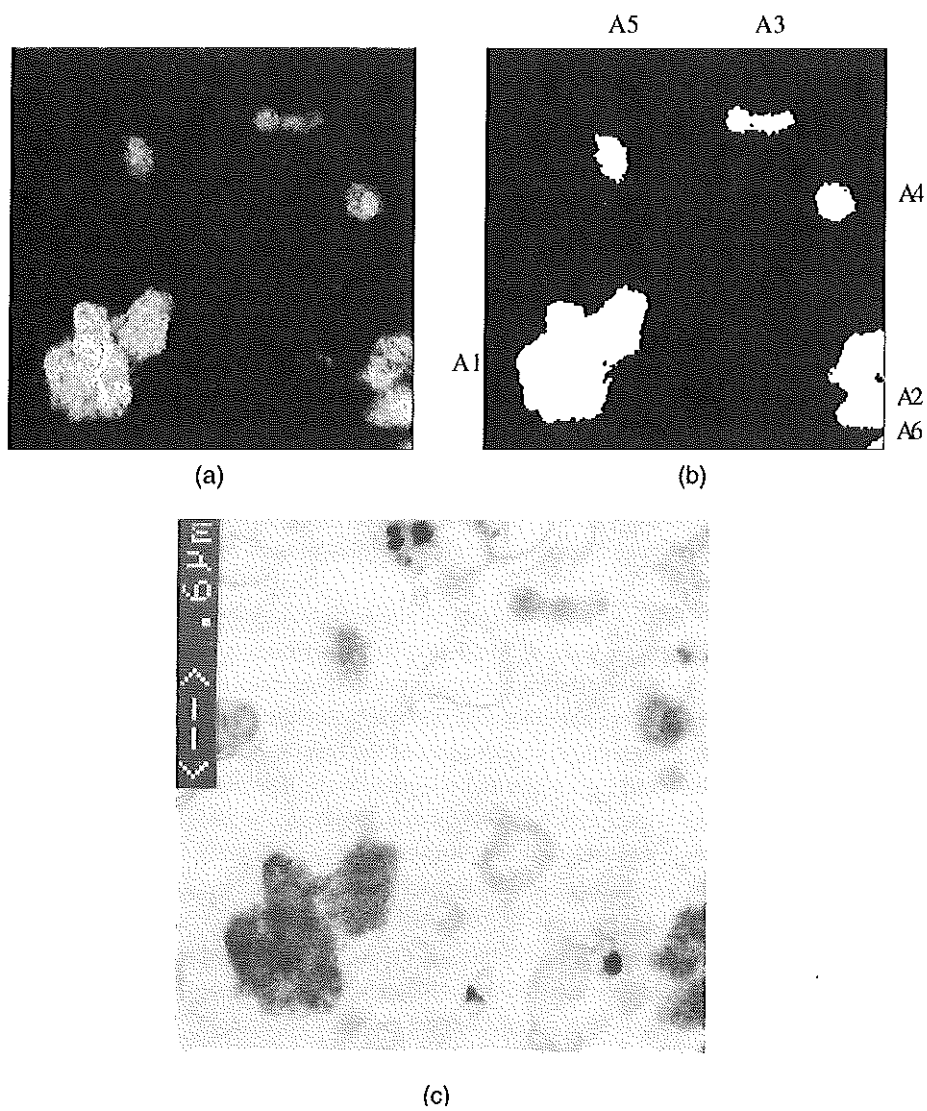


Figure 10.3 Example A: a) iron distribution b) object mask c) electron micrograph.

Example A

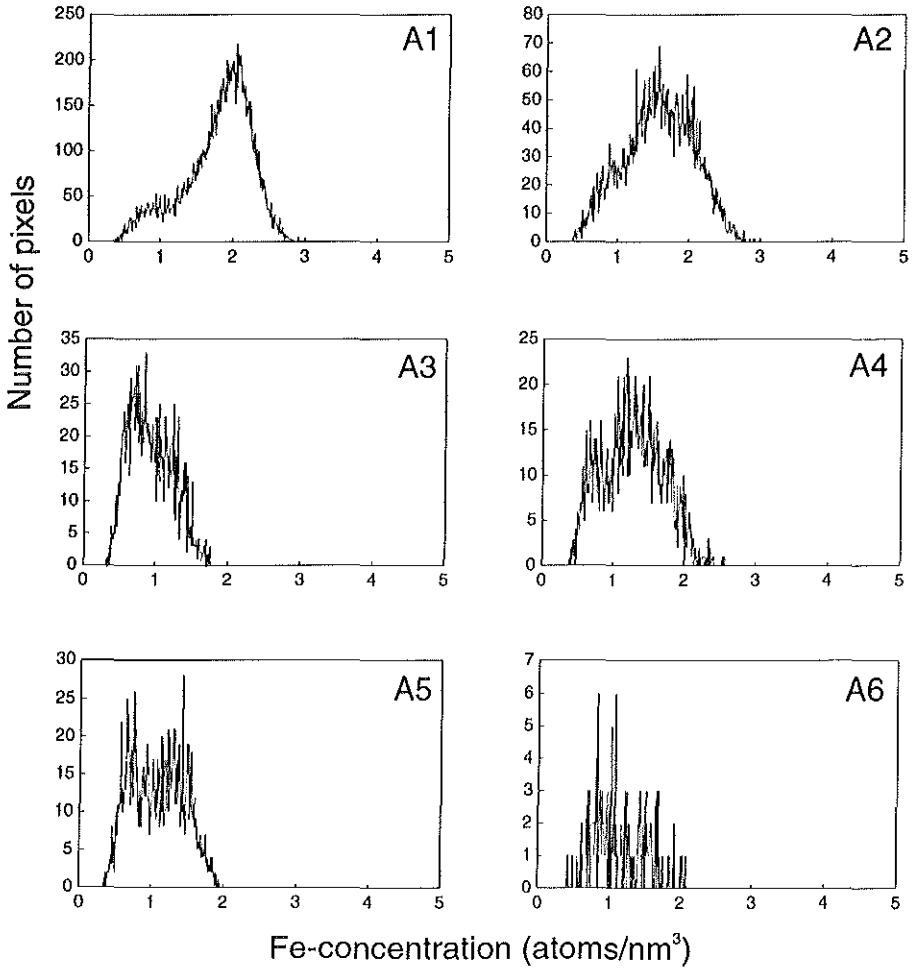


Figure 10.4 Histogram profiles of the objects in example A.

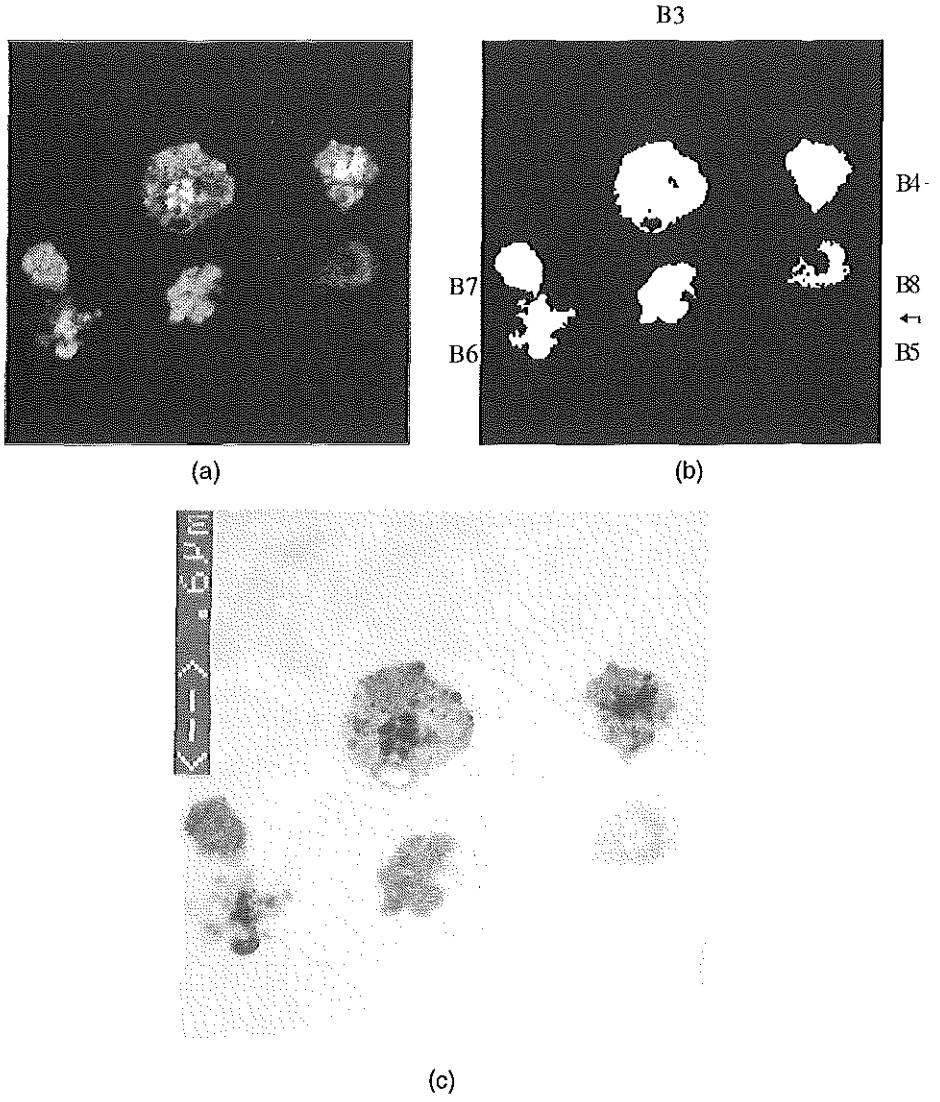


Figure 10.5 Example B: a) iron distribution b) object mask c) electron micrograph.

Electron spectroscopic image analysis of cellular iron in an overload situation

Example B

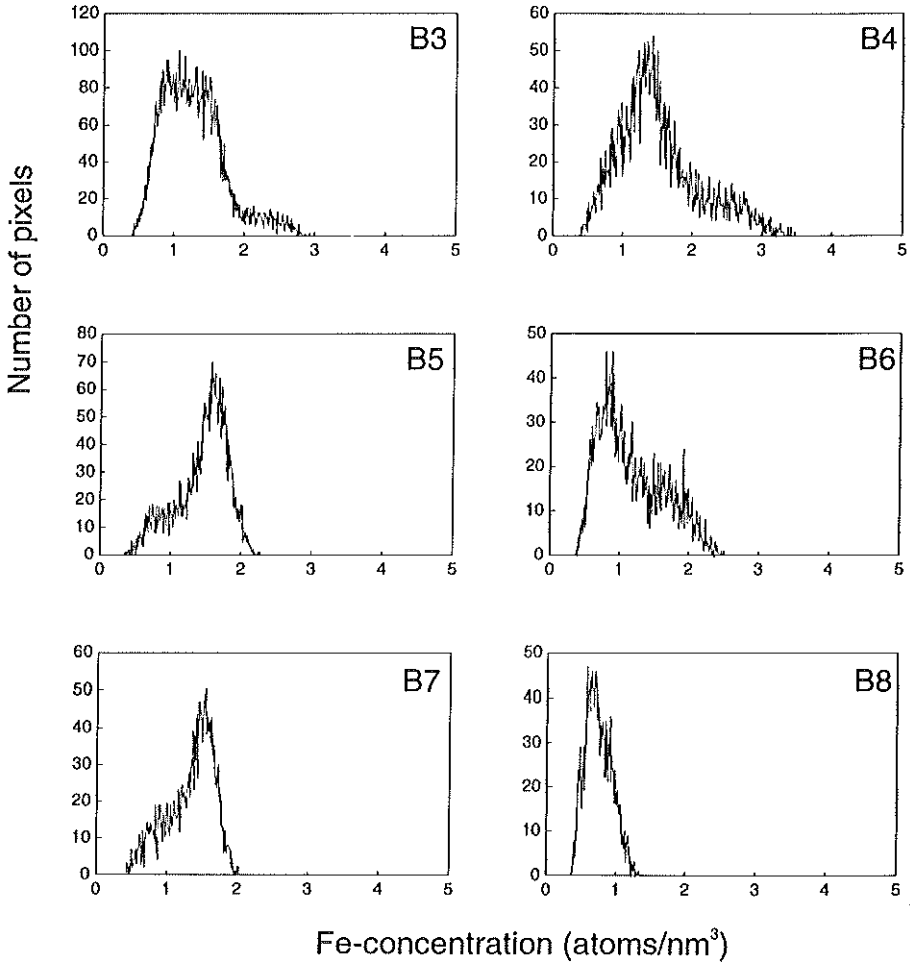


Figure 10.6 Histogram profiles of the objects in example B.

Chapter 10

the cells in which these structures lie, have not yet answered to the demand of iron. It must be noted that the measurements were performed in parenchymal cells, of which the location within the liver was undetermined. The selection of locations was triggered by the visual presence of electron dense structures, such as clusters, lysosomes or siderosomes. Because light-microscopical observations of histological sections revealed a lower grade of iron-loading of the liver after phlebotomy, but no difference between the concentration in the two situations could be measured, this experiment supports the hypothesis that iron containing structures are catabolized one by one. This is similar to the way ferritin is catabolized [Mostert89]. The result is not in agreement with the measurements performed by Cleton et al. [Cleton86]. The reason for this may be caused by the histologically insufficiently well-determined measurement locations. Because of the discrepancy, it is now believed that the location of the parenchymal cells relative to the descendant of the portal vein should be specified and that an equal number of object types (cluster, lysosome, siderosome) before and after phlebotomy should be addressed. Furthermore it should be realized that the quantitative results in this study are expressed in atoms per unit volume, while Cleton et al. expressed the quantities as weight percentages. Volume effects influence the former quantities, while mass effects influence the latter.

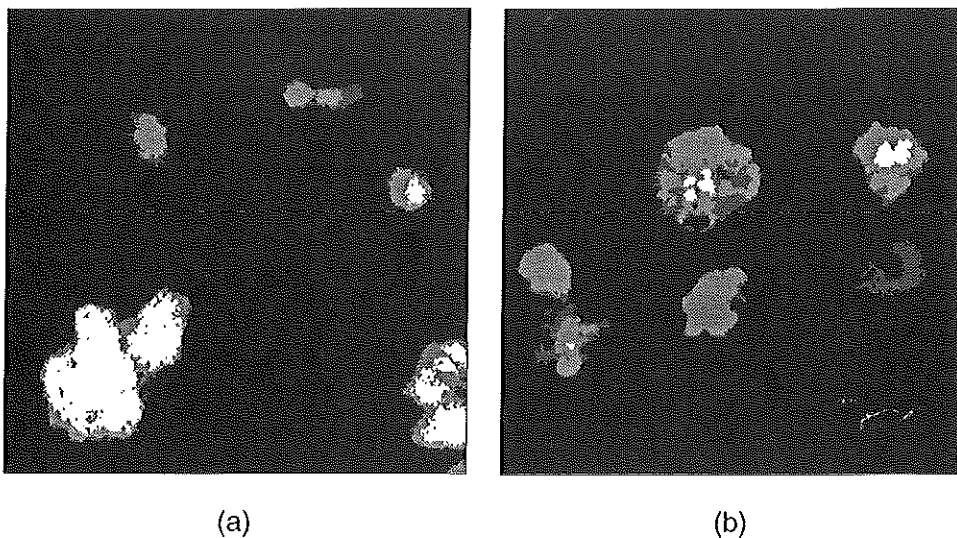


Figure 10.7 Region labelling corresponding to levels I (dark grey) , II (grey) and III (white) of iron concentrations; a) example A, b) example B.

Electron spectroscopic image analysis of cellular iron in an overload situation

Chemical characterization

In order to chemically characterize the segmented structures, the results in Table 10.2 were compared to the maximum concentration value of 2 atoms/nm³ that can be explained as originating from ferritin. To start with the lowest level (I), these contributions must be interpreted as ferritin. The spatial arrangement is apparently rather loose as the average concentrations are less than 2 atoms/nm³: 0.66 and 0.78 atoms/nm³, respectively (see Table 10.3). These measurements are consistent with the observation of the morphology visible in Fig. 10.5c. The object with label B8 typically falls into the level I category. Because of its irregularly shaped contour, suggesting that there is no membrane present, it is identified as a cluster. The individual particles in this object are randomly distributed, without a tight arrangement.

For level II, the characterization is more difficult, because for these concentrations (Table 10.3) it depends more critically on the spatial arrangement of the particles. In none of the objects have crystalline patterns been observed, which could have indicated a maximal compact arrangement. Typical level II objects such as B7 and B5, and to some extent A5 have irregularly ordered particles. Still, the particle arrangement appears much tighter than for level I. The typical objects are membrane bound and are identified as lysosomes. It is therefore assumed that the regions segmented at level II consist of lysosomal ferritin in an early stage of degradation.

At level III, regions are isolated which most certainly must be considered to consist of degraded ferritin (hemosiderin). Table 10.3 shows that the concentrations in these regions are above 2.0 atoms/nm³. Such regions are found in objects such as A1, B3 and B4. The complexity of the objects, with several differently loaded subregions present, indicates that these objects are probably siderosomes (as defined in [Cleton88]). The consistency of the concentration-based characterization and the morphological classification is again striking, since hemosiderin is believed to be exclusively found in siderosomes.

The chemical characterization as performed in this chapter is coarse, because global parameter values for segmentation were used. From the shape of the histogram profiles, it can be observed that the concentration profile in each object is different and the peaks are in different locations. This is not only true for objects in different cells, but also for objects that are close, i.e. within one image. Thus, although a rough distinction between various states can be made, the situation within each iron structure is apparently dissimilar. One might speculate about the reason for this. The most probable explanation is that the concentration differences in clusters originate from different spatial arrangements only, while in lysosomes and siderosomes this is mainly caused by the level of digestion, which in turn depends on the 'age' of the iron aggregate. The 'older' the lysosome, the more time enzymes may have had for decomposition of the ferritin and this is accompanied by more compact arrangements.

Chapter 10

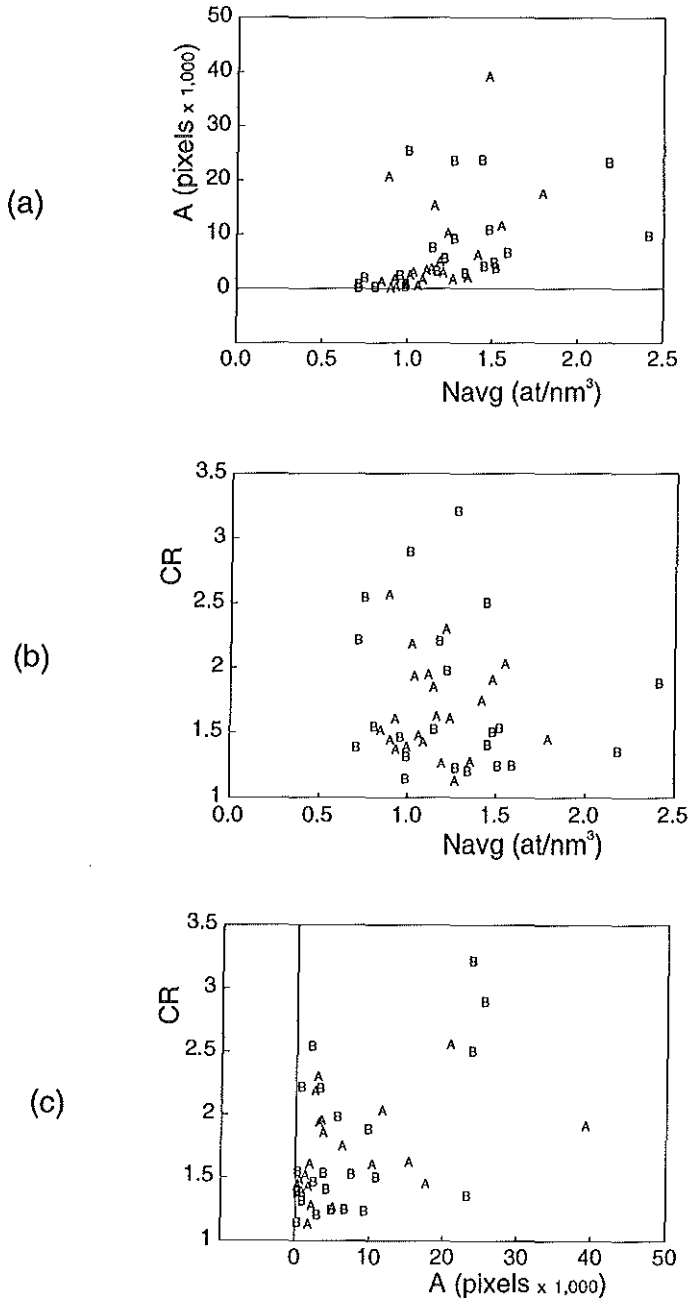


Figure 10.8 Scatter plots of (a) A versus N_{avg} , (b) CR versus N_{avg} , (c) CR versus A .

Electron spectroscopic image analysis of cellular iron in an overload situation

Morphology

Fig. 10.2 indicates that the average concentration and the maximum concentration of an object and the standard deviation of the concentration distribution of the object correlate well. The visual impression that the inhomogeneity increases with the average object loading is hereby confirmed. In the previous paragraph, it was stated that the representation of the object loading by the concentration histogram profiles such as in Fig. 10.4 and Fig. 10.6 can be used for the chemical characterization of regions. This characterization aids in discriminating object types. The purpose of the morphological analysis is twofold: to see whether simple parameters such as A and CR contribute to the type discrimination and to see whether phlebotomy has had any effect on the morphology. Fig. 10.8a seems to contain some structure. The question is whether this is artificial or not. The area of an object naturally depends on the way it was sectioned and, as a result, a large 3-D object may be seen as a small one in certain 2-D cross-sections. In Fig. 10.8b, no structure is visible at all. The conclusion of these measurements is that there is no marked difference between the situations A and B. Also, no clear indication could be obtained about the usefulness of the described morphologic parameters for the typing of the objects.

Considering the morphology qualitatively, it can be concluded that the use of the electron micrograph density as an indication for the presence of iron is questionable. Reversely, subregions with high iron concentrations are found, which correlate well with the presence of dense subregions. Because these subregions are of the compact type, it seems logical to conclude that either these regions originate from a biochemical process with a limited extent, or that they are the final result of such a process elsewhere and that these structures have been incorporated in a later stage.

Chapter 11. Electron spectroscopic imaging as a tool for the analysis of structure and composition of isolated ferritin particles

11.1 Carbon specific imaging

Ultrastructural observation of small isolated objects like ribosomes, viruses, lipoproteins has successfully been performed for several years with negative staining techniques [Hayat89]. Among such structures, ferritin particles have frequently been used as test-objects. With negative staining techniques, the final resolution obtained was limited by the thickness and grain-size of the support film and that of the staining material. The images obtained are to some extent indirect, as it is the stain that is imaged. Questions can be raised about the fidelity of the images obtained in this way. The staining material may not completely penetrate into cavities. The support film used has been produced either by metal evaporation [Langmore78] or by a chemical reaction [Kleinschmidt59]. Direct imaging would seem attractive as these problems are circumvented.

In principle, electron energy-loss spectroscopic imaging enables the direct visualization of (isolated) biological structures without any additional staining. Details about the use of STEM instruments for this purpose have been described earlier [Jeanguillaume78, Engel84, Shuman87, Krivanek91b, Leapman91, Leapman93, Leapman94]. Recently, STEM-imaging of frozen-dried biological materials was reported [Leapman93, Leapman94]. Energy-filtering transmission electron microscopes, like the Zeiss EM 902, have been used to acquire, in addition to the element-related images, structure-sensitive information by zero-loss filtering and filtering at $E=250$ eV. The information in such images filtered at 250 eV is in a certain sense also indirectly obtained. These images are acquired from a spectral region just in front of the carbon K-edge at 284 eV. Other elements present in the structure with edges at energy-losses below that of carbon appear bright, whereas the image contributions of carbon and those of elements with edges beyond the carbon edge are absent and appear dark [Sorber90a, Reimer91]. The imaging of biological structures by energy-filtering at 250 eV is advocated in [Stearns94] as a good alternative for using negative staining procedures.

Because element-specific images can be acquired, proteinaceous structures can be imaged directly by their carbon content, which in biological objects may amount to about 50 atomic % of the total number of atoms. However, carbon-based structural EFTEM analysis in ultrathin sections has not been successful for the following reasons:

- (1). The carbon in the proteinaceous structures is surrounded by or even infiltrated with a carbon-rich embedding medium, which annihilates carbon contrast.
- (2). Routinely obtained 50 nm thin sections may be considered too thick. Various small structures are seen in over-projection: in the case of the analysis of ferritin-particle clusters in liver parenchymal cells, four particles with a mean protein particle diameter of 12 nm may be present on top of each other in the 50 nm layer of an ultrathin section.

ESI as a tool for the analysis of structure and composition of isolated ferritin

For these reasons, direct imaging of carbon in separable objects has to be performed preferably in a model system with isolated single particles in a thin non-carbonaceous environment, like thin metal films [Peters86]. Two recent developments have enabled this. Elemental imaging was investigated in the first part of this thesis. Although initially developed for the quantification of iron, the imaging of carbon is a straightforward generalization. Also, the technique to create extremely thin metal (chromium) films became available [Apkarian88, Apkarian94]. Such films are strong and little interference with carbon is to be expected. For the preparation of the model system of particles, the Horne and Pasquali-Ronchetti technique [Horne74] can be used. This technique, which was originally proposed for negative staining of isolated particles, guarantees that one is dealing with neatly arranged particles in a single layer.

The visualization of carbon in individual objects seems feasible with the above described techniques. In principle, such a model system also allows to quantify the carbon content of isolated proteinaceous structures in situ. Such a result is to be compared to the values determined by bulk chemical analytical techniques from the same solution [Colliex84, Ottensmeyer84, Colliex85, Colliex86]. We will consider ferritin molecules as test objects. This molecule consists of a 24 subunit protein shell of about 12.5 nm diameter, surrounding a cavity of approximately 6 nm [Massover93]. In apo-ferritin the cavity is empty, while in an iron-rich situation it is filled with iron in a form that resembles ferrihydrite. We will concentrate on carbon visualization and on the estimation of its carbon content by ESI.

11.2 Materials and Methods

Ferritin particles were obtained from a commercially available stock solution of horse spleen ferritin (Sigma, Bornum, Belgium). Samples of this solution were diluted with double distilled water to an optical density of 0.2 at 595 nm (= 0.2 mg/ml). The Horne/Pasquali-Ronchetti technique was slightly adapted: we used a lower ammonium molybdate concentration and no ethylene glycol. Prior to use, ammonium molybdate tetrahydrate (Fluka, Bornum, Belgium) was added to droplets of the ferritin solution to a final concentration of about 1 wt %. Drops of this mixture were spread on freshly cleaved mica sheets (Agar Aids, Stansted, U.K.) by a glass rod. After initial drying at air, the sheets were covered with a pure chromium film by magnetron-Argon sputter coating, in a Denton DV-602 turbo-equipped sputter deposition system. The integral water-cooled cathode (DSM-300A) was operated at 50 mA for 60 s., at a cathode-target distance of 5 cm. The deposition thickness was measured by a quartz crystal thickness monitor. The films were floated-off on water and collected on unfilmed mesh 500 copper grids. Chromium, which has a grain size of about 0.2 nm, appears even at 0.5 nm thickness as continuous in TEM instruments with 200 kV acceleration voltage. Such tightly packed chromium films oxidize only at the surface when in contact with air. This converts the film partially into a chromium oxide film. The films on the grids were observed without any additional staining. A presumed cross-section of such a Cr-film and the

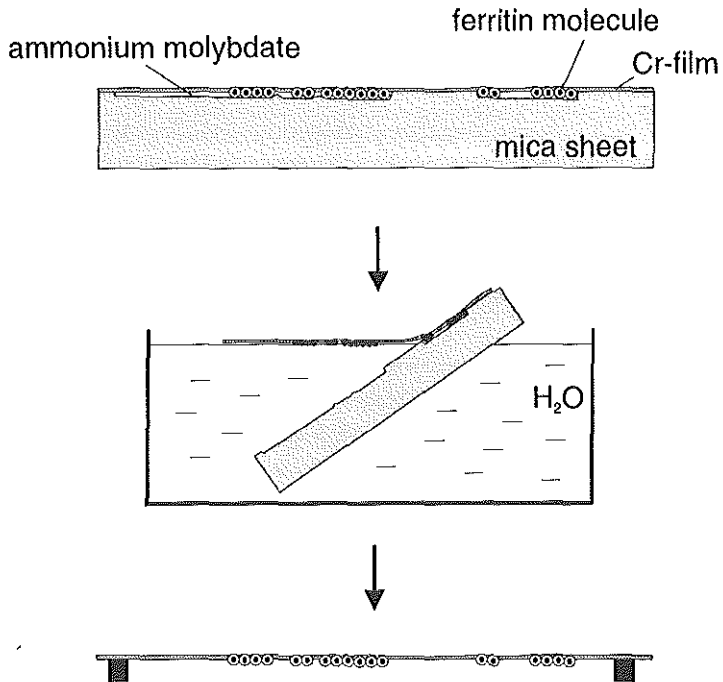


Figure 11.1 Preparation of the chromium film with ferritin. Ferritin is spread out on a mica sheet and covered with the chromium film, floated-off on water and put on a grid without support film.

preparation of a grid is shown in Fig. 11.1. C-films were prepared similarly for visual inspection of the ferritin. An aqueous uranyl acetate solution (1 wt%) was used for negative staining of these films.

The instrument set-up is described in section 2.3. Images were acquired with a Bosch TYC9A SIT camera. Electron spectroscopic imaging of the unstained specimens was performed using a protocol similar to that described in section 8.2. The theoretical resolution of the carbon distribution image, according to Table 2.1, is 2.4 nm (for $\beta=17$ mrad and $w_s=20$ eV). To resolve more detail, especially in the horizontal image direction, a magnification higher than 12,000x should be chosen. The magnification in this case was 50,000x, corresponding to a sample distance of 1.5 nm. Images were acquired at energy-losses of 184, 204, 224, 244, 264, 284 (edge), 304 and 324 eV. For zero- and low-loss imaging, optical filters with densities 4.0 and 3.0 were used. For the slit width a value of $w_s=20$ eV was chosen. The pre-edge and edge regions had widths of $w_1=100$ eV and $w_\Delta=60$ eV, respectively.

ESI as a tool for the analysis of structure and composition of isolated ferritin

The images were processed following the procedure outlined in section 8.3. Specimen drift and mass-loss were monitored and the check for non-detection was done to evaluate instrument stability. The procedures to perform these checks are described in section 7.3. Since for the images acquired with the Bosch camera an unacceptable amount of rest-shading was found in the image corners, only the central sub-image of 256x256 pixels was considered for the analysis. Visualization of carbon is possible with the I_k and R_C -images. The protein on the Cr-film does not uniformly cover the film but is arranged in lakes. To measure the amount of carbon, these protein containing regions have to be selected. This is done by image segmentation. Two strategies were followed. The first tries to delineate the carbon containing regions in general. For that purpose the carbon SNR- I_k image was thresholded. The resulting binary image represents a carbon specific mask. The second strategy tries to isolate individual ferritin molecules. For this purpose the first pre-edge image, with an energy-loss of 184 eV, was used as a contrast-image. In this image the iron-rich cores of ferritin are seen as bright spots. The diameter of these spots appear somewhat larger than 6 nm because of the various resolution-degrading factors. A top-hat filter is defined as the difference of the original image with its morphological opening [Meyer79]. Such a filter, with a structuring element size of 7x7 pixels, was found suitable to detect a sufficient number of molecules. The detected spots were subsequently skeletonized to one pixel and dilated circularly to acquire an area of 13 nm diameter to enclose the proteinaceous shell of the ferritin particle. This procedure defines a ferritin specific mask.

For quantification, the theory described in chapter 3 was applied. The absolute number of carbon atoms N_C in an analyzed area A can be determined by multiplication of eq. (3.2) by the analyzed volume $A \cdot t$:

$$N_C = \frac{I_k(\beta, \Delta) \cdot A}{I_T(\beta, \Delta) \cdot \sigma_k(\beta, \Delta)} = \frac{R_C(K, \beta, \Delta) \cdot A}{\sigma_K(\beta, \Delta)} \quad (11.1)$$

Since the specimen was not embedded and sectioned, an internal standard could not be used, bringing along the problem of the determination of the partial cross-section $\sigma_k(\beta, \Delta)$ of the K-edge of carbon. Hofer [Hofer91] compared values for K-shell cross-sections from the Hartree-Slater model, the hydrogen model and the experimental results from various authors. For carbon (for an acceleration voltage of 120 kV, $\beta=5.9$ mrad and $w_\Delta=100$ eV), values in the range $4.1-4.8 \times 10^{-21}$ cm²/atom were found. The hydrogenic model (in the SIGMAK2 implementation of Egerton [Egerton86]) was concluded to be accurate within 10% for K-edges, provided the width of the Δ -region is sufficiently large ($w_\Delta > 50$ eV). We adopted the SIGMAK2 program and calculated a value of $\sigma_K=4.8 \times 10^{-21}$ cm²/atom for the conditions used by Hofer, which is indeed close to the values mentioned in his paper. Our images are acquired at 80 kV, $\beta=17$ mrad and $w_\Delta=60$ eV. On the basis of these values, the SIGMAK2 program gave $\sigma_K=7.3 \times 10^{-21}$ cm²/atom. This value is used in the next section.

To qualitatively assess the presence of carbon, the local spectrum reconstruction technique as described in section 7.2.2 was applied to improve the SNR.

Chapter 11

Wet-chemical analysis for iron of the same ferritin stock solution was performed according to Bradford [Bradford76]. Similarly, the wet chemical analysis for total protein was performed by an adaptation of the method of Harris [Harris78]. For details, see [Gelder93].

11.3 Results

Fig. 11.2a, shows an analog contrast-sensitive micrograph acquired under zero-loss conditions. The presence of the ferritin particles is demonstrated by the iron cores in ferritin-particle lakes surrounded by bare chromium film. The fine grain of the chromium film can be seen in the areas not occupied by ferritin particles. In Fig. 11.2b, the analog contrast-sensitive zero-loss image of a negatively stained specimen displays the presence of the proteinaceous mantle around the central core. staining fails to stain. Fig. 11.2c, shows a digital zero-loss image, in which iron-cores are visible and the proteinaceous material is slightly distinguished in contrast from the free chromium film.

Because the Mo $M_{4,5}$ -edge at 227 eV is close to the carbon K-edge at 284 eV, prior to spectroscopic image analysis, EEL-spectra were obtained to assess the extent to which the molybdate solution has been removed by the wet preparation procedures. No signs of Mo could be found in the spectrum. Spectroscopic image sequences were subsequently acquired around the carbon K-edge and the background was corrected using the procedure described in section 6.2. To compare the capabilities of carbon-specific imaging with those of the already mentioned modes of observation, in Fig. 11.3a a carbon net-intensity I_k -image is shown; Fig. 11.3b shows the corresponding carbon concentration proportional R_C -image. In Fig. 11.3a, the absence of carbon in the cavity of the ferritin molecule can be observed as a relatively dark centre in each of the individual particles. The contrast between the mantle and the core in the R_C image in Fig. 11.3b is reduced, after correction for the high local core-mass density. Individual molecules can only vaguely be observed in the I_k -image, while in the R_C -representation this is not possible. From the I_k - and R_C -images it was suspected that some carbonaceous material was present between the ferritin lakes, which remained unobserved in the negatively stained specimen. Reconstructed, spatially integrated spectra confirm the presence of carbon in such regions. The nature of these has to be established.

To analyze the carbon content, the SNR- I_k -image was segmented to obtain the general carbon specific mask. Segmentation of the energy-filtered 184 eV image gave the ferritin specific mask as described in section 11.2. The contours of both masks are shown in Fig. 11.4. The area of the carbon specific region is 61,345 pixels ($0.14 \mu\text{m}^2$). The carbon content, calculated with eq. (11.1) is $N_C=22,993,150$ atoms of carbon, i.e. an average of 374.8 carbon atoms/pixel. The ferritin specific mask consists of 312 molecules of 45 pixels each. In these ferritin molecules, an average number of 16,874 carbon atoms/molecule was measured, which is equivalent to 375.0 atoms/pixel.

ESI as a tool for the analysis of structure and composition of isolated ferritin

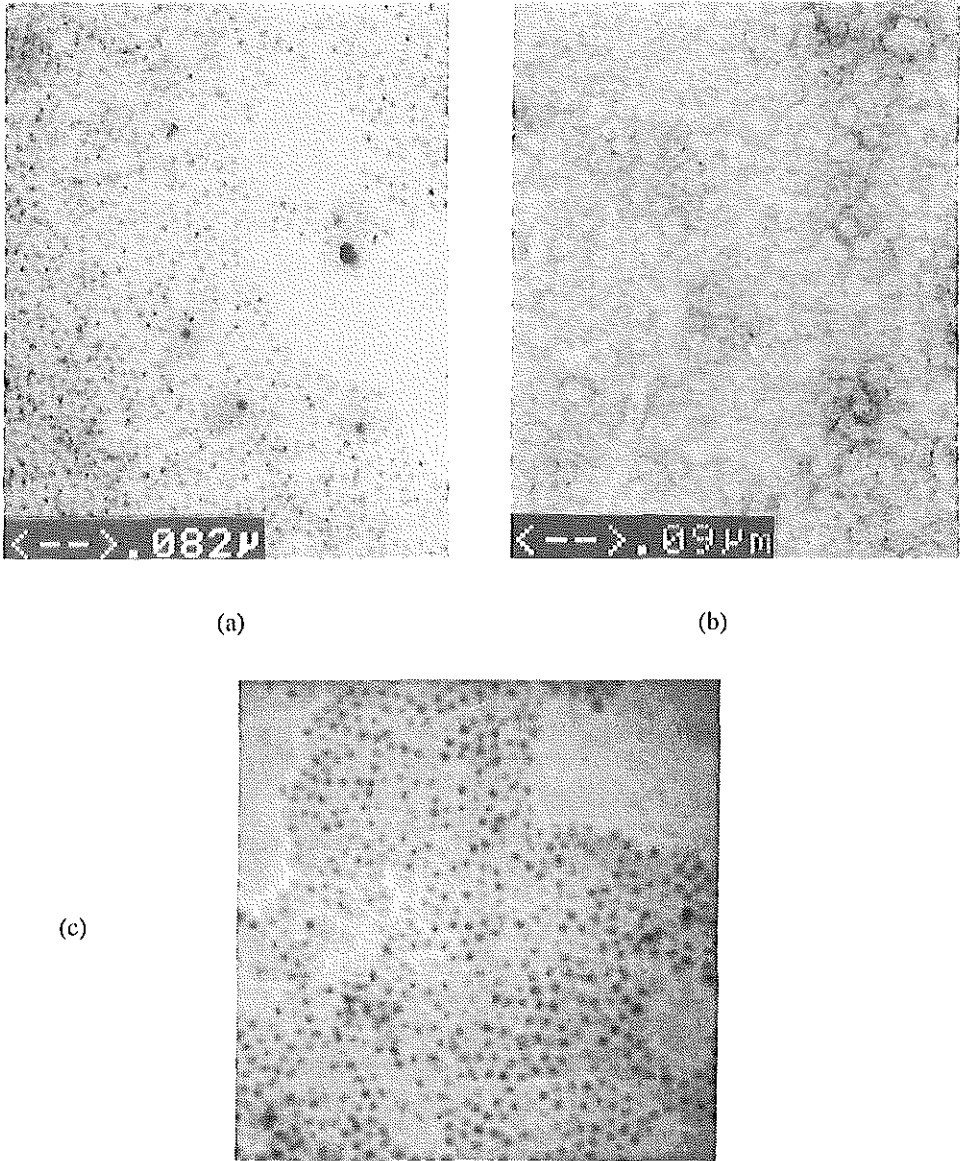


Figure 11.2 Comparison of zero-loss images of ferritin-containing films: (a) an unstained film, (b) a negatively stained film, both directly recorded on a photographic plate and (c) a digital zero-loss image.

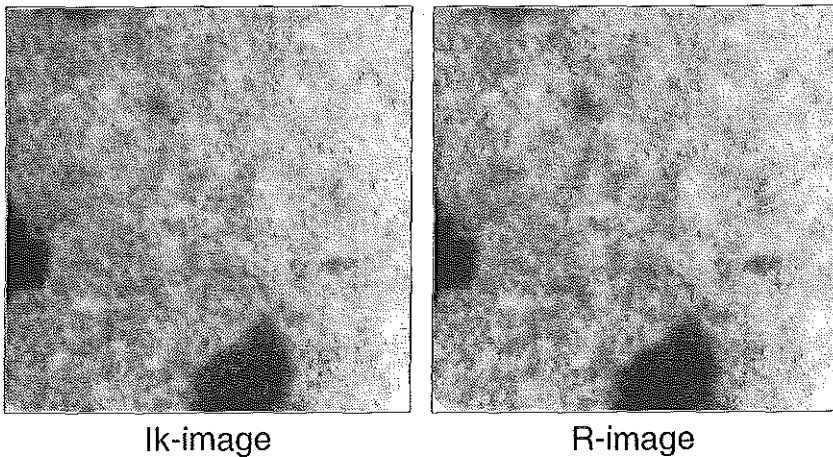


Figure 11.3 Results of carbon specific imaging. The iron cores are well localized in the net-intensity image. The contrast in the carbon distribution image is reduced to a great extent as compared to the net-intensity image.

Specimen drift was measured to be minor for the analyzed data-set and was not corrected for. During the acquisition time interval, also no significant mass-loss could be found. Checking for non-detection revealed that the image set contained sufficiently reliable information to justify imaging and quantification of carbon. Some indications of bundle drift were found. For larger magnifications under almost focused beam conditions, the instrumental primary-beam drift might cause a time-dependent shading component not modelled by the applied correction procedures. This may render some data sets unusable.

11.4 Discussion

Isolated ferritin particles have been used for years to demonstrate the analytical and instrumental potentials, both for transmission and scanning electron microscopy and for analysis by energy-dispersive X-ray spectroscopic (EDXS) and EELS microanalysis. [Bruijn81, Ottenmeyer84, Colliex84, Colliex85, Colliex86, Shuman87, Andrews93]. We used the Horne/Pasquali-Ronchetti technique to obtain a single layer of molecules firmly attached to and partially embedded in a chromium film-substrate of known thickness. This allowed us to investigate with ESI the use of carbon directly as a protein-imaging element and to study the possibility of carbon quantification. Under normal sectioning conditions with a carbon rich embedding material, or using carbon as a support film, carbon quantification becomes senseless. The thin chromium films used were 1 and 2 nm thick. Only the 2 nm films were strong enough to survive the floating-off procedure and the deposition on unfilmed grids. The

ESI as a tool for the analysis of structure and composition of isolated ferritin

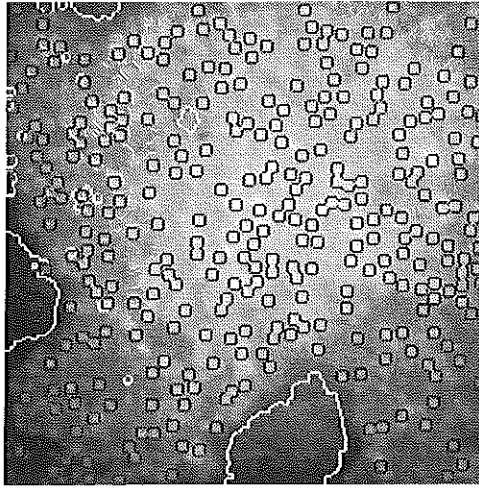


Figure 11.4 Contours of the segmented regions drawn in the $E=184$ eV image. The delineation of the carbon-specific area is shown in white and the ferritin-specific area in black.

grain size of the chromium film is such that imaging of particles with a diameter of 6-12 nm is feasible. The films appeared to be rather stable in the electron beam, at a beam intensity which was the maximum obtainable from the tungsten hairpin filament.

Comparison of imaging properties

Comparison of the (analogue and digital) images acquired under zero-loss conditions (Fig. 11.2a and c) with the negatively stained ferritin particles (Fig. 11.2b) does not contribute new aspects. At first sight, the results in Fig. 11.3a and b are disappointing because of the low contrast between the individual molecules. On the other hand, the 6 nm cores are still visible. Under ideal circumstances, the maximum contrast between core and mantle in a carbon proportional image is expected to be 27%, under the assumption of a homogeneous carbon distribution in the mantle and the absence of carbon in the core. The three main reasons for the limited amount of detail visible are: the large chromatic aberration, with a theoretical value of 2.3 nm (Table 2.1), the horizontal blurring by the camera and the probable presence of carbon containing protein fragments between the particles as also observed between the ferritin lakes. Other resolution degrading aspects are specimen drift and noise. Some possibilities for improvement are discussed below.

Chapter 11

Quantification

The acquisition of a series of images and the application of the image quantification procedure in combination with the validity checks allowed the carbon content in two types of regions to be measured. One type consisted of a general protein region, the other of a ferritin specific sub-region. The average number of carbon atoms measured in both regions was virtually the same (375 atoms/pixel). This is remarkable since only about 25% of the protein area was segmented as ferritin. Because segmentation of these particles was performed as the detection of bright spots in the $E=184$ eV image, these molecules are probably iron-loaded. The remainder of the area consists of iron-loaded ferritin missed by the segmentation, but it is likely that a certain amount of apo-ferritin is also present and probably also fragments of these molecules. Altogether, apparently, this does not influence the measured average amount of carbon per pixel.

The average carbon content per ferritin molecule was measured to be 16,874 atoms/molecule. This corresponds to a contribution to the molecular mass of 270 kDa. Unfortunately, there is little biochemical data to compare this value with. The total mass of horse spleen apo-ferritin is about 500 kDa [Massover93], which would imply that about 50% of the mantle consists of carbon. The number of iron atoms wet-chemically determined was 1,760 atoms Fe/core. If we assume that the core consists of ferrihydrite $9\text{Fe}_2\text{O}_3 \cdot 5\text{H}_2\text{O}$ [Massover93], and a number of phosphorus atoms is associated with the core with an Fe-P ratio of 9:1, the total mass of the core would be 155 kDa. Combined with the apo-mass, a total mass of 655 kDa is obtained for the iron-loaded molecule. It would be very interesting if distribution mapping could be performed also for other elements and under better resolution conditions. Particularly the possibility to measure the iron content per molecule is relevant because one of the main tasks of ferritin is to store iron in the cell in a less toxic fashion. For the quantification of iron it may be necessary to exchange chromium as element of the support film for another, because the Cr $L_{2,3}$ -edge at 574 eV disturbs the iron pre-edge region.

Possibilities for improvement

Three aspects are generally considered when results of electron spectroscopic imaging are to be improved: resolution, sensitivity and mass-loss.

- (1) In the case of digital image acquisition, the spatial resolution is affected mainly by chromatic aberration, spherical aberration, specimen drift, sample distance (controlled by the magnification) and the degree of smoothing by the SIT TV-camera. The aberrations depend on the objective lens aperture (see eqs. (2.4) and (2.5)) and the chromatic aberration, in addition, depends on the slit width. In [Berger93], the optimization of the instrumental parameters of energy-filtering microscopes was investigated theoretically for the purpose of elemental imaging. Using this theory, in [Lavergne94] it was shown that improvements for the EM 902 are also possible with respect to the currently used imaging parameters. It is expected, however, that suppression of the chromatic aberration by the choice of a smaller slit width entails the

ESI as a tool for the analysis of structure and composition of isolated ferritin

problem of having insufficient electron gun brightness to produce images. Still, it is considered worthwhile to investigate in more detail whether the imaging conditions can be improved.

Specimen drift during the acquisition period is another factor menacing the localization sharpness. The accuracy with which the specimen drift can be corrected is one pixel. Reduction of the total duration of the acquisition through automatic attenuation filter and spectrometer control may give some improvement in the future.

The sample distance depends on the magnification. If electron microscopic resolution, specimen drift and the resolution degradation by the camera are simultaneously considered, the choice of 50,000x (1.5 nm sample distance) for the magnification is believed to be sufficient.

- (2) The sensitivity of the detection of elements depends on the amount of noise present in the data. The electron dose, which is the product of the electron flux through the specimen (illumination brightness) and the duration of irradiation, determines the number of electrons available for image formation and therefore directly influences the amount of noise. The illumination brightness used in the experiments was the maximum obtainable from the used tungsten hairpin electron source. A higher brightness can be obtained with LaB₆ or field emission gun sources [Reimer84]. Image integration over periods longer than the currently used period of 10 s. is possible. A drawback of all dose enhancing measures is the increased radiation damage to the specimen.

Another aspects that influences the amount of noise in the element distribution image is the analysis procedure. There is evidence that the formalism of correspondence analysis has a smaller noise amplifying effect on the calculation of distribution images, when compared to the more conventional approach used in this thesis [Gelsema94]. This issue needs more research in the future.

- (3) Radiation damage in the form of mass-loss reduces the quality of element specific images and introduces a bias when elements are quantified. The results collected in [Hall74, Lamvik87, Zierold88, Lamvik89a&b, Lamvik91] clearly indicate that the small proteinaceous particles in or on carbon or metal films suffer from mass-loss in relation to dose and specimen temperature in a rather direct way. This leads (at the same dose) to a different residual mass after an initial loss, when observed either at room temperature or at 130 K or at liquid helium temperature, where a minimal loss is noticed.

It is clear that under the conditions present in our instrument, without specimen cooling, this initial mass-loss has taken place, since the maximum available beam intensity had to be used to acquire the requested images. Although we monitored rather modest mean losses during the acquisition period, the initial element-specific losses (e.g. oxygen [Drechsler91]) may have been large. On the other hand, the mean loss may have been modest due to the presence of a rather firm contact between the proteinaceous material and the chromium film. Metal (titanium) films have been shown to provide, at

Chapter 11

ultra low liquid helium temperatures, better protection than carbon films [Lamvik87, Lamvik89a&b, Lamvik91], whereas in [Zierold88], judging by the darkfield intensity, an improved mass-loss stability of a carbon film on frozen-hydrated sections was reported.

Further improvements are also possible with better purity of the ferritin solution. When broken shells and ferritin subunits are removed, the contrast between the individual particles is expected to be better.

In conclusion:

- (1) The carbon distribution images as obtained by the application of an EFTEM acquisition protocol and image processing procedures demonstrated the proteinaceous structure of the ferritin-shell. The resultant images were significantly different from those acquired after a negative staining procedure. Because the preparation and acquisition conditions were not optimal, a final judgement of the described spectroscopic imaging technique should be postponed until the experimental conditions have been improved.
- (2) The proposed acquisition protocol and image-processing procedures which include the use of calibrated attenuation filters for a variety of purposes are successfully applied. These procedures allow us to determine carbon- and presumably also iron-distribution images in isolated ferritin particles, embedded in 2 nm thick chromium films. The reliability of these observations and calculations for structural and composition analysis was evaluated by a number of validity checks. The obtained average of 16,874 carbon atoms per ferritin shell explains about 50% of the mass of the ferritin shell.

Chapter 12. General conclusions and summary

The capability of the energy-filtering transmission electron microscope to produce electron spectroscopic image sequences has been used to compute quantitative element distributions in ultra-thinly sectioned specimens. Part I of this thesis describes the investigation of methodological aspects and the development of procedures for measuring concentration distributions of chemical elements. A protocol, integrating these procedures was developed. Part II treats the application of these procedures for the measurement of iron concentrations under biological conditions and the imaging of carbon in a model environment. The main conclusions of this thesis are the following.

- Quantitative chemical element distributions can be obtained from ultra-thin sections of biological material with the use of a commercially available energy-filtering electron microscope (Zeiss EM 902). The only adaptation necessary is the addition of an optical filter holder in front of the TV-camera. The resolution of the iron distribution images is close to the resolution of the conventional electron micrographs and in this sense the quantification procedure meets the expectations of an electron microscopist. The lower limit of quantification (dependent on many factors), in the case of iron, approaches values of 0.5 atoms/nm³. This makes the measurement setup suitable for use in pathology to study conditions of iron overload.
- For the visual interpretation of element distributions, it has been demonstrated that division of the net-intensity distribution by the integrated zero- and low-loss image contributions is necessary if the element distributions are used for purposes other than making the binary decision with respect to the presence or absence of element quantities.
- In liver sections of an idiopathic hemochromatosis patient, taken before and after phlebotomy, no difference in average organelle Fe-concentration could be measured before and after this treatment. Thus, the iron was removed from other compartments than those in the regions analyzed, indicating that the mobilization of iron from its stores is an organelle specific process.
- For the investigation of tissue parts obtained from subjects with iron overload, concentration measurement of iron assists in the in situ chemical characterization of iron containing compounds. In this way, regions containing ferritin could be discerned from regions consisting of degradation products of the molecule.
- The imaging of macromolecular structures, when attached to an extremely thin film (of e.g. 2 nm chromium), by their natural carbon content seems feasible. However, the instrumental conditions have to be improved and the preparation techniques must be more closely controlled before an indication of the obtainable final resolution can be determined.

Chapter 12

Central in the first part of this thesis is the quantification expression formulated by Egerton, eq. (3.2). This expression identifies a number of quantities that are to be obtained from an electron spectroscopic image sequence: the net-intensity image I_k and the integrated zero- and low-loss contributions I_T . This means that the microscope, instead of being a tool for visualization, has to be converted into an instrument for measurement. One of the main requirements, in order to be able to use a system for measurement, is that the measurement values produced by such a system are a faithful representation of the quantity to be measured. The system that is considered in this thesis is an energy filtering electron microscope, projecting its images onto a scintillator screen. The images are subsequently observed by a TV-camera, connected to an image processing system.

The TV-camera is required to measure intensity distributions of electrons within a selected energy-range, defined by the spectrometer slit width. In principle this is possible, although it was recognized that the TV-camera also acts as a source of distortion and, moreover, is unable to measure intensities over such a large dynamic range as encountered in the spectrum. This resulted in the addition of optical attenuation filters for two purposes: to cover the large intensity dynamic range and to measure the distortions of the camera. Furthermore, correction procedures were implemented to compensate for shading and the non-linear photometric response of the TV-camera. To enable the calculation of element distributions, sequences of energy-filtered images have to be obtained. Lateral specimen drift that generally occurs during the acquisition period also requires correction. All corrective steps, i.e., for shading, non-linearity and drift were tested and judged to be essential for quantification. The optical filters are effective for light attenuation. There is, however, some uncertainty about the behaviour of the scintillator screen with respect to the large electron irradiation differences.

Energy-filtered imaging in the electron microscope is basically a form of electron limited imaging, which means that the number of electrons composing the image is so small that the images are inherently noisy. To characterize the images statistically, the detector chain was investigated. The adoption of a simple model for the interaction of electrons with the scintillator screen and for the collection of photons by the camera sensor led to the derivation of a linear relation between average μ and variance σ^2 of the intensities recorded by the camera. This relation has also been established experimentally. A normal distribution $N(\mu, \sigma^2)$ was further assumed to describe the statistics of the acquired images, where μ and σ^2 may be different in each pixel. For the spectral characterization of image sequences, we confined our analysis to regions where the power-law model (eq. 5.1) is valid. The combination of the power-law with the statistical image description yielded a statistical model for the spectral background and formed the basis for solving the problem of background subtraction.

Using the described model, the theory of statistical parameter estimation led to the formulation of the problem of estimating the background parameters in terms of a non-linear weighted least squares problem. This problem was solved by the design of an efficient iterative algorithm. Application of the algorithm to the pre-edge subset of a spectroscopic

image sequence gives the requested background parameter values. These values are then used to extrapolate the model to the edge-region giving a background estimate which by subtraction from the integral edge intensity yields the net-intensity image. Application of the theory of statistical parameter estimation also enabled to give an indication of the precision of background estimates. This property was used to discriminate significant element contributions in the net-intensity images by thresholding of the corresponding SNR-images.

The calculation of a net-intensity image is only an intermediate step in the process of quantification. Division by the integrated zero- and low-loss image contributions, followed by calibration with the reference value obtained from a Bio-standard, results in quantitative element distribution images. The Bio-standard, present in the same section, with a reference concentration obtained from neutron activation, is measured with the same microscope system, operated under comparable conditions and using the same procedures as for the measurement of unknown concentrations. Two major advantages with respect to the robustness of this approach have been mentioned: effects of mass-loss by radiation damage are reduced and possible non-linearities in the detector chain are suppressed. A remaining problem is the variability of the element-loading of the Bio-standard. An alternative to enhance the reliability and flexibility of the use of such standards has been given in Chapter 9.

The functional range of the concentration measurement scale was investigated in Chapter 7 with a series of experiments. At the high end of the scale, a deviation from the assumed linear relationship between measured and actual amount was observed. Deviations from linearity increase with increasing values of the relative section thickness. At the low end of the scale, the noise masks low concentrations from detection. It was suggested that extension of the functional range of the scale may be possible by correction for plural scattering (improving the linearity) and the use of smoothing techniques to enhance the SNR of the image data, or by the use of alternative methods for background correction (correspondence analysis, MLS-fitting). It was indicated that the relative section thickness must be monitored for quantification. This currently forms a standard procedure to check the validity of the quantification process. Other checks that are performed are those for radiation damage, specimen drift and the general consistency of the data by the computation of ghost-images. It is stressed, that such validity checks are essential components of the process of quantification. The additional image acquisition effort to enable these checks is small.

The analysis of double sections of epon-embedded Fe-Chelex spheres, which also contain sectioning artefacts such as tears, clearly indicated that visual interpretation of net-intensity images is virtually impossible if anything more than the determination of the presence or absence of an element is attempted. The effectiveness of mass-thickness correction by division of the net-intensity image by the integrated zero- and low-loss images was clearly demonstrated. The conclusion is that even for the purpose of visual interpretation, it is necessary to correct for mass-effects.

Chapter 12

As an application of the developed measurement procedures, the storage of iron in structures within liver parenchymal cells of an idiopathic hemochromatosis patient was investigated. Particularly, the influence of phlebotomy of the patient on the iron content of these structures was studied. Comparison of the results of the iron concentration measurements, performed in 32 organelles before and 22 organelles after phlebotomy, could not demonstrate a significant difference between the two situations. The conclusion was drawn that apparently the iron was not removed from the regions analyzed after phlebotomy. The results are evidence for the organelle specific catabolization in response to the demand for iron. A better, e.g., zonal localization of the analysis regions in such studies was suggested as a means to confirm this conclusion. An effort to chemically characterize the iron containing structures on the basis of the local iron concentration was successful. However, probably due to volume effects, the iron-concentration histograms are complex, preventing a straightforward classification of the structures. The investigation of a possible relationship between the average organelle iron-loading and the morphology related parameters, object area and object contour ratio, did not yield any positive result.

In a second application, the capability of ESI as an imaging modality was investigated. Isolated ferritin particles, prepared on a 2 nm chromium film, were used as test objects to create carbon distribution images. The results of this experiment look promising. Nevertheless, both specimen preparation and image acquisition conditions can be improved. More experimentation is needed before a final conclusion about the usefulness of this technique for this purpose can be given.

References

- [Agar74] Agar, A.W., Alderson, R.H., Chescoe, D. (1974) Principles and practice of electron microscope operation: Practical methods in electron microscopy, ed. Glauert A.M., North-Holland publishing company, Amsterdam.
- [Ahn85] Ahn, C.C., Rez, P. (1985) Inner shell edge profiles in electron energy loss spectroscopy, *Ultramicroscopy* **17**, 105-116.
- [Alonso80] Alonso, M., Fin, E.J. (1980) Fundamental university physics; Vol III: quantum and statistical physics, Addison-Wesley, Reading, Massachusetts, pp. 33-38.
- [Alt90] Alt, E.R., Sternlieb, I., Goldfischer, S. (1990), The cytopathology of metal overload, *International review of experimental pathology* **31**, 165-188.
- [Andrews87] Andrews, S.C., Treffry, A., Harrison, P.M. (1987), Siderosomal ferritin, the missing link between ferritin and heamosiderin? *Biochem. J.* **245**, 439-446.
- [Andrews93] Andrews, S.B., Leapman, R.D. (1993) Biological scanning transmission electron microscopy, *Europ. J. Microscopy and analysis* **6**, 21-24.
- [Apkarian88] Apkarian, R.P., Joy, D.C. (1988) Analysis of metal films suitable for high-resolution SE-I microscopy. In: *Microbeam analysis*, ed. Newbury, D.E., San Francisco Press, San Francisco, CA., pp. 459-462.
- [Apkarian94] Apkarian, R.P. (1994) Analysis of high quality monatomic chromium films used in biological high resolution scanning electron microscopy, *Scanning Microsc.* **8**, 289-301.
- [Auerhammer89] Auerhammer, J., Rez, P. & Hofer, F. (1989) A comparison of theoretical and experimental L and M cross sections. *Ultramicroscopy* **30**, 365-370.
- [Ballard82] Ballard, D.H., Brown, C.M. (1982) *Computer vision*, Prentice-Hall Inc., New Jersey, pp. 66-70.
- [Batchelor85] Batchelor, B.G. (1985) Television techniques. In: *Automated Visual Inspection*, eds. Batchelor, B.G., Hill, D.A. & Hodgson, D.C., I.F.S. Ltd, UK, pp. 215-253.
- [Berger93] Berger, A., Kohl, H. (1993) Optimum imaging parameters for elemental mapping in an energy filtering transmission electron microscope, *Optik* **92-4**, 175-193.
- [Bevington69] Bevington, P.R. (1969) *Data reduction and error analysis for the physical sciences*, McGraw-Hill, New York, pp. 235-240.

- [Bih88] Bihl, J., Rilk, A., Benner, G. (1988) Angle of acceptance and energy resolution in the imaging electron energy-loss spectrometer of the EM 902, *Int. Phys. Conf. Ser. No. 93: Vol. 1, Chapter 1*, 159-160.
- [Bonnet88a] Bonnet, N., Colliex, C., Mory, C. & Tence, M. (1988) Developments in processing image sequences for elemental mapping, *Scanning Microsc. Suppl.* **2**, 351-364.
- [Bonnet88b] Bonnet, N., Jean-Claude Liehn, J-C. (1988) Image registration in electron microscopy: Application of a robust method, *J. Electron Microsc. Tech.* **10**, 27-33.
- [Bonnet92a] Bonnet, N., Simova, E., Lebonvallet, S., Kaplan, H. (1992) New applications of multivariate statistical analysis in spectroscopy and microscopy, *Ultramicroscopy* **40**, 1-11.
- [Bonnet92b] Bonnet, N., Trebbia P. (1992) Multi-dimensional data analysis and processing in electron-induced microanalysis, *Scanning Microsc. Suppl.* **6**, 163-177.
- [Bonnet92c] Bonnet, N., Michel, J., Wagner, D., Balossier, G. (1992) Optimization of digital filters for the detection of trace elements in electron energy-loss spectroscopy I: Theory and simulations, *Ultramicroscopy* **41**, 105-114.
- [Bos82] van den Bos, A. (1982) Parameter Estimation. *Handbook of Measurement Science, Vol. 1* (ed. Sydenham, P.H., John Wiley & Sons Ltd., New York.), pp. 331-377.
- [Bothwell79] Bothwell, T.H., Charlton, R.W., Cook, J.D., Finch, C.A. (1979) *Iron metabolism in man*, Blackwell Science Publishers, London.
- [Bothwell88] Bothwell, T.H., Charlton, R.W. (1988) Historical overview of hemochromatosis, *Ann. N. Y. Acad. Sci.* **526**, 1-10.
- [Botton94] Botton, G. L'Esperance, G. (1994) Development, quantitative performance and applications of a parallel electron energy-loss spectrum imaging system, *J. Microsc.* **173**, 9-25.
- [Bradford76] Bradford, M.N. (1976) A rapid and sensitive method for the quantitation of microgram quantities of protein utilizing the principle of protein-dye binding, *Anal. Biochem.* **72**, 245-254.
- [Bruijn81] De Bruijn, W.C., Steijn-Myagkaya, G.M. (1981) In situ X-ray microanalysis of ferritin, *Beitr. Elektronenmikroskop. Direktabb. Oberfl.* **14**, 423-426.
- [Bruijn85a] De Bruijn, W.C. (1985) Integration of X-ray microanalysis and morphometry of biological material, *Scan. Electron Microsc. II*, 697-712.

References

- [Bruijn85b] De Bruijn, W.C., Cleton-Soeteman, M.I. (1985) Application of Chelex standard beads in integrated morphometrical and X-ray microanalysis, *Scan. Electron Microsc.* **II**, 715-729.
- [Bruijn91] De Bruijn, W.C., Ketelaars, D., Gelsema, E.S., Sorber, C.W.J. (1991) Comparison of the simplex method with several other methods for background-fitting for electron energy-loss spectral quantification of biological materials, *Microsc. Microanal. Microstruct.* **2**, 281-291.
- [Bruijn93] De Bruijn W.C., Sorber, C.W.J., Gelsema, E.S., Beckers, A.L.D., Jongkind, J.F. (1993) Energy-filtering transmission electron microscopy of biological specimens, *Scan. Electron Microsc.* **7** (2), 693-709.
- [Castaing62] Castaing, R., Henry, L. (1962) Filtrage magnétique des vitesses en microscopie électronique, *C.R. Acad. Sci. Paris* **255**, 76-78.
- [Cattermole91] Cattermole, D., Henderson, R. (1991) An electronic image drift compensator for electron microscopy, *Ultramicroscopy* **35**, 55-57.
- [Chapman89] Chapman, J.N., Craven, A.J., Scott, C.P. (1989) Electron detection in the analytical electron microscope, *Ultramicroscopy* **28**, 108-117.
- [Cleton86] Cleton, M.I., Roelofs, J.M., Blok-Van Hoek, C.J.G., De Bruijn, W.C. (1986) Integrated image and X-ray microanalysis of hepatic lysosomes in idiopathic hemochromatosis before and after treatment by phlebotomy, *Scan. Electron Microsc.* **III**, 999-1006.
- [Cleton88] Cleton, M.I., De Bruijn, W.C., Blokland, W.T.M., Marx, J.J.M., Roelofs, J.M., Rademakers, L.H.P.M. (1988) Iron content and acid phosphatase activity in hepatic parenchymal lysosomes of patients with hemochromatosis before and after phlebotomy treatment, *Ultrastruct. Pathol.* **12**, 161-174.
- [Cleton89] Cleton, M.I., Mostert, L.J., Sorber, C.W.J., de Jong, A.A.W., de Jeu-Jaspers C.M.H., De Bruijn, W.C. (1989) Effect of Phlebotomy on the ferritin iron content in the rat liver as determined morphometrically with the use of electron energy-loss spectroscopy, *Cell Tissue Res.* **256**, 601-605.
- [Colliex81] Colliex, C., Jeanguillaume, C., Trebbia, P. (1981) Quantitative local microanalysis with EELS. In: *Microprobe Analysis of Biological Systems*, eds. Hutchinson, T.E., Somlyo, A.P., Academic Press, New York, pp. 251-271.
- [Colliex84] Colliex, C., Jeanguillaume, C., Mory, C. (1984) Unconventional modes for STEM imaging of biological structures, *J. Ultrastr. Res.* **88**, 177-206.

- [Colliex85] Colliex, C. (1985) An illustrated review of various factors governing the high spatial resolution capabilities in EELS microanalysis, *Ultramicroscopy* **18**, 131-150.
- [Colliex86] Colliex, C., Manoubi, T., Krivanek, O.L. (1986) EELS in the electron microscope: A review of present trends, *J. Electron Microsc.* **35**, 307-313.
- [Crichton92] Crichton, R.R., Ward, R.J. (1992) Iron metabolism - new perspectives in view, *Biochemistry* **31** (46), 11255-11264.
- [Drechsler91] Drechsler, M., Cantow, H-J (1991) EELS data acquisition and display for the Zeiss CEM902 based on Lotus 1-2-3^R: application examples from a biological system and inorganic transition metal compounds. *J. Microsc.* **161**, 61-76.
- [Drysdale77] Drysdale, J.W. (1977) Ferritin phenotypes: structure and metabolism. In: *Iron metabolism*, ed. Jacobs, A., Ciba Foundation Symposium 51 Amsterdam, Elsevier, pp. 41-57.
- [Egerton80] Egerton, R.F. (1980) Instrumentation and software for energy-loss microanalysis, *Scan. Electron Microsc.* **1**, 41-52.
- [Egerton86] Egerton, R.F. (1986) *Electron Energy-Loss Spectroscopy in the Electron Microscope*, Plenum Press, New York.
- [Egerton87] Egerton, R.F., Cheng, S.C. (1987) Measurement of local thickness by electron energy-loss spectrometry, *Ultramicroscopy* **21**, 231-244.
- [Egerton89] Egerton, R.F. (1989) Quantitative analysis of electron energy-loss spectra, *Ultramicroscopy* **28**, 215-225.
- [Eijk93] van Eijk, H.G., van der Heul, C. (1993) IJzerstofwisseling, *Tijdschr. NVKC* **18**, 3-17.
- [Engel84] Engel, A., Reichelt, R. (1984) Imaging of biological structures with the scanning transmission electron microscope, *J. Ultrastr. Res.* **88**, 105-120.
- [Gelder93] van Gelder, W., Siersema, P.D., Voogd, A., de Jeu-Jaspars, N.C.M., van Eijk, H.G., Koster, J.F., de Rooy, F.W.M., Wilson, J.H.P. (1993) The effect of desferrioxamine on iron metabolism and lipid peroxidation in hepatocytes of C57BL/10 mice in experimental uroporphyrin, *Biochem. Pharmacol.* **46**, 221-228.
- [Gelsema92] Gelsema, E.S., Beckers, A.L.D., Sorber, C.W.J., De Bruijn W.C. (1992) Quantification procedures for electron energy-loss spectroscopy and imaging: the use of correspondence analysis for element detection, *J. Microsc.* **166**, 287-296.

References

- [Gelsema94] Gelsema, E.S., Beckers, A.L.D., De Bruijn, W.C. (1994) Optimal conditions for the use of correspondence analysis for element determination in EELS images, *J. Microsc.* **174**, 161-169.
- [Gonzalez87] Gonzalez, R.C., Wintz, P. (1987) *Digital image processing*, Addison-Wesley, Reading, Massachusetts, pp. 221-246.
- [Granick46] Granick, S. (1946) Ferritin: its properties and significance for iron metabolism, *Chem. Rev.* **38**, 379-403.
- [Hall74] Hall, T.A., Gupta, B.L. (1974) Beam-induced loss of organic mass under electron-microprobe conditions, *J. Microsc.* **100**, 177-188.
- [Hannequin88] Hannequin, P., Bonnet, N. (1988) Application of multivariate statistical analysis to energetic image series, *Optik* **81**, 6-11.
- [Harris78] Harris DC (1978) Ion-exchange between ferritin and transferrin in vitro, *Biochemistry* **17**, 3071-3078.
- [Harrison77] Harrison, P.M. (1977) Ferritin: an iron storage molecule, *Semin. Hematol.* **14**, 55-70.
- [Harrison91] Harrison, P.M., Andrews, S.C., Artymiuk, P.J., Ford, G.C., Guest, J.R., Hurzmann, J., Lawson, D.M., Livingstone, J.C., Smith, J.M.A., Treffry, A., Yewdall, S.J. (1991) Probing structure-function relations in ferritin and bacterioferritin, *Adv. inorg. Chem.* **36**, 449-486.
- [Hayat89] Hayat, M.A. (1989) *Principles and techniques of electron microscopy*, 3rd ed., McMillan Press Ltd, Hampshire and London, pp. 328-376.
- [Heel92] Van Heel, M., Schatz, M., Orlova, E. (1992) Correlation functions revisited, *Ultramicroscopy* **46**, 307-316.
- [Henkelman74] Henkelman, R.M., Ottensmeyer, F.P. (1974) An energy filter for biological electron microscopy, *J. Microsc.* **102**, 79-94.
- [Hentze87] Hentze, M.W., Caughman, S.W., Roualt, T.A., Barriocanal, J.G., Dancis, A., Harford, J.B., Klausner, R.D. (1987) Identification of the iron-responsive element for the translational regulation of human ferritin mRNA, *Science* **238**, 1570-1573.
- [Hider90] Hider, R.C., Singh, S., Porter, J.B., Huehns, E.R. (1990) The development of hydroxypyridin-4-ones as orally active iron chelators, *Ann. N. Y. Acad. Sci.* **612**, 327-338.

- [Hofer91] Hofer, F. (1991) Determination of inner-shell cross-sections for EELS quantification, *Microsc. Microanal. Microstruct.* **2**, 215-230.
- [Horne74] Horne, R.W., Pasquali-Ronchetti, I. (1974) A negative staining-carbon film technique for studying viruses in the electron microscope. I Preparation procedures for examining icosahedral and filamentous viruses, *J. Ultrastr. Res.* **47**, 361-373.
- [Iancu83] Iancu, T.C. (1983) Iron overload, *Molec. Aspects Med.* **6**, 1-100.
- [Jacobs74] Jacobs, A., Worwood, M. (1974) *Iron in biochemistry*, Academic Press, London.
- [Jeanguillaume78] Jeanguillaume, C., Trebbia, P., Colliex, C. (1978) About the use of EELS for chemical mapping of thin foils with high spatial resolution, *Ultramicroscopy* **3**, 237-247.
- [Kate90a] Ten Kate T.K., van Balen, R., Smeulders A.W.M., Groen F.C.A., den Boer G.A. (1990) Scilaim: A multilevel interactive image processing environment, *Pattern Recognition Lett.* **11**, 429-441.
- [Kate90b] Ten Kate T.K. (1990) *TV Microscopical image analysis for accurate DNA quantification in pathology*, PhD-thesis, Amsterdam, The Netherlands.
- [Kernigan78] Kernigan, B.W., Ritchie, D.M. (1978), *The C programming language*, Prentice-Hall, London.
- [Kleinschmidt59] Kleinschmidt, V.A., Zahn, R.K. (1959) Über Desoxyribonucleinsäure-Molekeln in Protein Mischfilmen, *Z. Naturforsch.* **14b**, 770-778.
- [Kontoghiorghes85] Kontoghiorghes, G.J. (1985) New orally active iron chelators, *Lancet* **ii**, 817.
- [Kortje92] Kortje, K.-H. Kortje, D. (1992) The application of electron spectroscopic imaging for quantification of the area fractions of calcium-containing precipitates in nervous tissue, *J. Microsc.* **166**, 343-358.
- [Kortje94] Kortje, K.-H. (1994) Image-EELS: simultaneous recording of multiple electron energy-loss spectra from series of electron spectroscopic images, *J. Microsc.* **174**, 149-159.
- [Krivanek91a] Krivanek, O.L., Gubbens, A.J., Dellby, N. (1991) Developments in EELS instrumentation for spectroscopy and imaging, *Microsc. Microanal. Microstruct.* **2**, 315-332.
- [Krivanek91b] Krivanek, O.L., Mory, C., Tencé, M., Colliex, C. (1991) EELS quantification near the single-atom detection level. *Microsc. Microanal. Microstruct.* **2**, 257-267.

References

- [Krivanek93] Krivanek, O.L., Mooney, P.E. (1993) Applications of slow-scan CCD cameras in transmission electron microscopy, *Ultramicroscopy* **49**, 95-108.
- [Lamvik87] Lamvik, M.K., Kopf, D.A., Davilla, S.D. (1987) Mass loss rate in collodion is greatly reduced at liquid helium temperature, *J. Microsc.* **148**, 211-217.
- [Lamvik89a] Lamvik, M.K., Davilla, S.D., Klatt, L.L. (1989) Substrate properties affect the mass loss rate in collodion at liquid helium temperature, *Ultramicroscopy* **27**, 241-250.
- [Lamvik89b] Lamvik, M.K., Davilla, S.D., Tuttle, J. (1989) Properties of substrates for low temperature quantitative microscopy and microanalysis, *Scanning Microsc. Suppl.* **3**, 271-276.
- [Lamvik91] Lamvik, M.K., Magid, A.D., Davilla, S.D., Córdova, L. (1991) Temperature directly affects the rate of irradiation induced mass loss from phosphatidylcholine multilayers, *Ultramicroscopy* **47**, 1-6.
- [Langmore78] Langmore, J.P. (1978) Electron microscopy of atoms. In: Principles and techniques of electron microscopy. Vol. 9. Biological applications. ed. Hayat M.A., van Norstrand Reinhold Cy., New York, pp. 1-63.
- [Lavergne94] Lavergne, J.-L., Foa, C., Bongrand, P., Seux, D., Martin, J.-M. (1994) Application of recording and processing of energy-filtered image sequences for the elemental mapping of biological specimens: Imaging-Spectrum, *J. Microsc.* **174**, 195-206.
- [Leapman80] Leapman, R.D., Rez, P. & Mayers, D.F. (1980) K, L, and M shell generalized oscillator strengths and ionization cross-sections for fast electron collisions, *J. Chem. Phys.* **72**, 1232-1243.
- [Leapman88] Leapman, R.D. & Ornberg, R.L. (1988) Quantitative electron energy loss spectroscopy in biology, *Ultramicroscopy* **24**, 251-268.
- [Leapman91] Leapman, R.D., Hunt, J.A. (1991) Comparison of detection limits for EELS and EDXS, *Microsc. Microanal. Microstruct.* **2**, 231-244.
- [Leapman92a] Leapman, R.D., Andrews, S.B. (1992) Characterisation of biological macromolecules by combined mass mapping and electron energy-loss spectroscopy, *J. Microsc.* **165**, 225-238.
- [Leapman92b] Leapman, R.D., Hunt, J.A. (1992) Compositional imaging with electron energy loss spectroscopy, *Microscopy: The key research tool* **22**, 39-49.
- [Leapman93] Leapman, R.D., Hunt, J.A., Buchanan, R.A., Andrews, S.B. (1993) Measurements of low calcium concentrations in cryosectioned cells by parallel-EELS mapping, *Ultramicroscopy* **49**, 225-234.

- [Leapman94] Leapman, R.D., Sun, S.Q., Hunt, J.A., Andrews, S.B. (1994) Biological electron energy-loss spectroscopy in the field-emission STEM, *Scanning Microsc. Suppl.* **8**, in press.
- [Massover93] Massover, W.H. (1993) Ultrastructure of ferritin and apoferritin: A review, *Micron* **24** (4), 389-437.
- [Meyer79] Meyer, F. (1979) Iterative image transformations for an automatic screening of cervical smears, *J. Histochem. Cytochem.* **27**, 128-135.
- [Michel93] Michel, J., Bonnet, N., Wagner, D., Balossier, G., Bonhomme, P. (1993) Optimization of digital filters for the detection of trace elements in electron energy-loss spectroscopy II: Experiments, *Ultramicroscopy* **48**, 121-132.
- [Mostert89] Mostert, L., Cleton, M.I., De Bruijn, W.C., Koster, J.F., van Eijk, H.G. (1989) Studies on ferritin in rat liver and spleen during repeated phlebotomy, *Int. J. Biochem.* **21** (1), 39-47.
- [O'Connell86] O'Connell, M.J., Halliwell, B., Moorhouse, C.P., Aruoma, A.I., Baum, H., Peters, T.J. (1986) Formation of hydroxyl radicals in the presence of ferritin and heamosiderin, *Biochem. J.* **234**, 727-731.
- [Oppenheim83] Oppenheim, A.V., Willsky A.S., Young, I.T. (1983) *Signals and systems*, Prentice Hall, London, pp. 519.
- [Ottensmeyer84] Ottensmeyer, F.P. (1984) Electron spectroscopic imaging: Parallel energy filtering and microanalysis in the fixed-beam electron microscope, *J. Ultrastruct. Res.* **88**, 121-134.
- [Peters86] Peters, K-R. (1986) Rationale for the application of thin continuous metal films in high magnification electron microscopy, *J. Microsc.* **142**, 25-34.
- [Phillipp94] Phillipp, F., Hörschen, R., Möbus, G., Osaki, M., Rühle M. (1994) The stuttgart atomic resolution high-voltage electron microscope: approaching 1 Ångström point-to-point resolution, *Jeol news* **31E-1**, 2-6.
- [Porter89] Porter, J.B., Huehns, E.R., Hider, R.C. (1989) The development of iron chelating drugs, *Baillieres. Clin. Haematol.* **2** (2), 257-292.
- [Pun84] Pun, T., Ellis, J.R. & Eden M. (1984) Optimized acquisition parameters and statistical detection limit in quantitative EELS, *J. Microsc.* **135**, 295-316.
- [Pun85] Pun, T., Ellis, J.R., Eden, E. (1985) Weighted least squares estimation of background in EELS imaging, *J. Microsc.* **137**, 93-100.

References

- [Puymbroeck92] Van Puymbroeck, J., Jacob, W. & Van Espen, P. (1992) Methodology for spectrum evaluation in quantitative electron energy-loss spectrometry using the Zeiss CEM 902, *J. Microsc.* **166**, 273-286.
- [Reimer84] Reimer, L. (1984) *Transmission electron microscopy*, Springer-Verlag, Berlin.
- [Reimer88] Reimer, L., Fromm, I., Rennekamp, R. (1988) Operation modes of electron spectroscopic imaging and electron energy-loss spectroscopy in a transmission electron microscope, *Ultramicroscopy* **24**, 339-354.
- [Reimer91] Reimer, L. (1991) Energy filtering transmission electron microscopy. In: *Advances in electronics and electron physics*. Vol **81**., Academic Press Inc., London, New York, pp. 43-126.
- [Renswoude82] van Renswoude, J., Bridges, K.R., Harford, J.B., Klausner, R.D. (1982) Receptor-mediated endocytosis of transferrin and the uptake of Fe in K562 cells: identification of a nonlysosomal acidic compartment, *Proc. Natl. Acad. Sci. USA.* **79** (20), 6186-6190.
- [Richter78] Richter, G.W. (1978) The iron-loaded cell: The cytopathology of iron storage, *Am. J. Pathol.* **91**, 363-396.
- [Richter84] Richter, G.W. (1984) Studies of iron overload, *Lab. Invest.* **50**, 26-35.
- [Ringeling90] Ringeling, P.L., Cleton, M.I., Huijskes-Heins, M.I.E., Seip, J.E., De Bruijn, W.C., van Eijk, H.G. (1990) Analysis of iron-containing compounds in different compartments of the rat liver after iron loading, *Bio Metals* **3**, 176-182.
- [Ringeling91] Ringeling, P.L. (1991) Rat liver ferritin biochemical and microanalytical aspects, PhD-thesis, Rotterdam, The Netherlands.
- [Roß-Meßemer93] Roß-Meßemer, M. (1993) Personal communication.
- [Scheuer77] Scheuer, P.J. (1977) *Liver biopsy interpretation* 2nd ed., Ballière, Tindall and Cassel, London.
- [Shuman85] Shuman, H., Kruit, P. (1985) Quantitative data processing of parallel recorded electron energy-loss spectra with low signal to background, *Rev. Sci. Instrum.* **56** (2), 231-239.
- [Shuman86] Shuman, H., Chang, C.-F., Somlyo, A.P. (1986) Elemental imaging and resolution in energy-filtered conventional electron microscopy, *Ultramicroscopy* **19**, 121-134.
- [Shuman87] Shuman, H., Somlyo, A.P. (1987) Electron energy-loss analysis of near-trace-element concentrations of calcium, *Ultramicroscopy* **21**, 23-32.

[Simon76] Simon, M., Bourel, M., Fauchet, R., Genetet, B. (1976) Association of HLA-A3 and HLA-B14 antigens with idiopathic hemochromatosis, *Gut* **17**, 332-334.

[Sindram&Cleton86] Sindram J.W. and Cleton-Soeteman, M.I. (1986) The human liver in iron overload, PhD-thesis, Utrecht, The Netherlands.

[Sorber90a] Sorber, C.W.J., de Jong A.A.W., den Breejen, N.J., De Bruijn, W.C. (1990) Quantitative energy-filtered image analysis in cytochemistry. I. Morphometric analysis of contrast-related images, *Ultramicroscopy* **32**, 55-68.

[Sorber90b] Sorber, C.W.J., van Dort, J.B., Ringeling, P.C., Cleton-Soeteman, M.I., De Bruijn, W.C. (1990) Quantitative energy-filtered image analysis in cytochemistry. II. Morphometric analysis of element-distribution images, *Ultramicroscopy* **32**, 69-79.

[Sorber91a] Sorber, C.W.J., Ketelaars, G.A.M., Gelsema, E.S., Jongkind, F., De Bruijn, W.C. (1991) Quantitative analysis of electron energy-loss spectra from ultrathin-sectioned biological material. I. Optimization of the background-fit with the use of Bio-standards, *J. Microsc.* **162**, 23-42.

[Sorber91b] Sorber, C.W.J., Ketelaars, G.A.M., Gelsema, E.S., Jongkind, J.F., De Bruijn W.C. (1991) Quantitative analysis of electron energy-loss spectra from ultrathin-sectioned biological material. II. The application of Bio-standards for quantitative analysis, *J. Microsc.* **162**, 43-54.

[Sorber93] Sorber, W.C. (1993) Analysis of electron energy-loss spectra and images, PhD-thesis, Rotterdam, The Netherlands.

[Stearns94] Stearns, Rebecca C., Marshall Katler and Godleski, John J. (1994) Contribution of osmium tetroxide to the image quality and detectability of iron in cells studied by electron spectroscopic imaging and electron energy-loss spectroscopy, *Microsc. Res. Tech.* **28**, 155-163.

[Stephens80] Stephens, A.P. (1980) Quantitative microanalysis by electron energy-loss spectroscopy: two corrections, *Ultramicroscopy* **5**, 343-349.

[Tang94] Tang, Z., Ho, R., Xu, Z., Shao, Z., Somlyo, P. (1994) A high-sensitivity CCD system for parallel electron energy-loss spectroscopy (CCD for EELS), *J. Microsc.* **175**, 100-107.

[Tenailleau92] Tenailleau, H., Martin, J.M., (1992) A new background subtraction for low-energy EELS core edges, *J. Microsc.* **166**, 297-306.

[Trebba90a] Trebbia, P., Bonnet, N. (1990) EELS elemental mapping with unconventional methods I. Theoretical basis: image analysis with multivariate statistics and entropy concepts, *Ultramicroscopy* **34**, 165-178.

References

- [Trebba90b] Trebbia, P., Mory, C. (1990) EELS elemental mapping with unconventional methods II. Applications to biological specimens, *Ultramicroscopy* **34**, 179-203.
- [Tsay90] Tsay, T., Inman, R., Wray, B., Herman, B., Jacobson, K. (1990) Characterization of low-light-level cameras for digitized video microscopy, *J. Microsc.* **160**, 141-159.
- [Unser87] Unser, M., Ellis, J.R., Pun, T., Eden, M. (1987) Optimal background estimation in EELS. *J. Microsc.* **145**, 245-256.
- [Ward92] Ward, R.J., Ramsey, M.H., Dickson, D.P.E., Florence, A., Crichton, R.R., Peters, T.J., Mann, S. (1992) Chemical and structural characterisation of iron cores of haemosiderins isolated from different sources, *Eur. J. Biochem.* **209**, 847-850.
- [Xhoffer93] Xhoffer, C. (1993) Chemical characterization of individual particles by electron probe X-ray microanalysis and electron energy-loss spectrometry, PhD-thesis, Antwerp, Belgium.
- [Zaluzec85] Zaluzec, N.J. (1985), Digital filters for application to data analysis in electron energy-loss spectrometry, *Ultramicroscopy* **18**, 185-190.
- [Zeiss] Zeiss, Computer-controlled Transmission Electron Microscope CEM 902 Operating Instructions, Carl Zeiss, Oberkochen, Germany.
- [Zhenghzu93] Zhengzhu, J., Nilsson, B.O. (1993) Analysis of heavy metals in mouse uterine secretion by X-ray microanalysis, *Scan. Electron Microsc.* **7** (2), 719-723.
- [Zierold88] Zierold, K. (1988) X-ray microanalysis of freeze-dried and frozen-hydrated cryosections, *J. Electr. Microsc. Techn.* **9**, 65-82.

Publications

This thesis is based on the following scientific publications:

Beckers, A.L.D., Gelsema, E.S., de Bruijn W.C. (1993) An efficient method for calculating the least squares background fit in electron energy-loss spectroscopy, *J. Microsc.* **171**, 87-92.

Beckers, A.L.D., de Bruijn, W.C., Gelsema, E.S., Cleton-Soeteman, M.I., van Eijk, H.G. (1994) Quantitative electron spectroscopic imaging in bio-medicine: methods for image acquisition, correction and analysis, *J. Microsc.* **174**, 171-182.

Beckers, A.L.D., de Bruijn, W.C., Jongkind, J.F., Cleton-Soeteman, M.I., Apkarian, R.P., Gelsema E.S. (1994) Energy-filtering transmission microscopy as a tool for structural and compositional analysis of isolated ferritin particles, *Scanning Microsc. Suppl.* **8**, 261-275.

Other publications related to this thesis:

De Bruijn, W.C., Sorber, C.W.J., Gelsema, E.S., Beckers, A.L.D., Jongkind J.F. (1992) Energy-filtering transmission electron microscopy in biology, *Beitr. Elektronenmikroskop. Direktabb. Oberfl.* **25**, 387-392.

De Bruijn, W.C., Sorber, C.W.J., Trommelen-Ketelaars, G.A.M., Jongkind, J.F., Beckers, A.L.D., Gelsema E.S. (1993) Electron energy-loss spectroscopy and electron probe X-ray microanalysis of biological material: A comparative quantitative analysis of electron microscopical images, in: *X-ray Microanalysis in Biology: Experimental Techniques and Applications*, eds. Sigee, D.C., Morgan, A.J., Sumner, A.T., Warley, A., pp. 81-98.

De Bruijn, W.C., Sorber, C.W.J., Gelsema, E.S., Beckers, A.L.D., Jongkind, J.F. (1993) Energy-filtering transmission electron microscopy of biological specimens, *Scan. Microsc.* **7**, 693-709.

Gelsema, E.S., Beckers, A.L.D., de Bruijn, W.C. (1994) Optimality conditions for the use of correspondence analysis for element determination in EELS images, *J. Microsc.* **174**, 161-169.

Gelsema, E.S., Beckers, A.L.D., Sorber, C.W.J., de Bruijn W.C. (1992) Correspondence analysis for quantification in electron energy loss spectroscopy and imaging, *Meth. Inf. Med.* **31**, 29-35.

Gelsema, E.S., Beckers, A.L.D., Sorber, C.W.J., de Bruijn W.C. (1992) Quantification procedures for electron energy-loss spectroscopy and imaging: the use of correspondence analysis for element determination, *J. Microsc.* **166**, 287-296.

Gelsema, E.S., Beckers A.L.D. (1992) An application of correspondence analysis for the processing of image sequences, ICPR 1992 Den Haag, 356-359.

Sorber, Lianne, Bonnet, Noel, Gelsema, Edzard, Jongkind, Hans, Beckers, Guus, de Bruijn, Wim (1992) Multivariate statistical analysis as a tool for the analysis of EELS-images, Beitr. Elektronenmikroskop. Direktabb. Oberfl. **25**, 393-398.

Other scientific publications:

Beckers, A.L.D., Dorst, L., Young, I.T. (1985) The Choice of Filter Parameters for Non-Linear Grey-Value Image Processing. In: Architectures and Algorithms for Digital Image Processing, SPIE Vol. 596, ed. Duff, M., Cannes, France, pp. 120-128.

Young, Ian T., Beckers, Guus L., Dorst, Leo, Boerman, Annelies, (1986) Choosing Filter Parameters for Non-Linear Image Filtering. In: Pattern Recognition in Practice II, eds., Gelsema, E.S., Kanal, L.N., Elseviers Science Publishers, pp. 5-15.

Van Vliet, L.J., Young, I.T., Beckers, A.L.D. (1988) An edge detection model based on non-linear laplace filtering. In: Pattern Recognition and Artificial Intelligence, eds. Gelsema, E.S., Kanal, L.N., Elseviers Science Publishers, pp. 63-73.

Van Vliet, Lucas J., Young, Ian T., Beckers, Guus L. (1989) A Nonlinear Laplace Operator as Edge Detector in Noisy Images, Comput. Vision, Graphics, Image Process. **45**, 167-195.

Beckers, A.L.D., Smeulders, A.W.M. (1989) A Comment on "A Note on 'Distance Transformations in Digital Images'", Comput. Vision, Graphics, Image Process. **47**, 89-91.

Beckers, A.L.D., Smeulders, A.W.M. (1990) The probability of a random straight line in two and three dimensions, Pattern Recognition Lett. **11**, 233-240.

Beckers, A.L.D., Smeulders, A.W.M. (1992) Optimization of Length Measurement and Pseudo-Euclidean Distance Transformations in Three Dimensions, Comput. Vision, Graphics, Image Process.: Image Understanding **55**, 296-306.

Abstracts

A.W.M. Smeulders and A.L.D. Beckers, Accurate image measurement methods (applied to 3D length and distance measurements), 1st International Conference on Confocal Microscopy and 2nd International Conference on 3-D Image Processing in Microscopy, March 15-17, 1989.

A.L.D. Beckers and A.W.M. Smeulders, 3D Length Measurements and Topographical Consequences. Symposium on 3D Image Processing and Visualisation, Utrecht, The Netherlands, April 18-19, 1990, Foundation for Computer Vision Research Utrecht, The Netherlands.

C.W.J. Sorber, G.A.M. Ketelaars, A.L.D. Beckers, W.C. de Bruijn, Quantitative EELS analysis of images of biological materials, EMAS '91 2nd European Workshop on modern developments and applications in microbeam analysis, Dubrovnik, Yugoslavia, May 13-17, 1991.

Concentration measurements in EELS images of biological materials.

I. Prerequisites for the images and spectra, C.W.J. Sorber, G.A.M. Ketelaars, A.L.D. Beckers, L.C.J. Timmermans, W.C. De Bruijn and E.S. Gelsema

II. Experiments towards the image acquisition procedure, L.C.J. Timmermans, C.W.J. Sorber, G.A.M. Ketelaars, A.L.D. Beckers, W.C. De Bruijn and E.S. Gelsema

III. Optimization of analytical procedures, A.L.D. Beckers, C.W.J. Sorber, G.A.M. Ketelaars, L.C.J. Timmermans, W.C. De Bruijn and E.S. Gelsema, Third European Workshop on Electron Spectroscopic Imaging and Analysis Techniques, Martinsried, Germany, June 27-28, 1991.

A.L.D. Beckers, W.C. de Bruijn, E.S. Gelsema, The acquisition and processing of electron spectroscopic images, Fourth European Workshop on Electron Spectroscopic Imaging, Diffraction and Analysis Techniques, Münster, Germany, June 3-4, 1993.

E.S. Gelsema, A.L.D. Beckers, C.W.J. Sorber, W.C. de Bruijn, Further investigation of the formalism of correspondence analysis as a method for the quantitative analysis of energy filtered image sequences, 4th European workshop on electron spectroscopic imaging, diffraction and analysis techniques, Münster, Germany, June 3-4, 1993.

W.C. de Bruijn, C.W.J. Sorber, E.S. Gelsema, A.L.D. Beckers, M.I. Cleton-Soeteman, The use of optical attenuation filters for the acquisition of concentration distribution images by energy-filtered transmission electron microscopy, 4th European workshop on electron spectroscopic imaging, diffraction and analysis techniques, Münster, Germany, June 3-4, 1993.

M.I. Cleton, A.L.D. Beckers, W.C. de Bruijn, E.S. Gelsema, H.G. van Eijk, Determination of hepatic iron concentrations in situ by EFTEM with the use of a biostandard in a patient with idiopathic haemochromatosis and porphyria cutanea tarda, European Iron Club, King's College, London, United Kingdom, September 16-18, 1993.

A.L.D. Beckers, E.S. Gelsema, W.C. de Bruijn, M.I. Cleton-Soeteman, H.G. van Eijk, Electron energy-loss spectroscopic imaging for the quantitative analysis of chemical elements in cells, European Iron Club, King's College, London, United Kingdom, September 16-18, 1993.

Gelsema, E.S., Beckers A.L.D. (1992) An application of correspondence analysis for the processing of image sequences, ICPR 1992 Den Haag, 356-359.

Sorber, Lianne, Bonnet, Noel, Gelsema, Edzard, Jongkind, Hans, Beckers, Guus, de Bruijn, Wim (1992) Multivariate statistical analysis as a tool for the analysis of EELS-images, Beitr. Elektronenmikroskop. Direktabb. Oberfl. **25**, 393-398.

Other scientific publications:

Beckers, A.L.D., Dorst, L., Young, I.T. (1985) The Choice of Filter Parameters for Non-Linear Grey-Value Image Processing. In: Architectures and Algorithms for Digital Image Processing, SPIE Vol. 596, ed. Duff, M., Cannes, France, pp. 120-128.

Young, Ian T., Beckers, Guus L., Dorst, Leo, Boerman, Annelies, (1986) Choosing Filter Parameters for Non-Linear Image Filtering. In: Pattern Recognition in Practice II, eds., Gelsema, E.S., Kanal, L.N., Elseviers Science Publishers, pp. 5-15.

Van Vliet, L.J., Young, I.T., Beckers, A.L.D. (1988) An edge detection model based on non-linear laplace filtering. In: Pattern Recognition and Artificial Intelligence, eds. Gelsema, E.S., Kanal, L.N., Elseviers Science Publishers, pp. 63-73.

Van Vliet, Lucas J., Young, Ian T., Beckers, Guus L. (1989) A Nonlinear Laplace Operator as Edge Detector in Noisy Images, Comput. Vision, Graphics, Image Process. **45**, 167-195.

Beckers, A.L.D., Smeulders, A.W.M. (1989) A Comment on "A Note on 'Distance Transformations in Digital Images'", Comput. Vision, Graphics, Image Process. **47**, 89-91.

Beckers, A.L.D., Smeulders, A.W.M. (1990) The probability of a random straight line in two and three dimensions, Pattern Recognition Lett. **11**, 233-240.

Beckers, A.L.D., Smeulders, A.W.M. (1992) Optimization of Length Measurement and Pseudo-Euclidean Distance Transformations in Three Dimensions, Comput. Vision, Graphics, Image Process.: Image Understanding **55**, 296-306.

Abstracts

A.W.M. Smeulders and A.L.D. Beckers, Accurate image measurement methods (applied to 3D length and distance measurements), 1st International Conference on Confocal Microscopy and 2nd International Conference on 3-D Image Processing in Microscopy, March 15-17, 1989.

A.L.D. Beckers and A.W.M. Smeulders, 3D Length Measurements and Topographical Consequences. Symposium on 3D Image Processing and Visualisation, Utrecht, The Netherlands, April 18-19, 1990, Foundation for Computer Vision Research Utrecht, The Netherlands.

C.W.J. Sorber, G.A.M. Ketelaars, A.L.D. Beckers, W.C. de Bruijn, Quantitative EELS analysis of images of biological materials, EMAS '91 2nd European Workshop on modern developments and applications in microbeam analysis, Dubrovnic, Yugoslavia, May 13-17, 1991.

Concentration measurements in EELS images of biological materials.

I. Prerequisites for the images and spectra, C.W.J. Sorber, G.A.M. Ketelaars, A.L.D. Beckers, L.C.J. Timmermans, W.C. De Bruijn and E.S. Gelsema

II. Experiments towards the image acquisition procedure, L.C.J. Timmermans, C.W.J. Sorber, G.A.M. Ketelaars, A.L.D. Beckers, W.C. De Bruijn and E.S. Gelsema

III. Optimization of analytical procedures, A.L.D. Beckers, C.W.J. Sorber, G.A.M. Ketelaars, L.C.J. Timmermans, W.C. De Bruijn and E.S. Gelsema, Third European Workshop on Electron Spectroscopic Imaging and Analysis Techniques, Martinsried, Germany, June 27-28, 1991.

A.L.D. Beckers, W.C. de Bruijn, E.S. Gelsema, The acquisition and processing of electron spectroscopic images, Fourth European Workshop on Electron Spectroscopic Imaging, Diffraction and Analysis Techniques, Münster, Germany, June 3-4, 1993.

E.S. Gelsema, A.L.D. Beckers, C.W.J. Sorber, W.C. de Bruijn, Further investigation of the formalism of correspondence analysis as a method for the quantitative analysis of energy filtered image sequences, 4th European workshop on electron spectroscopic imaging, diffraction and analysis techniques, Münster, Germany, June 3-4, 1993.

W.C. de Bruijn, C.W.J. Sorber, E.S. Gelsema, A.L.D. Beckers, M.I. Cleton-Soeteman, The use of optical attenuation filters for the acquisition of concentration distribution images by energy-filtered transmission electron microscopy, 4th European workshop on electron spectroscopic imaging, diffraction and analysis techniques, Münster, Germany, June 3-4, 1993.

M.I. Cleton, A.L.D. Beckers, W.C. de Bruijn, E.S. Gelsema, H.G. van Eijk, Determination of hepatic iron concentrations in situ by EFTEM with the use of a biostandard in a patient with idiopathic haemochromatosis and porphyria cutanea tarda, European Iron Club, King's College, London, United Kingdom, September 16-18, 1993.

A.L.D. Beckers, E.S. Gelsema, W.C. de Bruijn, M.I. Cleton-Soeteman, H.G. van Eijk, Electron energy-loss spectroscopic imaging for the quantitative analysis of chemical elements in cells, European Iron Club, King's College, London, United Kingdom, September 16-18, 1993.

Publications

A.L.D. Beckers, Quantitative analysis of chemical elements in electron energy-loss spectroscopic image series, Nederlandse Vereniging voor Patroonherkenning en Beeldverwerking, Amsterdam, The Netherlands, April 18, 1995.

A.L.D. Beckers, W.C. de Bruijn, E.S. Gelsema, M.I. Cleton-Soeteman, H.G. van Eijk, Quantitative electron spectroscopic imaging in bio-medical research, Scanning Microscopy 1995, Houston, USA, May 6-11, 1995.

A.L.D. Beckers, W.C. de Bruijn, E.S. Gelsema, M.I. Cleton-Soeteman, H.G. van Eijk, Quantitative electron spectroscopic image analysis, 5th European workshop on electron spectroscopic imaging, diffraction and analysis techniques, Freiburg, Germany, June 8-9, 1995.

Algemene conclusies en samenvatting

De mogelijkheid om met een energie-filterende transmissie elektronenmicroscopie elektron spectroscopische beeldsequenties op te nemen is gebruikt voor het berekenen van kwantitatieve elementverdelingsbeelden in ultradun gesneden preparaten. Deel I van dit proefschrift beschrijft het onderzoek naar methodologische aspecten en de ontwikkeling van procedures voor het bepalen van concentratieverdelingen van chemische elementen. Een protocol dat de verschillende procedures integreert is ontwikkeld. Deel II behandelt de toepassing van deze procedures voor het meten van de ijzerconcentratie onder biologische omstandigheden en het afbeelden van koolstof in een modelmatig gecreëerde situatie. De belangrijkste conclusies van dit proefschrift zijn de volgende.

- Kwantitatieve chemische elementverdelingen van ultradunne coupes van biologisch materiaal kunnen worden verkregen door gebruik te maken van een commercieel verkrijgbare energie-filterende elektronenmicroscopie (Zeiss EM 902). De enige aanpassing die hiervoor nodig is, is de montage van een filterhouder vóór de TV-camera. De resolutie van de verkregen ijzerverdelingsbeelden ligt dicht bij die van conventionele EM-foto's en in dit opzicht komt het resultaat van de gevolgde procedures dan ook tegemoet aan de verwachtingen van een elektronenmicroscopist. De ondergrens van de concentratie van ijzerhoeveelheden die nog kunnen worden gekwantificeerd ligt momenteel rond de 0.5 atomen/nm³ (afhankelijk van vele factoren). Deze eigenschappen maken de meetopstelling geschikt voor het gebruik ervan ten behoeve van onderzoek naar ijzerstapelingscondities binnen de pathologie.
- Voor de visuele interpretatie van elementverdelingen is aangetoond dat deling van de netto-intensiteit door de geïntegreerde zero- en low-loss bijdragen eveneens van belang is, wanneer ook maar iets meer over deze verdelingen geconcludeerd zou moeten worden dan alleen de binaire uitspraak betreffende aan- of afwezigheid van elementen.
- In levercoupes van een idiopatische hemochromatose patiënt, verkregen voor en na flebotomie, kon geen verschil worden aangetoond tussen de gemiddelde ijzerconcentraties binnen organellen voor en na deze behandeling. Dus het ijzer is verdwenen uit andere compartimenten dan die geanalyseerd na flebotomie, hetgeen een indicatie is voor het organel-specifieke karakter van het ijzermobilisatieproces.
- Voor het onderzoek van stukjes weefsel van mens en dier in een toestand van ijzeroverlading kan een (in situ) chemische karakterisering van ijzerhoudende celonderdelen worden bewerkstelligd door middel van ijzerconcentratiebepaling. Zo konden gebieden in de cel die ferritine bevatten worden onderscheiden van gebieden die bestaan uit degradatieproducten van dit molecuul.
- Het afbeelden van macromoleculaire structuren, opgenomen in een extreem dunne film (van b.v. 2 nm chrom), op basis van de aanwezige de koolstof in die structuren lijkt haalbaar. De instrumentele condities alsmede de preparatietechnieken zijn voor verbetering vatbaar en het is dus voorbarig nu reeds een oordeel te vellen over haalbare resoluties.

In het eerste deel dit proefschrift stond de uitdrukking van Egerton, vgl. (3.2), om de elementconcentratie kwantitatief te bepalen centraal. Deze expressie geeft een aantal grootheden aan die afgeleid dienen te worden uit een spectroscopische beeldreeks: het netto-intensiteitsbeeld I_k en de geïntegreerde zero- and low-loss bijdrage I_T . Dit betekent dat de microscoop, in plaats van een hulpmiddel voor visualisatie dient te worden geconverteerd in een meetinstrument. Een van de hoofdeisen om een apparaat als meetinstrument te kunnen gebruiken is dat de geleverde meetwaarden een getrouwe representatie zijn van meetgrootheid. Het apparaat dat in dit proefschrift wordt beschouwd is een energie-filterende elektronenmicroscoop die beelden op een scintillatiescherm projecteert die vervolgens door een TV-camera worden waargenomen. Deze camera is verbonden met een beeldverwerkingssysteem.

Aan de TV-camera wordt de eis gesteld dat intensiteitsverdelingen van energie-gefilterde elektronen die door het spleet-apertuur worden doorgelaten kunnen worden afgebeeld. In principe is dit mogelijk, echter de TV-camera verstoort ook de beelden en kan daarnaast niet het grote dynamisch intensiteitsbereik, zoals we dit tegenkomen in het spectrum, overbruggen. Dit heeft geresulteerd in het toevoegen van optische verzwakkingsfilters voor twee doeleinden: het overbruggen van het grote dynamisch bereik en het meten van de camera distorsies. Verder zijn correctieprocedures geïmplementeerd voor de compensatie van shading en de niet-lineaire fotometrische respons van de camera. Om elementverdelingsbeelden te berekenen zijn beeldreeksen nodig. Laterale drift die regelmatig optreedt bij de opname van dergelijke reeksen behoeft eveneens correctie. Alle correctiestappen, voor shading, niet-lineariteit alsmede drift, zijn getest en worden als essentieel beschouwd in het proces van kwantificeren. De optische filters zijn een effectief middel voor lichtverzwakking. Er is echter enige onzekerheid over het gedrag van het scintillatiescherm als gevolg van de grote elektron intensiteitsverschillen.

Energie-gefilterd afbeelden in de elektronenmicroscoop is een vorm van elektron gelimiteerde beeldvorming, hetgeen betekent dat het aantal elektronen dat deelneemt aan de beeldvorming dusdanig klein is dat de beelden inherent veel ruis bevatten. Voor de statistische karakterisatie van de beelden is de detectieketen onderzocht. Door de aanname van een eenvoudig model voor de interactie van elektronen met het scintillatiescherm en voor de detectie van fotonen door de camera kon een lineaire relatie tussen gemiddelde intensiteit μ en variantie σ^2 worden afgeleid. Deze relatie is experimenteel bevestigd. Een normale verdeling $N(\mu, \sigma^2)$ werd vervolgens aangenomen om de statistiek van de opgenomen beelden te beschrijven, waarbij μ en σ^2 in ieder pixel verschillend kunnen zijn. Voor de spectrale karakterisering van de beeldreeksen hebben we ons beperkt tot die gebieden waar de zgn. power-law (vgl. 5.1) geldig is. De combinatie van de power-law met de statistisch beschrijving leverde een statistisch model voor de spectrale achtergrond, waarmee de basis werd gelegd om het achtergrondsubstractieprobleem op te kunnen lossen.

Met behulp van het beschreven model leidt de theorie van statistisch parameterschatten

tot de formulering van de schatting van de achtergrondparameters in termen van een niet-lineair gewogen kleinste-kwadratenprobleem. Dit probleem werd opgelost door het ontwerp van een zeer efficiënt iteratief algoritme. Toepassing van dit algoritme op de pre-edge subset van een spectroscopische beeldreeks levert de gewenste parameterwaarden. Deze waarden worden vervolgens gebruikt voor extrapolatie van het model naar de edge-regio, waardoor een schatting van de achtergrond wordt verkregen. Deze achtergrond wordt afgetrokken van de totale edge-intensiteit en resulteert in het netto-intensiteitsbeeld. Toepassing van de theorie van statistisch parameterschatten maakte het tevens mogelijk een indicatie van de precisie van de achtergrondschatting te verkrijgen. Deze eigenschap werd gebruikt om significante element bijdragen in het netto-intensiteitsbeeld te detecteren door drempeling van het corresponderende SNR-beeld (signaal-ruis-verhoudingsbeeld).

De berekening van het netto-intensiteitsbeeld is slechts één enkele stap in het hele proces van kwantitatieve analyse. Deling door de geïntegreerde zero- en low-loss spectrale beeldbijdragen, gevolgd door calibratie met behulp van een Bio-standaard resulteert in kwantitatieve elementverdelingsbeelden. De Bio-standaard, die in de zelfde coupe aanwezig is en een bekende (met neutronenaktivatie verkregen) concentratie referentiewaarde heeft, wordt gemeten met dezelfde microscoop, onder vergelijkbare condities als waarmee de onbekende wordt gemeten. De resulterende beelden worden verwerkt met dezelfde procedures. Twee belangrijke voordelen met betrekking tot de robuustheid van deze aanpak zijn genoemd: het effect van massaverlies door stralingsschade wordt gereduceerd en eventuele niet-lineariteiten in de detectieketen worden onderdrukt. Een nog niet opgelost probleem is de variabiliteit in de belading van de Bio-standaard met een element. Een alternatief om de betrouwbaarheid en flexibiliteit van het werken met de standaarden te vergroten wordt genoemd in hoofdstuk 9.

Het functioneel bereik van de meetschaal is onderzocht in hoofdstuk 7 met een aantal experimenten. Aan de bovenkant van de meetschaal wordt een afwijking waargenomen van de verwachte lineaire relatie tussen een gegeven elementhoeveelheid en de gemeten waarde. Deze afwijking neemt toe met toenemende relatieve coupedikte. De onderkant van de meetschaal wordt begrensd door de aanwezige ruis. Suggesties werden gegeven om het functionele bereik van de schaal te vergroten door correctie voor meervoudige verstrooiing (verbetering van de lineariteit) en het gebruik van spatiële middelingstechnieken om de signaal-ruis verhouding van de beelden te verbeteren of door alternatieve methoden voor achtergrondcorrectie (correspondentieanalyse of MLS-fitting) te gebruiken. Aangegeven werd het belang van de meting van de relatieve coupedikte voor het kwantificeren. Deze registratie is momenteel een vast onderdeel van de validatieprocedure van het meetproces. Daarnaast bestaan er checks voor stralingsschade en coupedrift alsmede een meer algemene controle voor de consistentie van de data door zogenaamde ghost-beelden te berekenen. Dergelijke validatiestappen worden beschouwd als essentiële onderdelen in het hele proces van kwantificeren. De additionele data-acquisitie inspanning om deze te kunnen uitvoeren is klein.

De analyse van dubbele coupes van in epon ingebedde Fe-Chelex, die tevens enige

Algemene conclusies en samenvatting

snijartefacten bevatten, gaven duidelijk aan dat visuele interpretatie van netto-intensiteitsbeelden vrijwel onmogelijk is als ook maar iets meer over deze beelden gezegd zou moeten worden dan de aan- of afwezigheid van het element. De effectiviteit van de correctie voor massa-dikte door middel van deling door zero en low-loss beelden werd geïllustreerd. De conclusie is dat ook ten behoeve van visuele interpretatie massacorrectie noodzakelijk is.

De ontwikkelde meetprocedures zijn toegepast in een onderzoek naar de opslag van ijzer in structuren binnen leverparenchymcellen van een idiopatische hemochromatose patiënt. In het bijzonder is het effect van flebotomie op de ijzeropslagstructuren bestudeerd. De vergelijking van de resultaten van ijzerconcentratiemetingen, uitgevoerd in 32 organellen vóór en in 22 organellen na flebotomie leverde geen significant verschil op. De conclusie was dat flebotomie niet heeft geresulteerd in de verwijdering van ijzer uit de nog resterende ijzer bevattende organellen. Dit resultaat ondersteunt dan ook de hypothese dat de geïnduceerde vraag naar ijzer resulteert in een organel-specifieke mobilisatie van het ijzer. Gesuggereerd werd dat door bijvoorbeeld een betere lokalisatie van de analysegebieden de genoemde hypothese verder ondersteund zou kunnen worden. Een poging om de ijzerhoudende structuren chemisch verder te karakteriseren op basis van de lokale ijzerconcentratie was succesvol. Echter, door de mogelijk aanwezige volume effecten zijn de ijzerconcentratiehistogrammen complex, hetgeen een eenvoudige classificatie van de corresponderende structuren verhindert. Een mogelijke relatie tussen gemiddelde organel ijzerbelading en object parameters gerelateerd aan de morfologie (oppervlak en contour ratio) kon niet worden aangetoond.

In een tweede toepassing werd de mogelijkheid om ESI hoofdzakelijk als beeldvormende modaliteit te gebruiken onderzocht. Geïsoleerde ferritinemoleculen, geprepareerd op een 2 nm dikke chroomfilm, zijn gebruikt als testobjecten om koolstofverdelingsbeelden te verkrijgen. De resultaten van dit experiment zijn veelbelovend. Desalniettemin zijn de samenstelling van de preparaten en condities voor beeldvorming voor verbetering vatbaar. Meer experimenten lijken nodig alvorens een definitief oordeel over deze techniek kan worden gegeven.

Dankwoord

Een proefschrift komt zelden tot stand door alleen de inspanning van de promovendus. Een woord van dank aan hen die aan dit proefschrift hebben bijgedragen is dan ook op zijn plaats. Edzard Gelsema, zonder jou als promotor was het vast niet gelukt. Vrijheid van onderzoek is bij jou een begrip. Wim de Bruijn, in de samenwerking tussen Medische Informatica en Pathologie was jij de katalysator. Ik heb veel van je gekregen: kennis, eigenwaarde, moed, etc. Respect krijg je van mij. Henk van Eijk en Maud Cleton-Soeteman, jullie belangstelling en inbreng waren voor mij zeer waardevol en maakte de samenwerking ijzersterk en vooral heel gezellig. Lianne, Ton en Peter van de afdeling Pathologie, jullie hebben mijn leven in de buurt van de elektronenmicroscop een stuk makkelijker gemaakt. Prof. Dr. Georg Gosztanyi en Timucin Türker van de Freie Universität Berlin ben ik zeer veel dank verschuldigd voor het gastvrije verblijf in Berlijn en het uitlenen van de SIT camera. Verder bedank ik iedereen in mijn omgeving die mijn werkplezier heeft vergroot en zodoende in positieve zin heeft bijgedragen. Last but not least is daar Marjolein, mijn vrouw die alle ongenoemens en tegenslagen als een berg voor haar fiets kreeg. Door jouw sterke benen kwam ik er steeds weer bovenop. In mijn wiel is altijd plaats voor jou.

Curriculum Vitae

De auteur van dit proefschrift werd op 29 november 1958 geboren te 's-Gravenhage. In 1978 werd met het eindexamen de middelbare school periode (VWO-B) op het St-Maartenscollege te Voorburg afgesloten. In aansluiting daarop werd de studie technische natuurkunde aan de Technische Universiteit te Delft gevolgd. Deze studie werd binnen de sectie Patroonherkennen, als onderdeel van de vakgroep Systemen en Signalen, in 1986 afgerond. Tijdens de studie werd gedurende een periode in 1985 en 1986 als student assistent in de vakgroep gewerkt. Vervolgens werd in 1986 en 1987 bij het Nationaal Lucht- en Ruimtevaartlaboratorium NLR gewerkt in de Remote Sensing afdeling van de hoofdafdeling Ruimtevaart. In 1987 is de auteur begonnen als medewerker in de beeldverwerkingssectie van de vakgroep Medische Informatica van de Erasmus Universiteit Rotterdam. Na enig wetenschappelijk werk op ander terrein werd het onderzoek aangevangen waarvan een beschrijving in dit proefschrift is te vinden.

